Detection and tuning of non-local conductance in a nanowire Cooper pair splitter

by

Thomas Antonio Marangoni

Supervised by Jesper Nygård and Kasper Grove-Rasmussen

A thesis presented for the degree of
Master of Science

UNIVERSITY OF
COPENHAGEN

Center for
Quantum
Devices

Department of Nanoscience
Faculty of Science
University of Copenhagen
Denmark
31-08-2016

Abstract

This thesis presents non-local conductance measurements on a total of 16 resonance crossings in a nanowire Cooper pair splitter. The Cooper pair splitter has two gold electrodes acting as the normal contacts and an aluminium electrode acting as the superconducting contact, connected by an InAs nanowire. The majority of the non-local signals consisted of a positive and a negative peak, attributed to the transition of the ground state in the superconductor from a singlet to a doublet state and vice-versa. Afterwards, the bottom gates on the device were used to tune the Cooper pair splitter to several configurations, attempting to find the regime with the highest non-local efficiency. The splitter was successfully manipulated, detecting an increase in efficiency after several configurations. This thesis has successfully demonstrated the possibility of configuring a Cooper pair splitter device to a more optimal regime, a step towards creating a reproducible and highly efficient source of entangled electrons.

Contents

1 Introduction **1**
- 1.1 Thesis outline . . . 1
- 1.2 Acknowledgements . . . 2

2 Background **3**
- 2.1 Quantum computers . . . 3
- 2.2 Cooper pair splitters . . . 4

3 Theory **7**
- 3.1 Superconductivity . . . 7
- 3.2 Semiconductor nanowires . . . 8
- 3.3 Quantum dots . . . 8
- 3.4 Alternative transport through a quantum dot . . . 11
- 3.5 A quantum dot coupled to a superconductor . . . 11
- 3.6 Cooper pair splitters . . . 14
- 3.7 Current through a Cooper pair splitter . . . 16

4 Fabrication **19**
- 4.1 The silicon wafer . . . 19
- 4.2 Imprinting the design . . . 19
- 4.3 Metal deposition . . . 21
- 4.4 Nanowire deposition and contact . . . 22
- 4.5 The device used in this thesis . . . 23

5 Method **25**
- 5.1 Instrument setup . . . 25

6 Results and Discussion **31**
- 6.1 Detection of the non-local signal . . . 31
- 6.2 Tuning of the non-local signal . . . 46

7 Conclusion **61**

8 Appendix **63**

Bibliography **76**

Chapter 1

Introduction

The quantum world has fascinated me since learning about the many bizarre phenomenon in the field such as wave-particle duality, the Heisenberg uncertainty principle and the famous Schrödinger's cat to name a few. The fact that we still do not fully understand many aspects of quantum mechanics showed me that there was still so much to learn in this area of physics and it's one of the reasons why I decided to study nanotechnology. Nanotechnology is a perfect mix of applying the quantum world to real life problems and will be one of the fundamental pillars of future life, with tons of potential in physics, biology and chemistry. A promising area is quantum computing which, when realised, will revolutionise many aspects of life. I am extremely grateful to have been given the opportunity to contribute to its creation.

This thesis focusses on a nanoscale device called a Cooper pair splitter, a piece of equipment helpful in the creation of qubits, an essential component of future quantum computers. Cooper pair splitters aim to take apart the bound electron pairs occurring in the ground state of superconductors to create spatially separated, entangled electrons. The aim of this thesis is to build upon existing research in Cooper pair splitters, using the knowledge and techniques learned to attempt to tune the device to high efficiency configurations, working towards a reliable and reproducible entangled electron source. This thesis presents detection of non-local conductance on an InAs nanowire based Cooper pair splitter and subsequent successful tuning of the device's configurations to more efficient splitting regimes.

1.1 Thesis outline

This thesis will start by providing a short background of Cooper pair splitters. Here the importance of the device will be outlined along with some influential experiments in the field. Next, in chapter 3, the theory behind Cooper pair splitters is detailed. Each component of a splitter will be addressed and explained in the context of this thesis. Chapter 4 contains a summary of the fabrication techniques used to build Cooper pair splitter devices. At the end of the chapter the device used in this thesis is presented. In chapter 5 the experimental setup is shown. Chapter 6 showcases all the data collected and includes the discussion of the data. Finally, chapter 7 will shortly summarise the thesis and provide any concluding thoughts.

1.2 Acknowledgements

I would firstly like to thank my lead supervisor Jesper Nygård for giving me the opportunity to do my master thesis at QDev. Being one of the leading centres in the field, the large number of resources and knowledgeable people in the laboratory greatly improved my learning experience. Furthermore, by being a calm and level-headed supervisor and allowing me to have control in the project and writing has taught me more than just the contents of the thesis. I'd like to thank my co-supervisor Kasper Grove-Rasmussen for helping with running the measurements and for being an immense source of theoretical and experimental knowledge on the subject. And most importantly for always being willing and patient enough to answer my numerous questions. I would like to thank Anders Jellinggaard for building the device used in this thesis and Morten Hels for providing help and information in the early stages of the experiment along with giving me helpful tips on how to use the analysis programs and IT-systems. I would also like to thank my fellow master student Kasper Laursen for taking time out of his schedule to teach me how to operate various instruments involved in the fabrication. I would of course like to thank my family who, with their support and encouragement, have enabled me to study and live in Copenhagen. And lastly I would like to thank all my friends here who have made my stay in Denmark not just an educational one, but also a very enjoyable one.

Chapter 2

Background

This chapter will provide a short background to Cooper pair splitters. First a brief explanation of the quantum mechanical processes essential to the operation of Cooper pair splitters is explained along with a short description of their use in quantum computers. Next the geometry of the device is briefly introduced along with several influential research papers on the subject.

2.1 Quantum computers

Quantum entanglement is a quantum mechanical phenomenon where two or more particles are described by a quantum state. As such, a property like momentum or spin cannot be attributed to a single particle. Instead, the quantum state carries the property. As a result, measuring one particle in a two particle entangled state will instantly give information about the second particle, even when they are spatially separated. These phenomenons were described in the famous paper by Einstein, Podolsky and Rosen in 1935. [1]

One of the areas in which quantum entanglement can potentially be useful, and the area this thesis concerns itself with, is quantum information. Entangled particles are essential for the realisation of the quantum bit, the building block of the quantum computer. Quantum bits, called qubits, consist of ideally two entangled particles in a superposition, which result in the qubit being able to hold both a value of 0 and 1 simultaneously. [2] This is in contrast to the classical bit which is either 0 or 1. The quantum state of the qubit is generally represented in the Dirac notation as:

$$|y\rangle = |0\rangle + |1\rangle$$

Another way to visualise the superposition of the qubit is through the use of a Bloch sphere. A classical bit, which can be either 0 or 1, points to the north ($|0\rangle$) or south pole ($|1\rangle$). In a quantum bit the state can point to any part of the sphere's surface, reflecting the superposition being able to take on any combination of 0 and 1.

The power of the qubit can be seen when considering a 2 bit registry. A computer using classical bits is able to only store one of the four possible numbers $(00, 01, 10, 11)$. Qubits are able to store all four numbers at the same time. This increases exponentially when more qubits are added. A computer using qubits is able to make 2^n parallel calculations where n is the number of qubits. [3] A quantum computer therefore has the capability to process complex calculations potentially a million times faster than a classical computer. A working quantum computer will

revolutionise many computational tasks such as encryption, database searching and complex simulations. [4] [2] A quantum computer is able to decode the conventional encryption methods in instants, will find a request in a database in the square root of the time it takes now and will be capable of much more elaborate calculations and simulations than is possible today.

Realising a quantum computer is very difficult however. One of the hard parts is creating stable, spatially separated, entangled pairs for the qubits. Currently a stable qubit can be held for several hours at cryogenic temperatures. [5] The entangled pairs used today are mostly photons or electrons. Entangled photons can be generated by parametric down conversion. [6] [7] In parametric down conversion a laser beam is split by a non linear crystal, where a single photon can be converted to two photons. This pair of photons has the same energy and momentum as the original photon along with correlated polarisations. The correlated polarisations enable the photons to be used as an entangled pair in quantum computing.

2.2 Cooper pair splitters

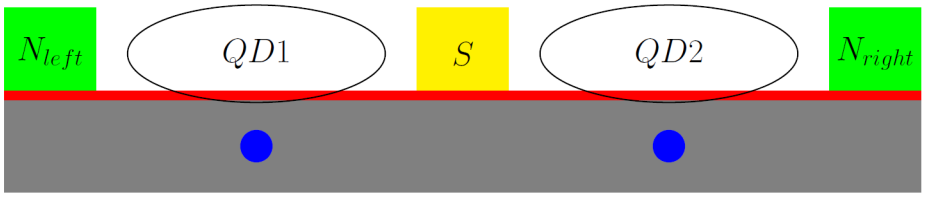

Figure 2.1: *A simplified schematic of the geometry of a Cooper pair splitter. This is not to scale. The nanowire or nanotube indicated by the red line is connected to two metal electrodes, the green rectangles denoted by N, at each end and a superconducting electrode, the yellow rectangle denoted by S, in the centre. The quantum dots that form are represented by the black ellipses and are named QD1 and QD2. The small blue circles underneath the wire are the gates which are used to manipulate the energy levels in the dots. There are only two shown in this figure but more can be added to increase the precision of tuning or manipulate the way the dot is coupled to the electrodes. A Cooper pair splitter is generally built on a silicon wafer, shown here as the grey base.*

Another way of generating spatially separated entangled pairs is the Cooper pair splitter (CPS). Cooper pairs are the charge carriers in superconductors and are made up of two spin-entangled electrons. [8] The CPS is a fabricated device which aims to split these Cooper pairs, leaving a spatially separated, entangled electron pair. A simplified schematic showing all the necessary components is shown in Fig. 2.1. A nano electronics device is generally built on top of a silicon wafer, depicted here as the large grey rectangle. A CPS consists of a nanowire or nanotube, shown in Fig. 2.1 as the red line, connected on each end by a metal contact, indicated by the green rectangles named N in Fig. 2.1. In the centre a superconductor, commonly denoted by S, connects to the wire. At low temperatures two quantum dots (QD1 and QD2) form between the superconducting and metal contacts. With side or bottom gates the energy levels in these dots can be manipulated. These are represented by the small blue circles in the figure. In reality these are thin leads that run below or next to the nanowire or nanotube. A voltage on the gate will affect the electrostatic environment around it. Another option, if there are no side or bottom

gates is to use the wafer as a device-wide back gate to control the electrostatic environment. When the Cooper pair splitter is in the right configuration these quantum dots can only hold one electron at one time, forcing the electrons of the Cooper pairs to travel separately into the two dots or consecutively though a single dot. By suppressing the latter, the Cooper pairs can be confidently split into a spin-entangled, spatially separated electron pair in the metal contacts.

The first tunable Cooper pair splitter was realised in 2009 by Hofstetter et al. [9]. Simultaneously, Hermann et al. developed a Cooper pair splitting device as well, whose paper was published a few months later. [10] Hofstetter et al. had built two Cooper pair splitting devices. Side gates were added near the two quantum dots to tune their energy levels. One of the devices had dots strongly coupled to the metal contacts, while the in the other they were weakly coupled. In order to detect Cooper pair current, the conductance through a quantum dot (QD1) was measured while the energy levels in the other quantum dot (QD2) were moved around via the side gate. Moving the levels in QD2 affected the transport through QD1. This is known as the non-local conductance, as the signal through QD1 depends on the situation in QD2.

In order to detect the non-local signal due to Cooper pair splitting, The group measured the conductance through QD1 and subtracted the mean value, which gives a non local signal through QD1 defined as:

$$\Delta G_1 = G_1 - \langle G_1 \rangle$$

where G_1 is the conductance through QD1 and $\langle G_1 \rangle$ is the mean value. The group measured ΔG_1 at different positions of the energy levels in QD1 while sweeping the levels in QD2. ΔG_1 was found to be heavily dependent on the level position in QD1. At the edge of the energy level a strong positive non-local signal was observed. Moving closer towards the centre of the level peak the signal decreases to eventually change sign and become maximally negative at the peak centre. This result was observed in both samples and different charge states. Additionally the non-local signal was found to disappear with increasing temperature, completely vanishing at around 200 mK reinforcing the fact that Cooper pair splitting is responsible for the non-local conductance. The maximum splitting efficiency of 2% was observed at the lowest temperature of 20 mK. This may seem low, however it is much higher than had previously been accomplished with photons in parametric down conversion. Hofstetter et al. does give room for improvement as it states that not all requirements for an efficient Cooper pair splitter were fulfilled.

In 2012 Schindele at al. [11] reported a Cooper pair splitter with a splitting efficiency of 90%. The device was similar as the one fabricated in Hofstetter et al., with a carbon nanotube connected to two palladium contacts at each end with a superconducting palladium/aluminium contact in the centre. Two side gates are able to tune the two quantum dots. The group tuned the levels in one dot (QD1) while measuring the conductance G_2 in the second dot (QD2). They observed a sharp peak (ΔG_2) in the conductance of QD2 when the levels of QD1 were aligned with the chemical potentials of the electrodes. This peak quickly disappeared when the levels in QD1 moved away from this resonance condition, confirming the peak was due to non-local processes. The group defined the splitting efficiency in one dot as $\frac{\Delta G}{G}$. By assuming that $\Delta G_1 = \Delta G_2$, the splitting efficiency of the entire device becomes:

$$s = \frac{2G_{CPS}}{G_1 + G_2}$$

where $2G_{CPS} = 2\Delta G_2$. Using this definition Schindele et al. obtained efficiencies of up to 90%.

Fülöp et al. [12] fabricated a device with a total of 10 bottom gates, making it possible to finely tune not only the levels in the dots, but also the coupling between the dots and the electrodes which has a large effect on the current flowing through the dots. The device consisted of an InAs nanowire connected to two Ti/Au electrodes at each end and a Nb superconducting electrode in the centre. The group measured the non-local conductance in a similar fashion as Schindele et al. and Hofstetter et al. However fülöp et al. then used the side gates to vary the coupling strengths enabling them to investigate its effect on the non-local signal. They found the non-local Cooper pair conductance to be strongly dependent on the contact barriers of the local gates. Tuning the coupling of the dots with the normal electrodes they observed a change of an order of magnitude in the total conductance. The tuning of the coupling with the superconducting electrode had less of an impact, although they did not investigate it as thoroughly. The group sees definite possibilities in using gates to tune a Cooper pair spitter to the most favourable configuration.

This thesis will move forward on the statement made by Fülöp et al. attempting to configure the device to maximise the splitting efficiency. Measurements of non-local signals were done on an InAs nanowire based Cooper pair splitter device. The device is unique in the fact that it has 15 gates available to configure the device.

Chapter 3

Theory

The Cooper pair splitter is a fairly new and complicated device. It has many components that are not fully understood, such as superconductivity or the junction of a quantum dot with normal and superconducting metals. A full and complete theory on the Cooper pair splitter therefore does not exist yet. Many papers develop their own descriptions and definitions of the current moving through a CPS device and the efficiency of splitting. This thesis does not aim to reinvent CPS theory, but is instead concerned with detecting Cooper pair current and the tunable nature of this current. The goal of this chapter is to introduce the core ideas on which the Cooper pair splitter is built, which includes superconductivity, nano wires and quantum dots, and explain the physics that drives it.

3.1 Superconductivity

Superconductivity is a phenomenon that occurs in certain metals. The electrical resistance in the metal vanishes when the temperature falls below a certain critical temperature, T_c. [13] Below this temperature, a current can ideally run forever. Another feature of superconductivity is the expulsion of an external magnetic field from the metal. [13] As a result, there also exists a critical magnetic field, B_c, above which the magnetic field is able to break down the superconductivity due to the high energy cost to keep the field out. In a superconducting metal, electrons are attracted to each other and form pairs. The pairs can be separated by several hundred nanometres, which is useful when it is neccesary to split them. [14] Classically the pair attraction can be visualised by considering the electron moving across the metal, attracting positive ions and increasing the positive charge density around the electron which, in turn, attracts other electrons. This occurs for any net attraction, no matter how small it is. However the binding energy is of the order of 10^{-3} eV, so only at low temperatures will there be a significant number of Cooper pairs present. [15] The quantum mechanical picture is more complicated, and attributes the attraction to electron-phonon interactions. [16] The BCS theory on superconductivity describes it further, but this is beyond the scope of this thesis.
It was discovered that the electrons in a pair always have opposite momentum $k_1 = -k_2$. [8] As a result the Cooper pairs can be described by an orbital wave function. Cooper pairs are bosons and have an integer spin, thus in order to keep the symmetric total wave function, the orbital wave function has to be multiplied with a spin singlet:

$$|S\rangle = \frac{1}{\sqrt{2}} \left(|\uparrow\downarrow\rangle - |\downarrow\uparrow\rangle \right)$$

The result of this action means that the spin of the electrons are in a superposition state. Measuring the spin on one electron will determine the spin of both electrons: one pointing up, one pointing down; the individual spins of a Cooper pair are maximally entangled with the total spin being zero.

Since Cooper pairs are bosons, they collapse to the same ground state at low temperatures. When a metal is superconducting, BCS theory states that excitations from this ground state require a minimum energy of 2Δ, forming an energy gap of Δ to $-\Delta$. This is called the superconducting energy gap.

3.2 Semiconductor nanowires

Nano scale electronic devices often use nano-wires or tubes as a fundamental component. Due to their geometry they have strong quantum confinement, allowing for easily created quantum dots. Their linear nature also makes it easy for fabrication, as the wires are generally several microns long, while the resolution of nano fabrication techniques can easily achieve distances down 10 nm. [17] Nanowires are also easy to produce in great quantities using current growth techniques. [18] [19] [20]
Semiconductors are often chosen as the basis for the wires due the tunable electronic properties of such a wire. The geometry of a wire causes a quantisation of the electron energy, resulting in quanitsed energy channels that carry the current. The conductivity of a wire is the sum of these quantised energy channels and the thinner the wire, the fewer of these channels exists. [21] These channels can be easily tuned, for example by using a side or bottom gate. By adjusting the voltage on the gate, the current through a semiconductor nanowire can be controlled and ultimately pinched off. Semiconductor wires also allow for doping to alter its desired electronic properties. Another reason to choose semiconductor nanowires are the semiconductor-metal contacts which are more reliable than other options such as carbon nanotubes. In addition to that, problems related to Schottky barriers at the semiconductor-superconductor interface can be avoided by using semiconductor wires such as InAs, where the Fermi level at the surface is fixed in the conduction band.

3.3 Quantum dots

At low temperatures the thermal energy of the electrons in the nano wire is not enough to overcome the potential barriers of the contacts. Instead they need to tunnel through the barriers to enter and exit the wire. A quantum dot forms when the tunnel resistance becomes proportionate to the quantum resistance $R_t \gtrsim \frac{h}{2e^2}$. [22] The quantum dot occupies the space of the wire between the contacts. This is shown in Fig. 8.1b, where the QD, named CNT QD, sits in between the source and drain contacts of this particular carbon nano tube device. A charge carrier moving from the source to the drain therefore has to pass through the dot. A schematic of this situation is drawn in Fig. 8.1c. Here the QD is shown to be coupled capacitively to the source and drain contacts. The Γ refers to the strength of the tunnel coupling, and a higher Γ indicates better coupling and thus a higher current through the tunnel barrier. It is important to note that the coupling to the back gate (BG), which in this case is the silicon wafer the device was built on. Gates are separated from the dot by a large enough distance or a dielectric barrier so that the electrons are not able to tunnel to or from the QD. However putting a bias on the back gate (V_g) will still influence the electrostatic potential in the dot, as indicated by the capacitive

coupling of the back gate in Fig. 8.1c.
The quantum dot restricts the electron momentum in three dimensions and therefore has a discrete energy spectrum as indicated in Fig. 8.1a. The discrete energy levels restrict the electron flow to just one electron at a time. [23] The energy levels in the dot are often called ϵ or $\mu(N)$ where N refers to the number of electrons on the dot. An electron occupying a level will charge the dot, which will result in a voltage gain $U = \frac{e}{C}$, where C is the capacitance of the tunnel barrier. [24] However, for a small enough dot, the voltage gain in the dot can repel other electrons from entering the level via Coulomb interactions, and so prevent a further flow of electrons. Thus at low source-drain voltage, current flow through the device is blocked and the system is in Coulomb blockade. [24] [25]

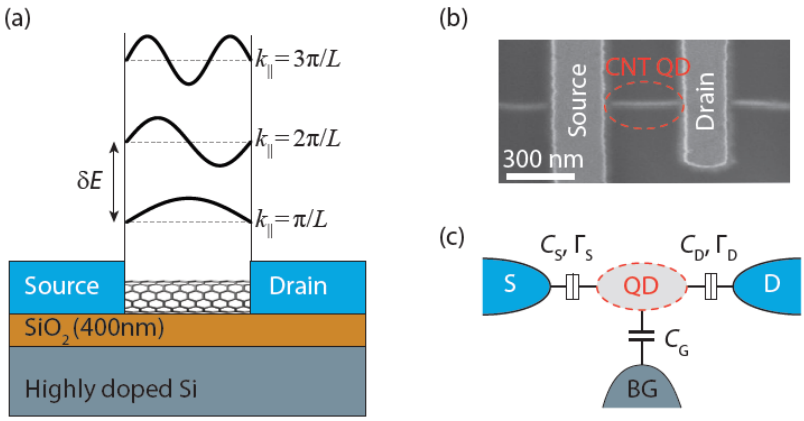

Figure 3.1: *(a) shows the quantum dot energy spectrum and location on a carbon nanotube wire. For the case of a carbon nanotube the energy levels are equally spaced. For a semiconductor wire such as InAs this is not the case. (b) shows the position of the formed quantum dot with respect to the source and drain electrodes. (c) illustrates the coupling the dot has to the source and drain contacts and any additional nearby gates. It is important to note that the back gate is only capacitively coupled and is only used to influence the states in the quantum dot and not as another drain contact. Figure adapted from [22].*

When a voltage is applied to a gate close to the qauntum dot, it will shift its energy levels linearly via the relation $\alpha\Delta V_g$. α is known as the gate factor. [26] The shift enables an electron in Coulomb blockade to exit the dot when a level in the dot is lined up with the chemical potentials of the source-drain contacts, μ_S and μ_D. This is when the quantum dot is in resonance.[25] A schematic of this procedure is shown in Fig. 8.2, where a gate voltage has shifted the $\mu(N+1)$ resonance in Fig. 8.2a down to the level of chemical potentials of the electrodes in Fig. 8.2b. When in resonance the electrons flow across the dot and will enable a current through the dot. Changing the gate voltage further until the chemical potential of the level is lower then μ_S and μ_D, will enable Coulomb blockade again. When the next level is aligned, a current is able to flow again and so on. Measuring the differential conductance, $G = \frac{\partial I}{\partial V_{SD}}$, illustrates this by showing a peak when the dot is in resonance and being zero otherwise. A $\frac{\partial I}{\partial V_{SD}}$ measurement of the device in Fig. 8.1 is pictured in Fig. 8.2c. The situation in Fig. 8.2a gives zero conductance, as the device is in Coulomb blockade, whereas Fig. 8.2b with the QD resonance level with μ_S and μ_D results

in a Coulomb peak.

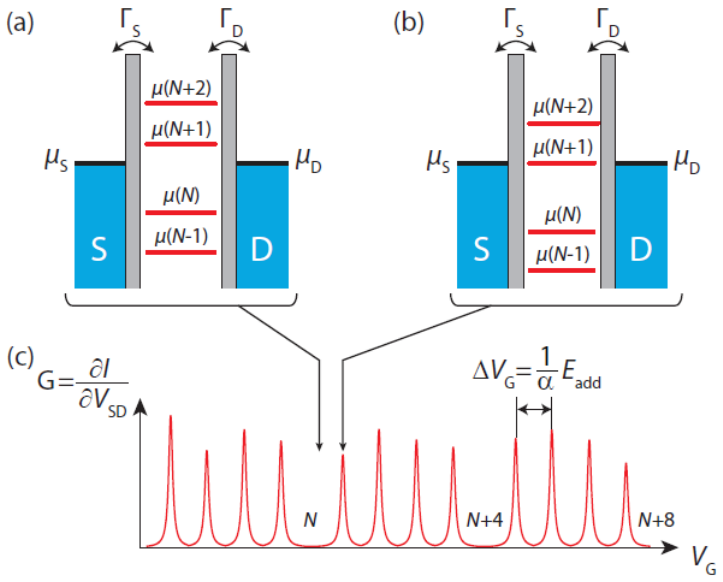

Figure 3.2: *The Coulomb peak measurement from the device in Fig. 8.1 (a) The dot is in Coulomb blockade and no current is possible through the dot. As a result the measured conductance in (c) is zero (b) The dot has been tuned with a back gate to move the energy levels in the dot to be equal to the chemical potential of the electrodes, indicated by μ_S and μ_D. Now a current is able to flow though the dot, resulting in a conductance peak in (c). (c) A $\frac{\partial I}{\partial V_{SD}}$ measurement as the the gate voltage is swept. Coulomb peaks are observed where transmission through the dot is possible. The N and N+4 refer to the carbon nanotube shells which are not relevant for this thesis but more information can be found on them in [22]. Figure adapted from [22].*

The height and width of a Coulomb peak can be used to extract the strength of the coupling Γ of the dot with the source-drain electrodes. Jørgensen et al. [27] developed an approximation of the Coulomb peak given by the Lorentzian expression:

$$G = \frac{e^2}{h}\frac{4\Gamma_L\Gamma_R}{\Gamma^2}\frac{(\frac{\tilde{\Gamma}}{2})^2}{\epsilon^2 + (\frac{\tilde{\Gamma}}{2})^2}$$

where $\tilde{\Gamma} = 1.36\Gamma$, $\Gamma = \Gamma_L + \Gamma_R$ and ϵ is the level energy (V_g). The subscripts L and R refer to the coupling to the left and right of the dot, such as the source and drain contacts.

When extracting the Γ's, this approximation is fitted against the Coulomb peak in the normal state. The fit returns a value for Γ_L and Γ_R and the total coupling strength Γ. The downside of this method is that the fit is not able to assign the value to Γ_L or Γ_R directly. This has to be done manually. This can either be done by looking for signs that the dot is coupled more strongly to one side, for example by identifying the shape of sub-gap states, which will be explained later in this chapter. Another way is by varying the voltage on a gate positioned in between the dot and

the electrode. The changing voltage will tune the strength of the coupling, which would enable the user to identify which extracted Γ belongs to that side.

Alternatively, increasing the source-drain bias will also enable a current to flow through the device. Doing so will increase the bias window until eventually, with high enough bias, a resonance will always lie inside the window and a current will flow continuously. The Coulomb peaks from Fig. 8.2c are taken at a V_{SD} of zero. At non-zero bias the peaks will widen, as the bias window increases. This behaviour is seen when a two dimensional map is taken of the gate voltage versus the source-drain voltage. A diamond pattern forms of areas where conductance is not allowed as seen in Fig. 3.5a. From these Coulomb diamonds it is possible to extract several parameters of the quantum dot. [28] The height of diamond represents the charging energy plus the energy level spacing. The energy level spacing can be found by noting at which bias the excited states appear. And finally the gate factor of the dot, α, can be extracted from the diamond via $\alpha = \frac{height}{width}$.

3.4 Alternative transport through a quantum dot

So far it has been assumed that only single electron transport is possible when a dot is in Coulomb blockade. However via a process called elastic co-tunnelling two electrons can travel simultaneously through the dot while in Coulomb blockade. Elastic co-tunnelling occurs when an electron from the source enters the dot and within the Heisenberg uncertainty time, τ, another electron leaves the dot to the drain. [29] The resulting current is proportional to V_{SD}, which means the differential conductance due to co-tunnelling is constant. When V_{SD} is larger than ΔE inelastic co-tunnelling starts to occur. Inelastic co-tunnelling involves the electron leaving the dot in an exited state. Co-tunnelling can be visible in the Coulomb diamonds as a conductance step inside the diamond. This step signifies the boundary between elastic and inelastic co-tunnelling and thus also indicates ΔE.

3.5 A quantum dot coupled to a superconductor

The electrical transport between a quantum dot coupled to a superconducting electrode is different than the N-QD junction discussed previously and gives rise to several transport phenomena. A result of the BCS theory on superconductivity is the existence of an energy gap in a superconductor at Fermi level. [16] A Cooper pair excited to an excited state in the superconductor will break apart into two charge carriers referred to as quasiparticles. When looking at the quasiparticle density of states, $D_s(E)$, one obtains a result which is very similar to that of semiconductors [15]:

$$D_s(E) = D_N(\eta)\frac{dN}{dE} = \begin{cases} D_N(\eta)\frac{E}{\sqrt{E^2-\Delta^2}} & (E > \Delta) \\ 0 & (E < \Delta) \end{cases}$$

where $D_s(\eta)dN$ is the density of states of free electrons. The important result is that there are no quasiparticle states at $(E < \Delta)$ meaning that the ground state is completely occupied by Cooper pairs. When considering the quasiparticle transport through a quantum dot coupled to both a normal and superconducting electrode, an arrangement fundamental to the CPS, the importance becomes clear. In the normal state the differential conductance in Coulomb blockade is caused by co-tunnelling. In the superconducting state this is multiplied by the density of states

of the quasiparticles. Since an ideal Cooper pair splitter needs exclusively Cooper pair transport, it is essential to keep the thermal energy below Δ.

There are other states that exist inside the superconducting energy gap, Andreev bound states, which are caused by a process called Andreev reflection. [30] Here, an electron with energy $E < \Delta$, momentum k and spin $\uparrow$ approaches an interface of a normal metal and a superconductor. The electron cannot enter the superconductor since it does not have enough energy to form a quasiparticle. With a high potential barrier the electron will just reflect normally, travelling back with a energy $E < \Delta$, momentum $-k$ and spin $\uparrow$. With a low barrier the electron can instead team up with another electron with energy $-E, -k, \downarrow$ and they both enter the superconductor as a Cooper pair as shown in Fig. 3.3. The electron with $-E$ will leave behind a hole, travelling away from the interface. Andreev reflection results in a current across the interface. Andreev reflection also occurs in Cooper pair splitter geometry where two electrons from separate leads combine to form the Cooper pair. It can also go the other way, with a Cooper pair splitting up into two electrons. This is called crossed Andreev reflection (CAR).

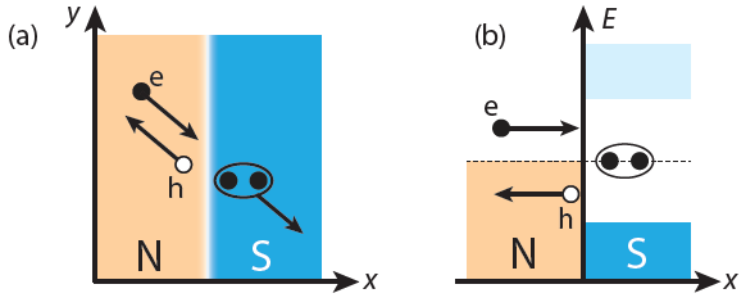

Figure 3.3: *A schematic of Andreev reflection. (a) illustrates the formation of a Cooper pair resulting from Andreev reflection at a metal-superconductor interface. The incoming electron with energy $E < \Delta$, momentum k and spin $\uparrow$ combines with a second electron with energy $-E$, momentum $-k$ and spin $\downarrow$ to form a Cooper pair. The second electron leaves behind a hole travelling away from the interface. (b) The situation shown in an energy diagram. Figure adapted from [22].*

Another type of an Andreev bound state are the Yu-Shiba-Rusinov (YSR) states, shown in Fig. 3.4 and Fig. 3.5. [31] [32] [33] These states, also called sub-gap states, appear inside the gap of the superconductor when electrons in a Coulomb blockaded dot tunnel to the quasiparticle states above the gap. This occurs only when the coupling of the quantum dot with the superconductor, Γ_S, is strong. The quantum dot has three different occupational states. It can have zero, one or two electrons occupying the resonance. The ground state can then be described by a singlet (zero and two electrons), often referred to as even, or a doublet (one electron), otherwise known as odd. Excitations involving the changing of the singlet and doublet ground state cause the observed sub-gap resonances. The shape of these states is shown in Fig. 3.4a-c and depend on system parameters such as the dot charging energy, U, the gate voltage, V_g and the coupling strength to the superconducting electrode, Γ_S. For a small $\frac{\Gamma_S}{U}$ the ground state changes from a singlet to a doublet and back to a singlet as the gate voltage is swept across the different dot occupations. Figure 3.4d illustrates this and shows that the corresponding sub-gap states in Fig. 3.4a have very sharp sign changes at the ground state transition points. As $\frac{\Gamma_S}{U}$ gets larger,

for example by increasing the strength of the coupling with the superconducting electrode, the sub-gap states have more gentle slopes. When $\frac{\Gamma_S}{U}$ is high enough, the ground state remains a singlet as is detailed in Fig. 3.4f and the sub-gap states do not cross each other any more, as shown in Fig. 3.4f. Figure 3.5b shows a bias spectroscopy plot showcasing the YSR states over a large plunger gate range. The states mostly correspond with the situation in Fig. 3.4b and Fig. 3.4e. The periodic size differences, also seen in the schematics in Fig. 3.4 allows the quantum dot occupations to be identified.

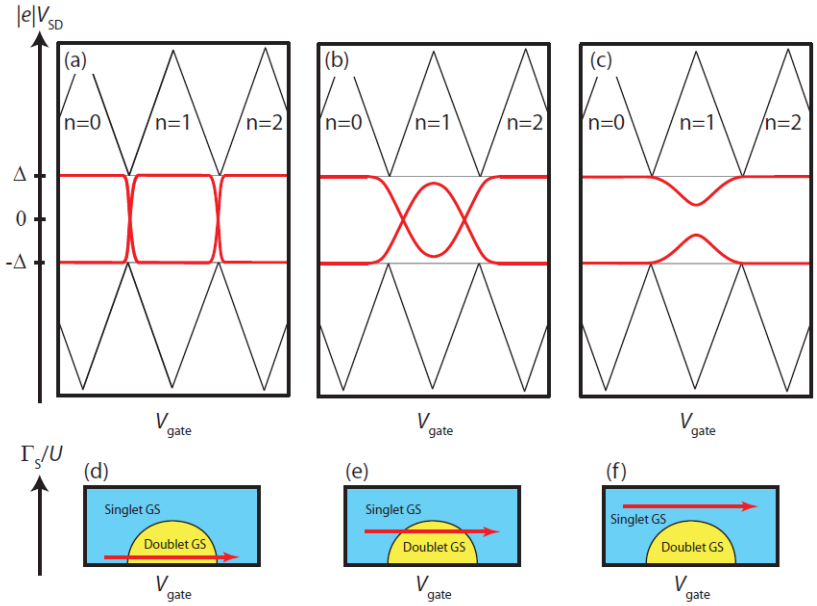

Figure 3.4: *A visualisation of the ground state transistions are shown in (d)-(f). A high* $\frac{\Gamma_S}{U}$ *results in the ground state remaining a singlet as the gate voltage is swept. As* $\frac{\Gamma_S}{U}$ *gets lower the ground state will transition to a doublet state. The resulting shape of the sub-gap states observable in a bias spectroscopy of the dot are shown above (a)-(c). The states overlap at the ground state transitions. This overlap is very sharp when* $\frac{\Gamma_S}{U}$ *is low (a),(d). As* $\frac{\Gamma_S}{U}$ *is increased, the shape of the YSR states become less sharp untill eventually they do not overlap (c),(f). The shapes can used to identify the quantum dot occupations indcated in the diamonds by n. Figure adapted from [22].*

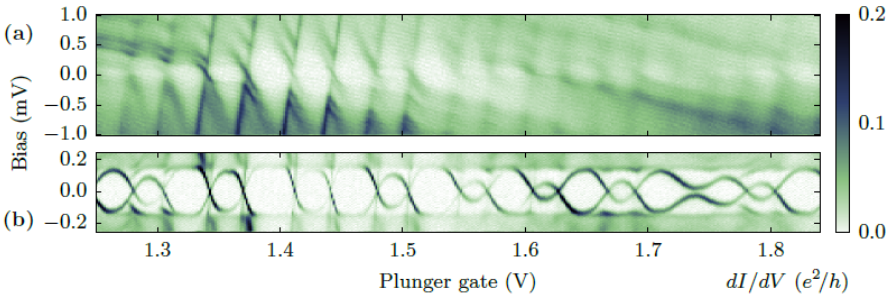

Figure 3.5: *An example of how YSR states look in a bias spectroscopy image. The top plot (a) has a longer V_{SD} range and shows the Coulomb diamonds of the dot, clearest in the plunger gate range of 1.3-1.5 V. (b) When zoomed in on the superconducting gap Δ the YSR states are visible. The crossings of the states correlate with the ground state transition as is schematically shown in Fig. 3.4. Figure adapted from [34].*

3.6 Cooper pair splitters

The goal of the Cooper pair splitter is to split the Cooper pair charge carriers into two spin entangled electrons. To achieve this the Cooper pair splitter is made of two N-QD-S junctions as shown in Fig. 3.6a. The two quantum dots are in Coulomb blockade and so only allow one electron to pass at a time. When a bias is put across the device the Cooper pairs have no choice but to split and let one electron through at a time. Ideally, an electron will go to each of the two normal leads and leave a spatially separated entangled electron pair, as shown in Fig. 3.6a. The Cooper pair electrons exit the superconducting electrode at a distance δr. The significance of this will be explained later.

As described previously the thermal energy k_bT must be smaller than the binding energy of the Cooper pairs, Δ. Similarly, the thermal energy of the electrons must not be able to overcome the charging energy of the dots, U, to not break to the Coulomb blockade. Furthermore the bias voltage V_{SD} cannot give the electrons enough energy to overcome these barriers either. This gives the requirement for a Cooper pair splitter:

$$k_bT\,,\, eV_{SD} \;<\; U\,,\, \Delta$$

A Cooper pair has the possibility to leave the superconducting electrode through one lead without splitting. Firstly, the pair can tunnel into the same lead via a process called pair tunnelling. [35] One electron will tunnel to the $\mu(N)$ resonance of the quantum dot and the second will tunnel to the $\mu(N+1)$ resonance of the same dot. Both will then be able to tunnel to the metal electrode. Secondly, an electron from a Cooper pair can be excited to a quasiparticle state. [35] The other electron tunnels to the quantum dot. When it leaves the dot and tunnels into the metal lead, the excited electron can then tunnel into the same metal lead via the dot. This is called sequential tunnelling. Fortunately, both these processes can be suppressed to insignificant levels by adhering to the requirements listed earlier without hampering the splitting probability.

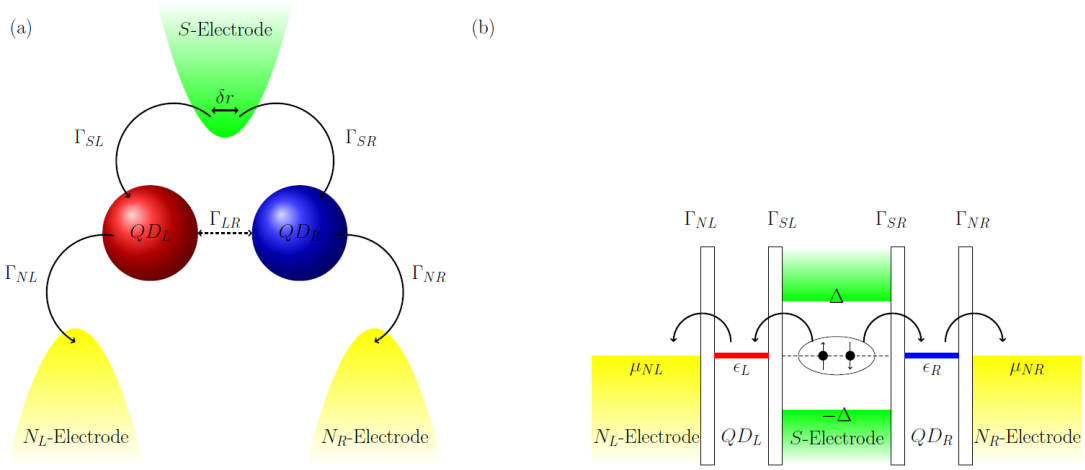

Figure 3.6: *The basic structure and potential energy diagram of a Cooper pair splitter. (a) shows two entangled electrons leave the superconducting electrode at a distance of δr. The arrows indicate tunnelling actions made by the electrons. The tunnelling to a quantum dot is regulated by the coupling strengths denoted by the $\Gamma's$. The dots are also slightly coupled to each other, shown here as Γ_{LR}. (b) The potential energy diagram of the situation in (a). The entangled electrons from the Cooper pair in the superconductor ground state tunnel towards the normal metal electrodes when the resonances in the quantum dot (ϵ) are equal to the chemical potentials the N-electrodes (μ). The gap of the superconductor is given by Δ.*

The strength of the coupling of the quantum dot with the electrodes is also important and are listed in Fig. 3.6a. The arrows indicate tunnelling actions of the electrons and with it are the relevant $\Gamma's$. Figure 3.6b shows the potential energy diagram of a Cooper pair splitter, providing a clear view of the tunnel actions that the electrons have to perform. The total coupling strengths of the left and right quantum dots are made up of the coupling with the normal and superconducting electrodes: $\Gamma_L = \Gamma_{LN} + \Gamma_{LS}$ and $\Gamma_R = \Gamma_{RN} + \Gamma_{RS}$. There also exists an inter-dot coupling, Γ_{LR}, between the two quantum dots.
With a high inter-dot coupling, a split Cooper pair can reform by tunnelling from one dot to the other. [10] To prevent this the normal electrode has to be strongly coupled so that $\Gamma_N \gg \Gamma_{LR}$. In this regime the electrons are much more likely to tunnel out into the normal leads thus reducing the probability of reforming via inter-dot travel. Similarly, having $\Gamma_N \gg \Gamma_S$ will allow for electrons occupying the dots to leave to the normal electrode before new Cooper pair electrons can arrive. Naturally, it is beneficial when the electrons occupy the dots for the shortest time possible, allowing for a high Cooper pair current. The coupling strength relations can be added to the requirements of building an ideal Cooper pair splitter:

$$k_bT\,,\, eV_{SD} \,<\, U\,,\, \Delta \qquad \Gamma_N \gg \Gamma_{LR}\,,\, \Gamma_S$$

When all these requirements are met, a Cooper pair splitter can perform with 100% efficiency. However, even with perfect splitting efficiency, the entanglement of the Cooper pairs can be destroyed after splitting. One of these processes is when an entangled electron in the quantum dot is switched with a random electron. This occurs when the energy level spacing, ΔE, is small, so that the quantum dot acts like a capacitive island and any electron from the dot is able to leave to the normal electrode. The result is non-entangled electrons entering the normal lead. A high level spacing, $\Delta E \gg k_bT\,,\, eV_{SD}\,,\, \Gamma$, will prevent this problem since the electrons in

the dot will not have enough energy to jump to the $\mu(N)$ resonance occupied by the entangled electron. It is also beneficial for this resonance to be empty to rule out any correlations with other electrons. Lastly, the required strong Γ_N coupling could allow electrons from the normal electrodes to tunnel to the quantum dots and interact with the Cooper pair electrons. This process is limited by maintaining a high enough bias voltage while keeping the resonance of the quantum dot level with the chemical potential of the superconductor: $eV_{SD} > \Gamma$ while $\mu_{QD} = \mu_S$

The complexity of the system becomes clear by the large number of rules and balances that it must adhere to. Using the Cooper pair splitter as a reliable entangled electron source requires even more requirements, such as high spin de-phasing times. However, that is slightly out of scope of this thesis.

3.7 Current through a Cooper pair splitter

There have been several ways to define the current and differential conduction through a Cooper pair splitter device. Often, a paper on a new CPS device defines their own, different definition of these parameters. While it is important to understand these definitions, and so understand what influences the current, it is not essential here to build a new theory as this thesis mostly concerns itself with measuring relative differences between measurements. We will however look at some previous papers to get a good picture of the typical current in these devices.

Hofstetter et al. [9] assumed a non-interacting picture and defined the transmission probabilities of the entangled electrons through the two dots as T_1 and T_2. The transmission probabilities depend on the parameters of the quantum dot junction such as the tunnel barriers, charging energy and quantum dot resonances. If both transmissions are small, then the probability of tunnelling through a dot as a pair (known as local pair tunnelling or LPT) is given by T_1^2 or T_2^2. The splitting probability is proportional to $\rho(\delta)T_1T_2$ where $\rho(\delta)$ is the probability of finding two electrons of a Cooper pair at opposite ends of the superconducting contact. Therefore the total conductance through quantum dot 1 G_1 is proportional to:

$$\alpha T_1^2 + \rho(\delta)T_1T_2$$

So the model predicts a positive non-local signal caused by Cooper pair splitting. This was also seen in the experiment but only when the transmission was low. At higher energies the ideal CPS requirements were likely not satisfied any longer, causing other transport processes to take over .

Earlier Recher et al. [36] performed a much more thorough analysis. Their thought experiment on a device with a Cooper pair splitter geometry starts with defining its Hamiltonian. Using the T matrix method they arrived at an expression for the current due to entangled electrons through one dot:

$$I_1 = \frac{e\Gamma_s^2\Gamma_N}{(\mu_1+\mu_2)^2 + \frac{\Gamma_N^2}{4}}\Big[\frac{sin(k_f\rho(r))}{k_f\rho(r)}\Big]^2 exp\Big(-\frac{2\rho(r)}{\pi\xi}\Big)$$

The subscripts 1 and 2 refer to quantum dot 1 and 2 respectively. Γ_S and Γ_N refer the the dot's coupling to the superconducting and normal electrodes. μ refers to the resonance in the quantum dot. $\rho(r)$ is the distance between the exit points of the electrons in the superconductor. ξ is the coherence length of Cooper pairs and k_f is the Fermi wave vector.

Both theories show that the splitting current is dependent on the transmission through the dot and that the coupling with the electrodes plays a major role. While this may seem obvious it is useful to see its importance and it underlines the goal of this thesis where we use a 15 gated device to have major control on the coupling strengths. Another attribute both definitions share is the inclusion of the exit points of Cooper pair electrons from the superconductor, denoted by $\rho(\delta)$ or $\rho(r)$. A higher current occurs when the electrons leave the superconductor at the sides. It is therefore essential for an ideal CPS that the width of the superconducting electrode is less than the spatial extent of a Cooper pair. The spatial extent is reflected in the coherence length of the superconductor where a long coherence length allows for 'wide' Cooper pairs. This is reflected in the above equation by the exponential term, which greatly suppresses the Cooper pair current when the coherence length ξ is smaller then the exit points $\rho(r)$. The device used in this thesis has a 100 nm wide aluminium contact used as the superconducting electrode. Aluminium has a coherence length in the µm range [37], meaning the Cooper pairs can easily exit at the sides of this electrode thus maximising the Cooper pair current.

Chapter 4

Fabrication

Fabrication of the nanowire devices is a very delicate and precise process, consisting of a series of steps that need to be completed properly. And even correctly fabricated devices can fail. All the effect and processes at the nano scale are simply not fully understood yet. As a result the fabrication process is relatively slow and it is very hard to produce a large number of successful devices at the same time. For a quantum computer, which would need many nano devices on its chips, this is a real bottleneck. There is no ideal way of fabrication at this time. Many groups use their own methods, often based on the materials chosen and the equipment available. In this chapter, I will go through the most popular methods of the fabrication of Cooper pair splitter devices, describing the techniques and procedures used at each step. I will focus on instruments that I have trained on and are therefore more familiar with, but I will to include all the relevant techniques used in the field. At the end, the device used in this thesis is presented.

4.1 The silicon wafer

The basis of a new Cooper pair splitter device is typically a silicon wafer. These wafers form a good working platform on which to build the device. Since silicon is a semiconductor it can also serve as a general back-gate to perform device wide tuning of the electrostatic potentials as well as the possibility of accepting donor materials to change the wafer to an n- or p-type semiconductor [38]. Silicon is used because it can be grown as an extremely pure crystal. [39] The silicon wafers allow more control on the electronic properties by cutting along a specific crystalline orientation as electron transport through silicon is anisotropic [38].

Often however the proposed chip is smaller than the wafer. In this case the wafer can be cut to the desired size using a scribing tool. For rough resizing this can be done by hand. A small cut is made at the edge of a wafer and it is then snapped along the small cut. Alternatively, a diamond tip can be used in combination with a microscope to make extremely precise cuts.

4.2 Imprinting the design

Before fabrication of the chip can begin, the design has to be 'imprinted' on the wafer. The first part of the design is called the base chip.

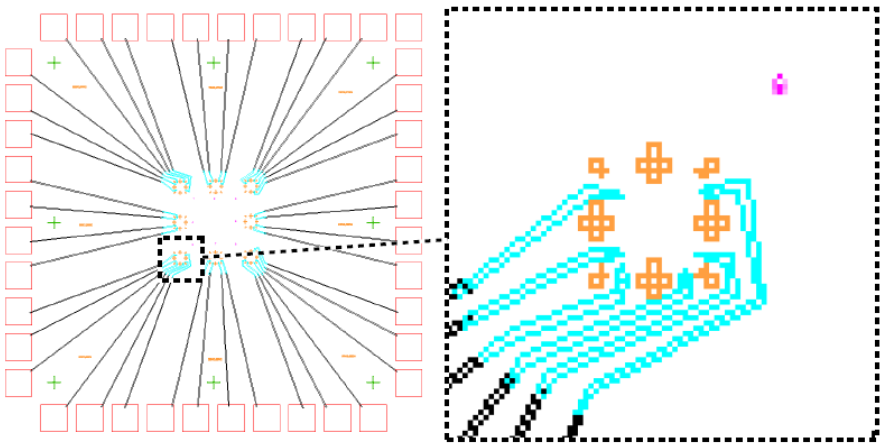

Figure 4.1: *An example of a base chip design. This one in particular was part of the first generation of devices made by Kasper Kirkholt for his thesis. The red squares on the outer edge serve as bonding pads to connect the chip in the cryostat. From these bonding pads metallic leads head towards the area where the nanowire and eventually the device will be located. The change of color is just a stylistic choice and does not indicated a difference in material. This area is highlighted in the zoomed-in cut-out and is surrounded by gold coloured alignment marks, used to align several fabrication instruments. Unfortunately the resolution is a bit low, which is a limitation of the software. This base chip design has a total of 8 deposition areas.*

The base designs used to create nanowire devices, such as the one shown in Fig. 4.1, typically have several common features. The relatively large red squares on the outer edge in Fig. 4.1 serve as bonding pads. The pads will consist of a slab of metal, which will make contact with the leads in the cryostat to connect the device to all the instruments. From the bonding pads thin leads propagate towards the area where the device will be. This area is inside the yellow pluses in the zoom-in of Fig.4.1. These leads move all the way to surround the nanowire deposition area to make it easy to connect to the electrodes and gates of the device, linking them up to the measurement setup.

There are multiple ways of imprinting a design on the wafer. Most are based on the principle of lithography. Personally I have had experience using LED lithography where a photo-reactive resist on the wafer is exposed to a LED light source.
In LED lithography a few drops of a photo-reactive resist are placed on the wafer. It is then placed on a spinner to evenly distribute it across the surface. Soon after the chip is placed in an LED exposer, in our case an Heidelberg LED writer. This instrument is able to follow the design precisely with a high power LED light source that exposes the photo-reactive resist. The exposure to the LED light enables the resist to become soluble to a specific chemical called a developer. When the chip is submerged in the developer, the soluble resist washes away and an imprint of the design is left in the remaining resist as shown in Fig. 4.2. This type of resist is also know as a positive resist. [40] For a negative resist, The exact opposite process happens and the unexposed areas will dissolve instead.
A more common option to forge the design is using e-beam lithography. The fundamentals are the same, with a resist coating, typically PMMA, on top of the wafer. A high energy electron beam then writes the design into the resist analogous to the LED writer. This exposes the resist

and allows it to be removed from the chip and leave the design imprinted on the wafer. Besides e-beam and the LED exposure, the same principle can be applied using ions or x-rays to etch away a resist.

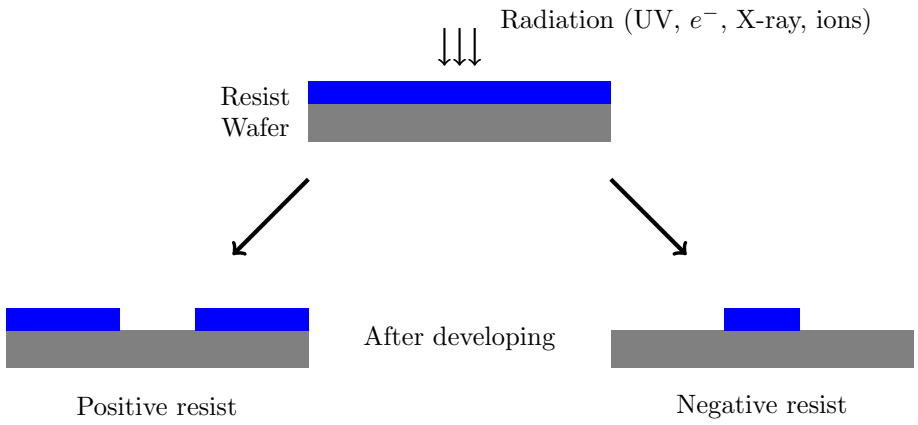

Figure 4.2: *The difference between a positive and a negative resist. Radiation, usually UV or an electron beam, hit the resist and exposes it. With a positive resist the exposed area dissolves in the developer and leaves a troth behind. A negative resist is the opposite, with the exposed resist becoming insoluble to the developer.*

After exposure the chip is generally ashed for a short time. This is in order to remove any residual resist that may not have fully been dissolved, which can cause the metal to not deposit properly onto the wafer. The chip is placed in the ashing chamber under a Faraday cage. An oxygen plasma will fill the vacuum chamber, oxidising the resist, which is then pumped away, leaving clean troths. The process is showcased in Fig. 4.3

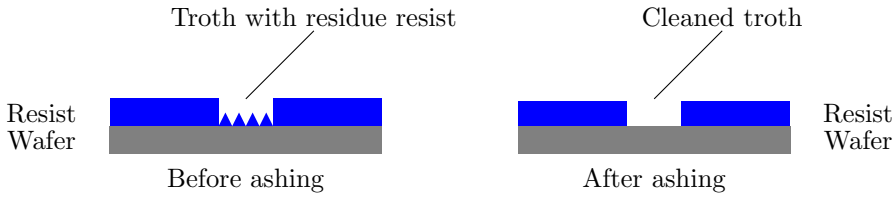

Figure 4.3: *The result of ashing to clean the troths. The exposure of the design is not always perfect and some resist may not have dissolved in the developer, leaving a thin layer of residue resist in the troth. This is a problem since the metal will not deposit directly on the wafer. Ashing cleans the thin layer away by oxidising the resist with a oxygen plasma, removing a uniform layer.*

4.3 Metal deposition

With a smooth imprinted design the chip is ready for metal deposition. One way is using an e-beam evaporator, in our lab we have several AJA instruments inc. systems. The chip is placed

in a ultra high vacuum chamber. A high energy electron beam then hits a sample of metal positioned inside the chamber. The electron beam melts the metal and the metal molecules are thrown into the vacuum chamber and subsequently land on the chip. The metal forms a fairly uniform layer over the entire chip. When the metals are all deposited to their desired thickness, the chip is removed and the lift off process can start.
An alternate way is sputtering where instead of a e-beam a plasma, usually argon hits a target and kicks out a few atoms at a time towards the device. Sputtering is especially useful when wanting deposit compounds or mixtures that would typically deposit at different rates in e-beam lithography.
Molecular beam epitaxy (MBE)is another option when a lot control is needed. MBE enables the deposition of one atomic layer at a time by directing slow streams of elements at the chip.

Lift off is similar to the developer dissolving the resist described earlier. The chip is submerged in a chemical which allows the resist to release from the chip, taking with it the metal deposited on it. The metal deposited straight on the wafer in the troths will stick leaving the metal in the shape of the design behind. The result of metal deposition and lift-off is detailed in Fig. 4.4. The resulting chip is called the base chip.

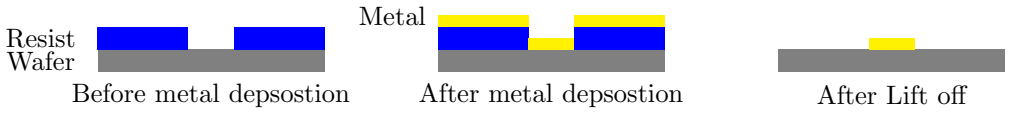

Figure 4.4: *A schematic of the chip during metal deposition and lift-off. Metal is deposited uniformly on the chip, landing both on the resist and the wafer. During the lift-off process the resist will release form the chip leaving just the metal that was directly deposited on the wafer.*

4.4 Nanowire deposition and contact

With the design now imprinted in metal on the wafer the nanowire can be deposited. One way is using a micro manipulator. This instrument uses a small needle, around 0.1 to 0.25 µm thick at the tip, to grab a nanowire grown on a separate growth chip and drop it in the desired area of the wafer. The benefit of using this method is that many different types of wires can be used, even on the same chip. However it is very tedious and slow, with many wires failing to drop or break apart during deposition.
Instead one can choose to grow a large selection of nanowires directly on the chip. When a suitable wire is located the device is fabricated around this wire. Another option is placing a catalyst inside the fabricated base chip and instigating nanowire/tube growth, which can then be contacted with a second deposition step. This cuts down on the search of finding a suitable nanowire.

After the base design is built and the wire is in position, a second lithography step is done to contact the nanowire. The process is the same as in the first step, although now the design of the electrodes and gates is made based on the location of the wire. Generally, before the nanowire is contacted, an oxide layer on the wire has to be removed. As the nanowire is exposed to the air during fabrication, an oxide layer will grow on it, which can hamper the metal-wire contacts. Via a process called milling, the layer is removed right before the contact metal deposition. Milling involves firing ions, generally argon, at the sample to sputter away the oxide. With the wire successfully contacted the device is finished.

The finished device is then placed in a probe station where the conductivity of the device is tested. This is necessary as it is very time consuming and pointless to place the device directly in the cryostat when it is unknown if the fabrication has been successful. In the probe station the electrodes are connected and a current is run through the device. Devices with good conductivity can be placed in the cryostat.

4.5 The device used in this thesis

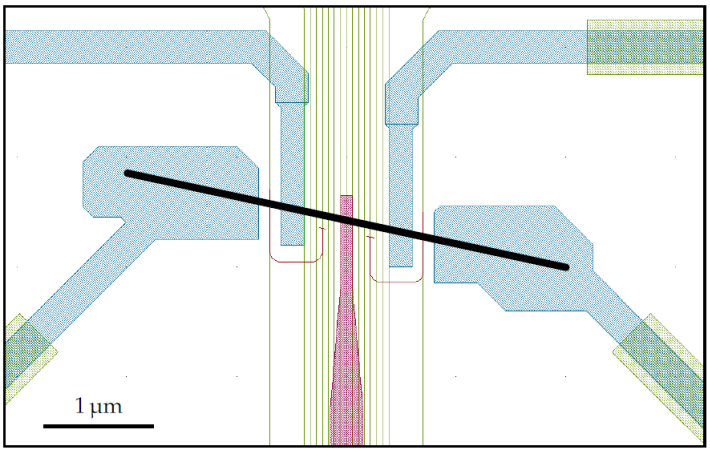

Figure 4.5: *The design of the device used in this thesis. It has the typical Cooper pair splitting geometry, with a superconductor in the centre, indicated in purple, and two normal metal electrodes at the edges (the blue rectangles entering the image from the top), connected by a InAS nanowire. The superconducting contact is made of Al/Ti (95 nm / 5 nm) and contact the nanowire over a 100 nm wide section. The normal metal electrodes consist of Au/Ti (90 nm / 5 nm) The 5 nm titanium layer serves to improve the contact of the electrodes with the wire. Between the two normal electrodes are 15 Au/Ti (12 nm/ 5 nm) bottom gates separated by a 24 nm layer of hafnium oxide serving as the dielectric barrier between the wire. image 3.8 from AJthesis*

The device used in this thesis was fabricated by Anders Jellinggaard during his PHD thesis. [41] [34] The design used for the fabrication is shown in Fig. 4.5. The device was built on a 100 mm wide and 500 µm thick heavily doped silicon wafer. The wafer is capped with a 500 nm thick layer of SiO_2. The superconducting contact consists of a 95 nm thick layer of the superconductor aluminium on top a 5 nm thick layer of titanium. The titanium layer helps improve the contact with the nanowire. The contact with the InAs nanowire, indicated by the black line in Fig. 4.5 is 100 nm wide. The wire has a diameter of 70 nm. Under the superconducting contact there is one bottom gate used to tune the potentials inside the superconductor and the inter-dot coupling. This gate is referred to in the experiment as gate 8. The gates are represented by the thin green lines in Fig. 4.5. The bottom gates are made of a 12 nm thick layer of gold with a 5 nm layer of titanium to aid the contact. A 24 nm thick hafnium layer acts as the dielectric barrier between the gates and the wire, ensuring that the gates are only capacitively coupled.

There are two normal leads on either side of the superconductor. In Fig. 4.5 these are the two thick blue lines coming down from the top of the device. They consist of a 90 nm layer of gold on top of a 5 nm layer of titanium. Between each normal lead and the superconductor are 7 bottom gates. These are equidistantly placed in a 330 nm wide section below the nanowire. As a result there are in total 15 bottom gates capable of manipulating the electrical environment of the device. The 7 gates on the left side are referred to as gate 1-7, the right side as 9-15.

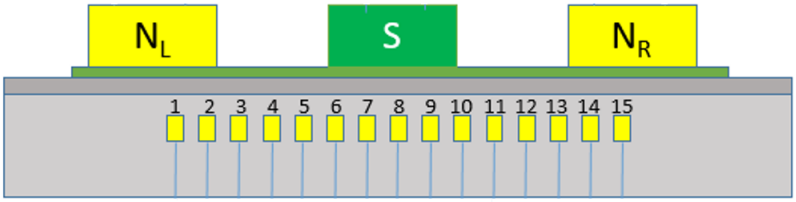

Figure 4.6: *A simplified schematic of the device, with the normal and superconducting electrodes and the 15 bottom gates indicated. The location of the gates is crucial in deciding their role in the measurements. Gate 4 and 12 are both in the center between the electrodes, right underneath the centre of the dots. Therefore these gates are used as plunger gates, moving the resonances in the dots. Gates 2, 6, 11 and 14 are used to tune the strength of the coupling of the dots with the electrodes. Gate 11 is used instead of gate 10 because gate 10 was found to be unstable.*

A simplified schematic of the device is shown in Fig. 4.6. The gate locations are important as they indicate what the gate can tune. When the device is cooled two quantum dots will form on each side of the superconducting electrode. Gate 4 and 12 are located close the the centre of these dots and therefore are used as the plunger gates, which will tune the resonances of the dots. The coupling to the normal electrodes is tuned using gate 2 and 14. These gates are close to the edge of the dots and thus should have the greatest effect on the coupling strength. Using for example gate 3 or 5 will also have a fairly strong effect on the resonances in the dot while using gate 1 or 15 will affect the electrodes too much. When tuning the coupling between the dot and the superconducting electrode, gate 6 and 11 are used. Gate 6 is located close the dot's edge as gate 2 and 14. Gate 10 would be a better option to tune Γ_{SR} with, but it was found to be very unstable and therefore gate 11 was used instead.

There are two additional Au contacts fabricated adjacent to the two normal leads. In Fig. 4.5 these are represented by the blue rectangular-like shapes on the outer edge of the device. Underneath the 200 nm wire segment there is a additional bottom gate. These contacts are coupled capacitively to the main device through flouting gates and can be used as sensor dots. However they were not used in this thesis. The full recipe for the fabrication of this device can be found in [41].

Chapter 5

Method

As superconductivity is necessary for a working CPS, the device must be held at ultra cold temperatures. To achieve this, the Cooper pair splitter is placed inside a cryostat, where it is cooled to about 40 mK. The cryostat is connected to the instruments and the control computer, where the data is processed and analysed. This chapter will discuss the instrument set-up, with a description of the use of each instrument.

5.1 Instrument setup

The cryostat used in the experiment was an Oxford instruments Triton 200 system. Triton 200 is a cryofree dilution refrigerator capable of ultra low temperatures down to 20 mK. It uses a mixture of ^3He and ^4He as its cooling agent. The cold parts of the system are enclosed by a vacuum chamber, which includes the sample. The device is connected to the electrical circuit in the cryostat via the bonding pads on the device. These wires first pass through a set of filters before reaching the breakout box, which is outside the cryostat. The breakout box serves as the connection to the cryostat for the instruments. Each wire inside the cryostat is connected to an output on the breakout box, e.g to put a voltage on a specific bottom gate, a bias has to be set on the output. The breakout box is isolated from ground and care must be taken to ensure that all incoming signals are isolated as well to minimise the noise and avoid ground loops. The cryostat is suspended from the ceiling using a specially designed frame to minimise the effect of vibrations. This cryostat also had an internal 8-3 T magnet to apply a magnetic field around the device during ultra cold temperatures.

Intuitively, the conductance through the dots is able to be measured using a simple 2-terminal measurement as shown in Fig. 5.1. A voltage is applied on the superconducting electrode. This voltage will induce a Cooper pair splitting current to the normal electrodes which will be measured by instruments connected to the normal electrodes.

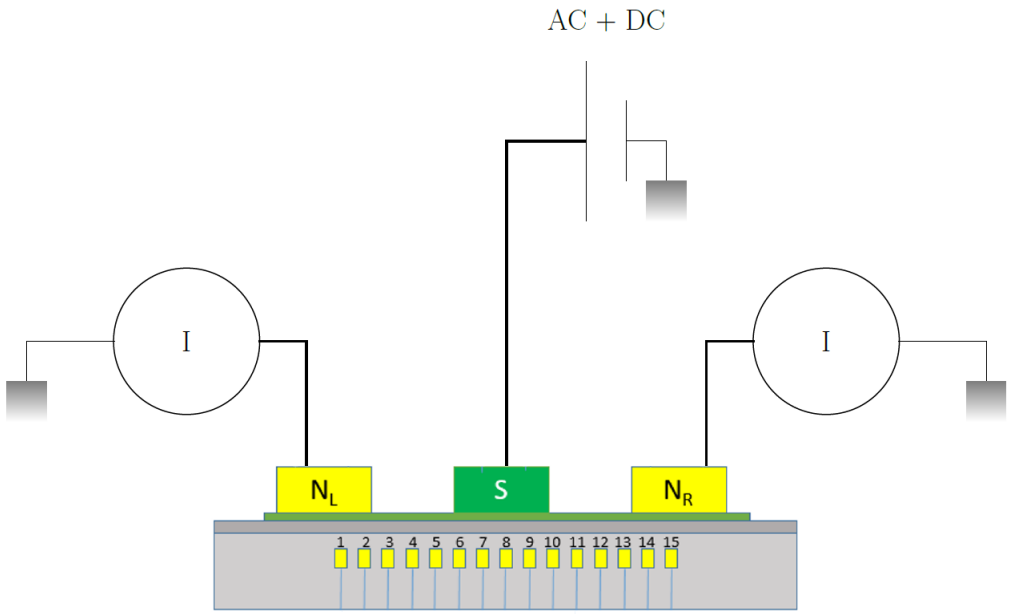

Figure 5.1: *A setup of a 2-terminal measurement of the Cooper pair current. The source generates a AC+DC current on the superconducting electrode, which will induce a Cooper pair splitting current through the dots. This is measured by the current measurements on the normal electrodes. Filters in the cryostat prevent this type of measurement setup*

Unfortunately, filters in the cryostat prevent the use of a 2-terminal setup. The filters introduce a resistance in the lead, making the source bias unable to be used as the voltage drop across the dots. Instead a 4-terminal measurement is needed to extract the conductance through the normal electrodes. A schematic of such a setup is shown in Fig. 5.2. The setup consists of three groups of instruments which are color coded. The red group applies the bias to the superconducting electrode as in the 2-terminal setup. The blue group measures the current in the normal metal electrodes as before. The new green group measures the voltage drop across the dots. As a result each electrode now has two connections.

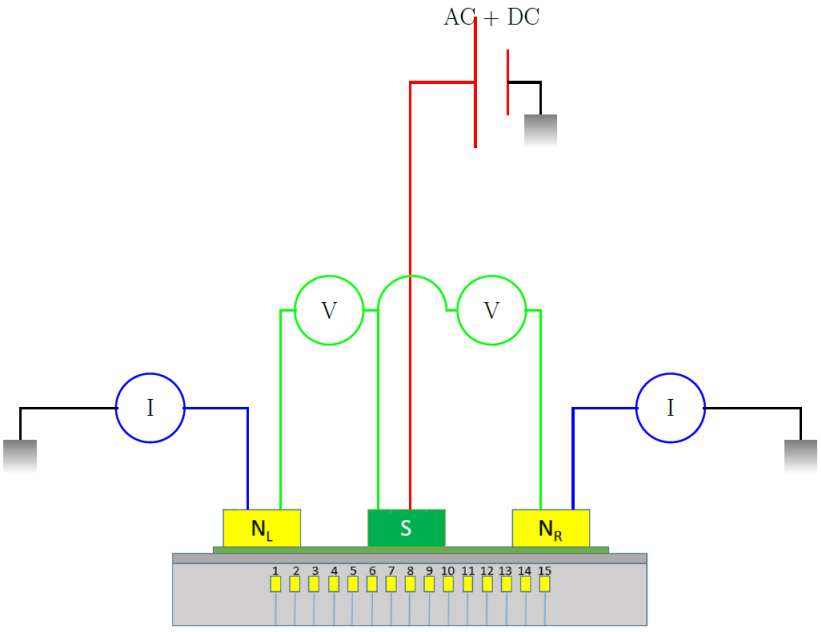

Figure 5.2: *A 4-terminal measurement setup to measure the CPS conductance. The color code refers to the task of the instruments. The red group is the source from Fig. 5.1 and the blue group the current measurements. The new green group measures the voltage drop across the dots. This setup is the one used in this experiment.*

The full experimental setup is displayed in Fig. 5.3. The color code from Fig. 5.2 is also used in this figure, indicating the task of the instruments.
The bias is generated in the red group by a Stanford research SR830 lock-in amplifier and a Harvard instruments 16 bit digital-to-analog converter (DAC) output resulting in a combined AC and DC source voltage. It has the added benefit of reducing noise as the signal is generated and measured at a signal frequency. The lock-in amplifier generates a voltage at 121 Hz. 121 Hz is chosen since it was not near any ground loop harmonics. Its signal is first passed through an isolator to remove the signal from ground and then divided by a factor of 10000. This is necessary to get the signal to the relevant energy scales of $\sim K_bT$. Afterwards the AC signal joins up with the DC signal and connects to the break out box, which then connects it to the superconducting electrode. The DC signal is outputted from a DAC output. The DAC is connected to the computer from which a DC voltage can be set, after which it passes through a voltage divide set to 1000:1. This brings the DC signal to an appropriate resolution of 300 nV with which to modulate the AC signal.

The bottom gates of the device are all connected to the DAC via the breakout box. Each gate is connected separately by a wire to its own DAC output. In Fig. 5.3 these wires exiting the cryostat are represented by a single wire. Similarly to the DC signal, a voltage can then be selected on the computer to run through the gates. The plunger gates of this device, gate 2 and 4, have an additional connection. This extra connection divides the DC voltage by a factor of 200 to enable a higher sweep resolution of these gates when needed. To ensure that the noise is kept to a minimum, every connection of an instrument to the PC is first converted to an optical signal from a GPIB connection and then back to a GPIB. This ensures that the instruments

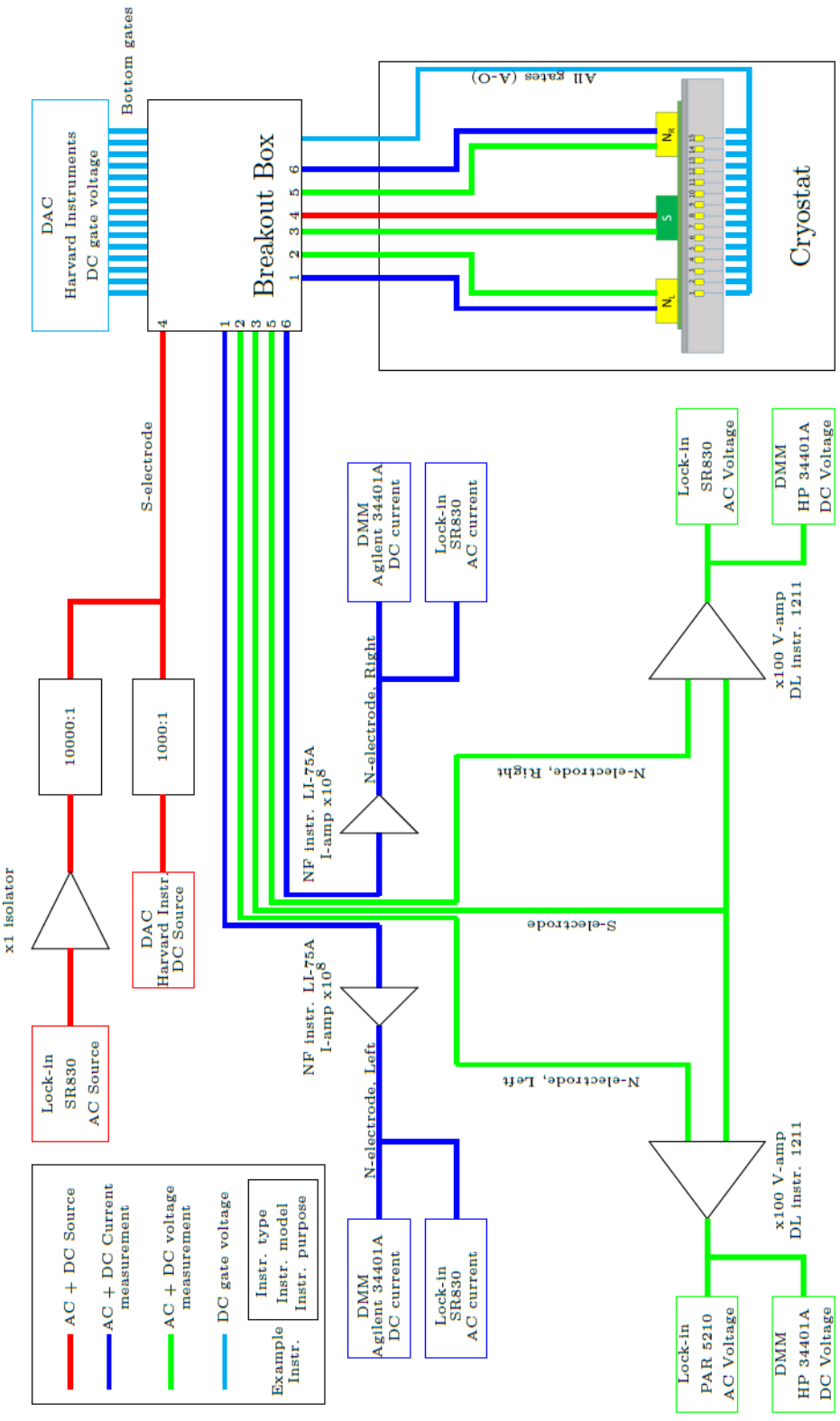

Figure 5.3: *The full instrument setup used for all measurements in this thesis. The color code from Fig. 5.2 is kept, indicating the task of the instruments. Each instrument is represented by a rectangle, or triangle in the case of the amplifiers. The instruments that are connected to the analysis computer are highlighted by a coloured rectangle. Each connection to the computer consists of a conversion of a GPIB signal to an optical and back again before reaching the PC. This is to ensure the instruments are isolated as much as possible to reduce the noise. The connections in the breakout box are numbered or lettered, with the numbered lines connecting via the breakout box.*

remain isolated from ground.

The blue instrument group measures the current on the normal electrodes. Each normal electrode is connected via the breakout box to a NF instruments LI-75A pre-amplifier. The gain on the amplifiers is set to 10^8. The signal is then connected to a Agilent 34401A digital multimeter (DMM) and a SR830 lock-in amplifier. The DMM and lock-in amplifier measure the current through the dot and are both connected to the PC which reads the signal.

The green instrument group measures the voltage across the dots. The two normal electrodes connect to a DL instruments 1211 voltage amplifier which is set to amplify the signal by a factor of 100, necessary to make the signal readable by the instruments. To these amplifiers the lead from the superconducting electrode connects as well, after it splits into two. The voltage on the electrode is compared and the signal from the amplifier then leads to HP 34401A DMM's and a SR830 or Princeton apllied research 5210 lock-in amplifier which measure the AC and DC voltage drop across the dots.

The computer processes all the data from the instruments via an analysis program written in Matlab by Anders Jellinggaard. At each measurement the computer collects the data from all the instruments in the left dot, the right dot or both. The program then enables the user to select from a menu which images are to be generated, e.g a ΔG or η plot. All images in thesis thesis are generated using this custom program.

Chapter 6

Results and Discussion

In this chapter I will present data collected on the Cooper pair splitter device and discuss the result and observations made. The data was collected in two steps. Firstly, measurements were taken to determine the parameters of the dots, needed to check if the device met the ideal Cooper pair splitter requirements. Afterwards the couplings strengths were measured to determine the regime of each dot. Finally the non-local signal is measured. Initially just one peak crossing is investigated to explore the nature of the ΔG signal. Then 32 peak crossings are investigated giving an unprecedented picture of the non-local behaviour.
Secondly, the bottom gates on the device are used to tune the coupling strengths. The relevant bottom gates are first used to find the voltage at which the quantum dot changes regime. Having mapped out the gates, the non-local signal is measured while the device is brought to several different configurations, including the ideal configuration as suggested by the theory. Visibility is generally used to compare the effectiveness of a regime, with a high visibility being desirable.

6.1 Detection of the non-local signal

With the working device inside the cryostat, large range sweeps of the source-drain voltage, (V_{SD}), against the plunger gates are done to find well conducting regions of the quantum dots. These are area with high conductance and well defined Coulomb peaks. With these regions found, smaller range sweeps are taken only including a few Coulomb peaks. The bias spectroscopy plots allow for the investigation of the Coulomb diamonds and with it, the parameters of the dots, such as U_c and ΔE, can be determined.

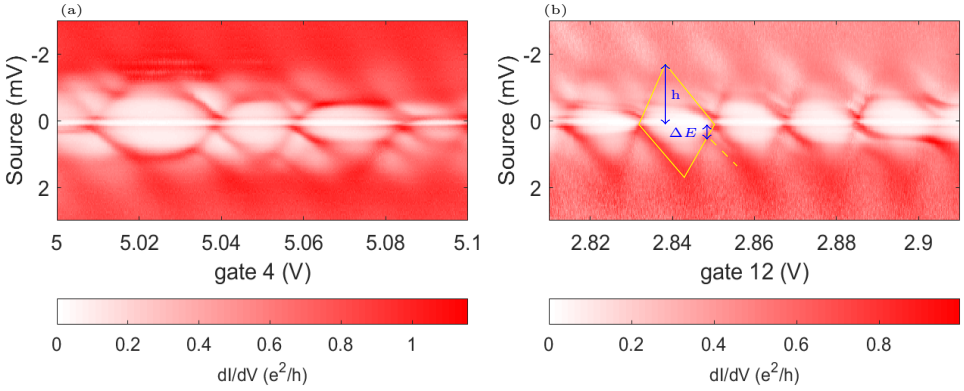

Figure 6.1: *The bias spectroscopy of the left (a) and right (b) quantum dots. Gate 4 and 12 are the plunger gates of the dots. The plots were both taken with the device in the superconducting state at $T = 40mK$ with $B = 0$. A Coulomb diamond in the right dot has been highlighted by a solid yellow line. The dashed yellow line indicates the first exited state, starting from the diamond at a height ΔE. The blue parameters refer to the values that can be extracted from the Coulomb diamond.*

In the bias spectroscopy plots of both dots from Fig. 6.1 a Coulomb diamond is visible, although the left dot is not as clear. This means that quantum dots have formed on the wire and that they are in Coulomb blockade. From the Coulomb diamonds several parameters can be extracted. The Coulomb diamond has been highlighted on Fig. 6.1 in yellow. Firstly the charging energy of the dots, U_c, is determined by looking at the height of the Coulomb diamonds, h, via the relation $h = \frac{U_c + \Delta E}{e}$. Figure 6.1b these parameters highlighted in blue. Starting with the right dot, the height of the diamond is 1.7 mV. ΔE, the energy level spacing, is 0.4 mV. This value also contains the energy gap Δ, which is around 120 mV. This can more clearly be seen later when zooming in on the gap, especially in Fig. 6.2d. Lastly, using the height determined earlier, and the width of the diamonds, the gate factor is calculated via $\alpha_L = \frac{h}{Width} = \frac{1.7}{19} = 0.089$. This parameter is useful for analysing the coupling strengths later. The same process is done for the left dot giving the results shown in Table 6.1.

Parameter	Left dot	Right dot
U_c	1.5 mV	1.3 mV
ΔE	0.7 mV	0.4 mV
α	0.073	0.089

Table 6.1: *The extracted parameters of the dots from the bias spectroscopy in Fig. 6.1.*

The measurements are all done at a temperature of 40 mK where the thermal energy is $k_b T = 3.5$ µeV. A successful Cooper pair splitter needs to have a thermal energy well below the energy scales of the device. Table 6.1 confirms that this is the case. The charging energies and ΔE are of the same order as other nano-electronic devices. Along with the fact that there is little difference between the two dots, this all points towards a successful fabrication.

The next goal is to look closer at what happens inside the gap at low source bias to inves-

tigate the sub-gap states. The plunger gates on both dot will be swept across 0.1 V and the conductance measured at constant $V_{SD} = 0$ V. This will provide a picture of both the shape and size of the Coulomb blockade peaks. Additionally, sweeping in normal state as well will give the opportunity to investigate the coupling strengths of the dots with the normal and superconducting metal electrodes.
Secondly, a bias spectroscopy is made over the same plunger gate range. This is to get a more complete view of the coupling and electrostatic environment of the device. The results of the measurements are shown in Fig. 6.2.

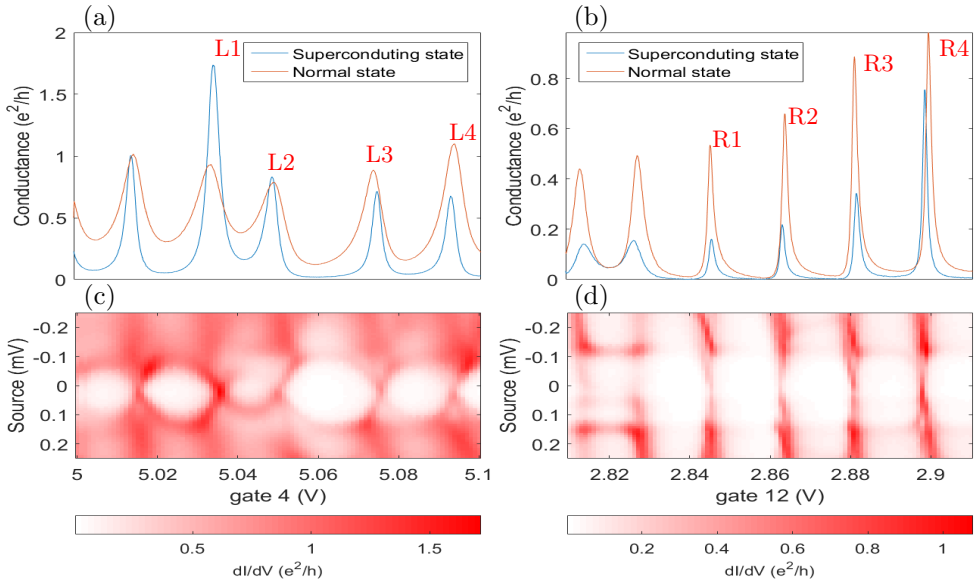

Figure 6.2: *(a) and (b) show the conductance in the normal and superconducting states plotted against the plunger gates of the respective dot. Both plunger gates were swept over a range of* 0.1 *V. The peaks that will be investigated further have been given a label shown in red on the two figures. L refers to the left dot, R to the right. (c) and (d) shows the bias spectroscopy taken in the superconducting state. The x-axis is the same as the 1D conductance plot above. As a result (a)and (b) can be interpreted as taking a cut through (c) and (d) respectively in the superconducting state at* $V_{SD} = 0$ *V.*

Figure 6.2 shows many differences between the two dots. The left dot in Fig. 6.2a shows that the normal state conductance is fairly equal to the superconducting state with exception of $L1$. This is in contrast with the right dot in Fig. 6.2b where for all peaks the normal state is larger. This suggests that the right dot is less strongly coupled. Both dots do display a slight asymmetry in the peaks by having a slight tail on one side, although the right dot displays this much clearer. This is likely due to the fact that the peaks on the right side are much sharper, even in normal state. The peaks in the normal state on the left dot only get "fatter". Along with the higher magnitude of the conductance in the left dot this reaffirms the belief that the left dot is more strongly coupled.

Another difference is the non-zero conductance in the normal state on the left side. This

points towards additional transport processes occurring such as co-tunnelling.

Looking at the bias spectroscopy in Fig. 6.2c and d the difference between the dots becomes even clearer. Many of the differences seen in the one dimensional plots can also be seen here. The right dot has sharp peaks which extend over the whole V_{SD} range while in the left dot the Andreev bound states are fairly smooth indicating a stronger coupling to the superconducting electrode.

Most of these contrasts are due to the different way the dots are coupled to the metal electrodes. This can be confirmed by analysing the strength of the couplings Γ. Using the gate factors of the dots obtained from Fig. 6.1 and the fitting method, the total coupling strengths of the dots, where $\Gamma = \Gamma_{Li} + \Gamma_{Ri}$ with $i = N, S$, are obtained and shown in Table 6.2.

Peak number	Left dot (μeV)	Right dot (μeV)
1	1150	247
2	997	214
3	715	220
4	785	222

Table 6.2: *The coupling strengths of the marked peaks in Fig. 6.2. The peak number refers to which marked peak was measured, e.g. peak number 1 refers to* $L1$ *in the case of the left dot or* $R1$ *for the right dot.*

The total coupling strengths show that indeed the left dot is more strongly coupled than the right dot as was implied by the observations. The strength of Γ also obeys the $\Delta E > \Gamma$ requirement to minimise entanglement loss in the dots. The fitting program also returns the strength of Γ_N and Γ_S of both dots which are displayed in Table 6.3.

Peak number	$\Gamma_{LN}(\mu eV)$	$\Gamma_{LS}(\mu eV)$	$\Gamma_{RN}(\mu eV)$	$\Gamma_{RS}(\mu eV)$
1	387	762	209	37
2	259	737	170	44
3	223	491	149	71
4	393	393	132	91

Table 6.3: *A breakdown of the supposed coupling strength of each dot with its electrodes. N refers to the dot coupling with the normal metal electrode. S refers to the coupling with the superconducting metal electrode. The peak number shows which peak marked in Fig. 6.2 is analysed. Peak 4 on the left dot shows equal coupling strengths. This occurs when the fitted Coulomb peak is 1* $\frac{e^2}{h}$ *or larger. The Lorentzian approximation introduced in section 3.3 can only account for this by setting* $\Gamma_N = \Gamma_S$.

Unfortunately when extracting the values it is unclear which is Γ_N or Γ_S. This must be decided by looking at other features. The right dot is fairly clear. The very steep peaks indicate a weak Γ_S coupling. Therefore it is safe to assume that the Γ_N is dominating. The left dot is not as clear, but for now the Γ_S has been assigned as the largest. This will be confirmed later on when tuning the left dot.

In an ideal Cooper pair splitter it is beneficial to keep $\Gamma < \Delta$. Table 6.3 shows that the right

dot is close to Δ but the left dot is significantly above. This can be addressed by tuning the coupling strengths.

After getting a good idea of the status of both dots, it was time to measure the non-local signal. In order to detect a non-local signal, conductance peaks in both dots have to be aligned with the Fermi energy in the superconductor. In this case the peaks marked $L3$ and $R4$ in Fig. 6.2 are aligned by manipulating the plunger gates. Then, in order to entice a current flow through the dots the source voltage is set to -40 µV and 40 µV. This is still well within the energy gap of $\Delta = 120$ µV but large enough to give a strong current through the dot obeying the $eV_{SD} < U_c, \Delta$ requirement for a successful Cooper pair splitter. Measuring at both positive and negative bias will allow for the observation of a non-local current running in both directions. A two dimensional map of the non local conductance or ΔG is created by sweeping the two plunger gates. This two dimensional picture not only gives the magnitude and peak shape of ΔG, but also the position of the signal relative to the conductance peaks of the dot. The results of this first measurement are displayed in Fig. 6.3.

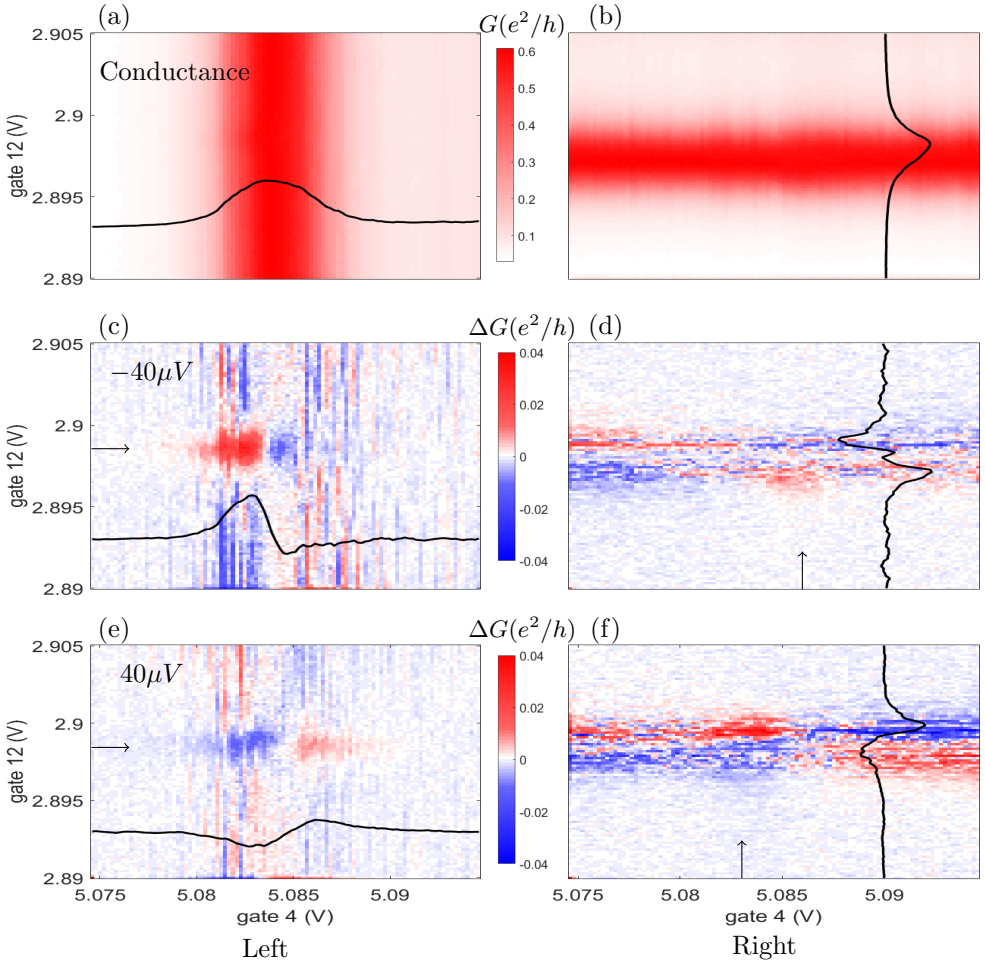

Figure 6.3: *(a) and (b) show the Coulomb peaks of L3 and R4 respectively at* $V_{source} = -40\mu V$ *when the two plunger gates are swept simultaneously. The black line is a trace of the peak at that position. (c) and (d) show the* ΔG *or non-local signal at* $V_{source} = -40\mu V$ *at the peak intersection of the two Coulomb peaks in (a) and (b). The black arrow indicates where the trace was taken. The traces shown are an average of 5 traces around the position of the arrow. (e) and (f) show the the non-local signal at* $V_{source} = 40\mu V$*. The traces on the* ΔG *are all normalised.*

A non-local signal is detected according to Fig. 6.3. Figures (a) and (b) show the Coulomb peaks in the left and right dot respectively. Since the resonances in the let dot are moved by the plunger gate 4, and the right dot by plunger gate 12, the peaks in the left dot appear vertical and in the right dot horizontal. Both the left and right dot show a non-local conductance in both bias configurations (c)-(f). For every point on the local plunger gate axis, a computer algorithm calculates the mean of the conductance in a line parallel to the local conductance peak. It then subtracts the mean from the measured total conductance to detect conductance contributions from the non-local peak, giving ΔG. A result of this method is that the noise shows up in parallel lines, seen clearly in the left dot in Fig. 6.3c and d.
The signal consists in all cases of a positive and negative peak next to each other. The left dot

appears to give much clearer signals with (c) and (d) showing two peaks at the peak intersection area.. There is much less noise than the right dot, where the signals are harder to distinguish. Figure 6.3d and f show the non-local conductance of the right dot. Both plots deal with an artefact of the image generation causing a horizontal divide running through the middle of the image and leaving strong positive and negative signals that switch when they reach the centre. This makes it hard to detect the non-local signals. The ΔG signals are identified by looking for a peak that slightly extends outwards from the noise and is located close to the peak intersection. The noisiness could be attributed to the significantly more strongly coupled left dot being better at letting current through.

All images in Fig. 6.3 are accompanied by traces. An arrow on the plot indicates where the trace was taken. The traces of the non-local conductance in Fig. 6.3c-f are also shown in Fig. 6.4. The positions of the plots are analogous to the position in Fig. 6.3. The traces shown in black are averaged over 5 traces shown in light gray. There appears to be a slight offset of the main trace most clearly seen in Fig. 6.4a. The reason is likely that the main traces are not a direct average from the gray traces, but taken from a 2D plot that automatically averages the 5 nearby traces. The algorithm might have inadvertently induced a slight offset. The magnitudes of the peaks do seem correct however along with the width of the signal.

The most notable effect of the bias is that it switches the positive and negative peaks around, seen clearly when observing the traces in Fig. 6.4, and occurs in both the left and right dot. This is not a surprising result, as switching the bias will naturally switch the direction of the current as well. Lastly the magnitude of the non-local signal is not equal when the bias is switched. It is not unreasonable to expect this as the bias is the same absolute value, however this is likely due to the fact that the quantum dot conductance is not perfectly symmetric.

A similar result was found in schindele et al. in 2014. [42] The group measured the non-local conductance of a Cooper pair splitter device and observed a positive-negative peak pattern identical to the ones observed in Fig 6.3. The switch between negative and positive peaks occurred when the ground state of the superconductor changed from a doublet to a singlet and vice versa. Using this for the plots in Fig. 6.3c-f the occupation of the ground states can be determined. For both negative and positive bias, the ground state starts as a singlet and transitions to a doublet as the plunger gate is increased. Looking back at the bias spectroscopy of the left dot in Fig. 6.2c this is reinforced by the shape of the ABS states, with the $L3$ peak separating a large and a small ellipse. The odd occupation generally has smaller amplitude. They also observed a sign chance of the peaks when the bias was reversed, analogous to the results observed here. To describe this phenomenon they used a rate equation model, on which more information can be found in [42]. The paper only limited itself to the measurement of non-local conductance through one dot. Here a simultaneous measurement on both dots can confirm that they both dots display this behaviour.

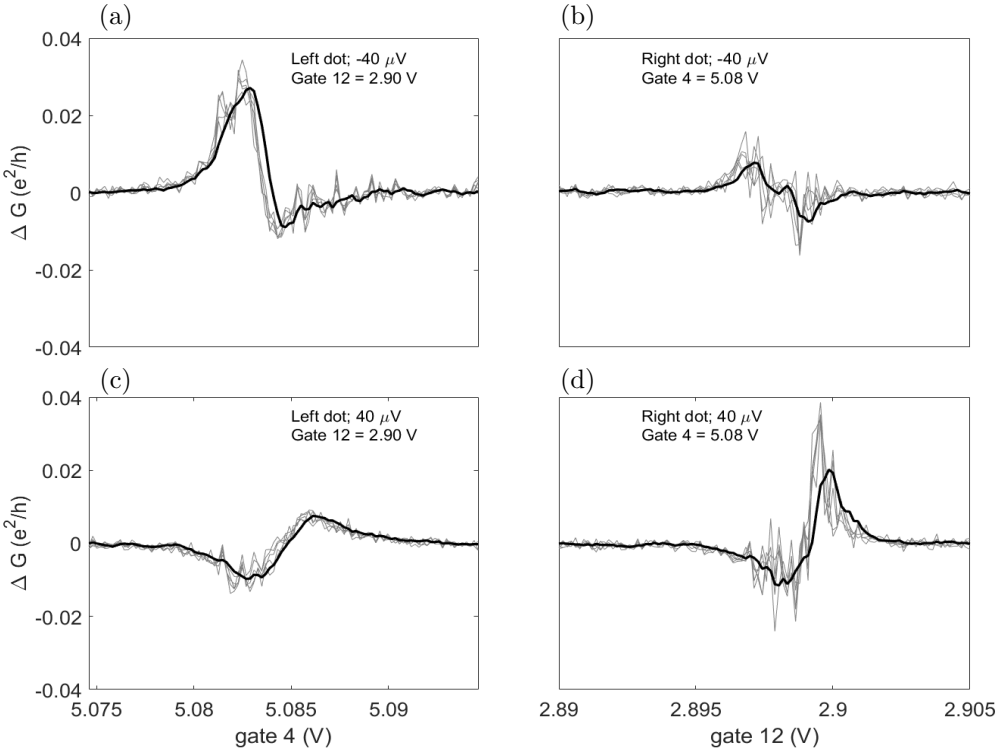

Figure 6.4: *The averaged traces from Fig. 6.3 are shown in black. The grey lines are the measured traces from which the average trace was taken. The position of the plots is analogous to Fig. 6.3. The value of the plunger gate from the other dot is noted on the plot along with the value of* V_{SD}.

Before moving on to measure the non-local signal on more peak intersections, it is vital to test the obtained signal and ensure it is not an artefact. The signal was therefore measured with an increasing magnetic field. A high enough magnetic field will destroy the superconductivity of the aluminium contact and revert to the system back to the normal state. In Fig. 6.5 the non-local signal of $L4$ and $R4$ is shown with an increasing strength of the magnetic field. The signal disappears at around $B = 80$ mT showing that ΔG is indeed due to S-state related transport such as the transport of Cooper pairs. The $L4 - R4$ intersection was chosen as it had one of the clearest signals. This test was performed on several other peaks and the non-local signal disappeared at around 80 mT for all investigated intersections.

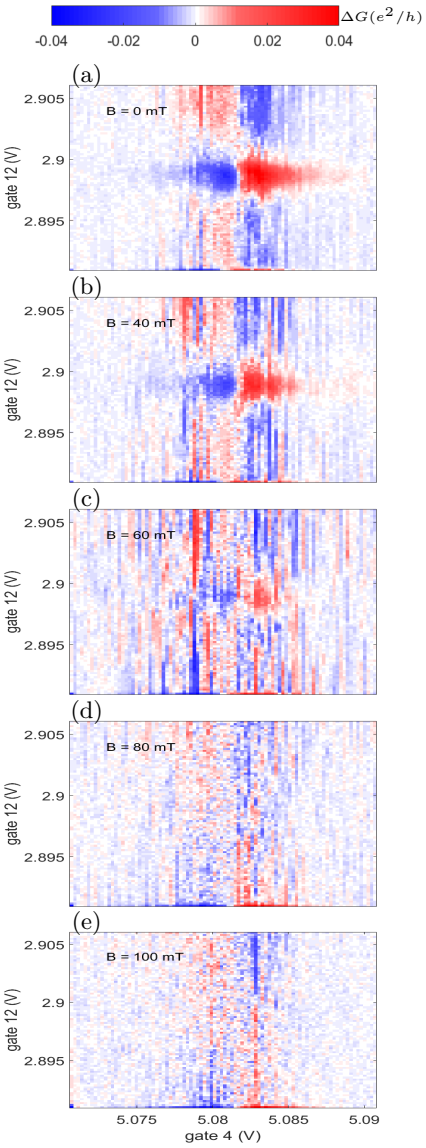

Figure 6.5: *The non-local signal of the $L4 - R4$ intersection with increasing magnetic field. The signal degrades slowly until it can vaguely be seen at 60 mT (c). At 80 mT (d) it has completely disappeared, confirming that the observed ΔG peaks arise from the superconducting effects.*

Now that the signal appears real, the rest of the peaks marked in Fig. 6.2 are ready to be investigated. The non-local signal ΔG was measured in the same way as in Fig. 6.3, meaning the signal in the right and left dot was measured at both a $V_{SD} = -40$ µV and $V_{SD} = 40V$ µV. This was done for every peak intersection. The resulting sixty four plots are laid out in Figs. 6.6 to 6.9. The figures had to be displayed sideways to ensure the individual plots were visible.

Figure 6.6 shows the non-local conductance observed in the left dot at $V_{SD} = -40$ µV for all peak intersections. The plot with the highlighted border is the same as Fig. 6.3c. The signal

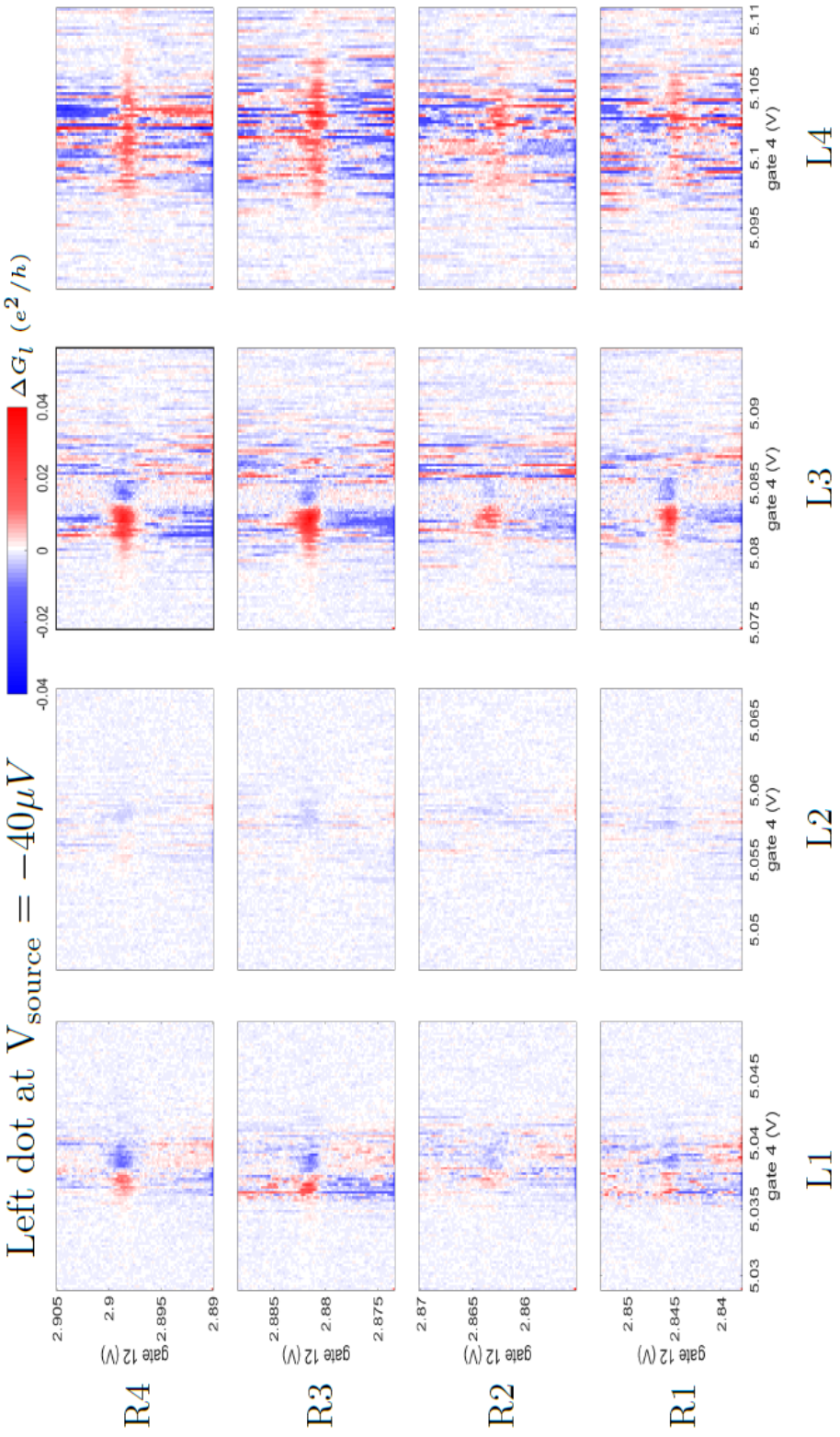

Figure 6.6: *An overview of the non-local signals found for each peak intersection at* -40 μV *source bias in the left dot. The peak is displayed at the outer axis where the peaks from the left dot refer to the entire column and the peaks from the right dot refer to the entire row. Each two dimensional image shows* ΔG *at the specific peak intersection. The plot with the highlighted border is the* $L3 - R4$ *peak measured in Fig. 6.3c.*

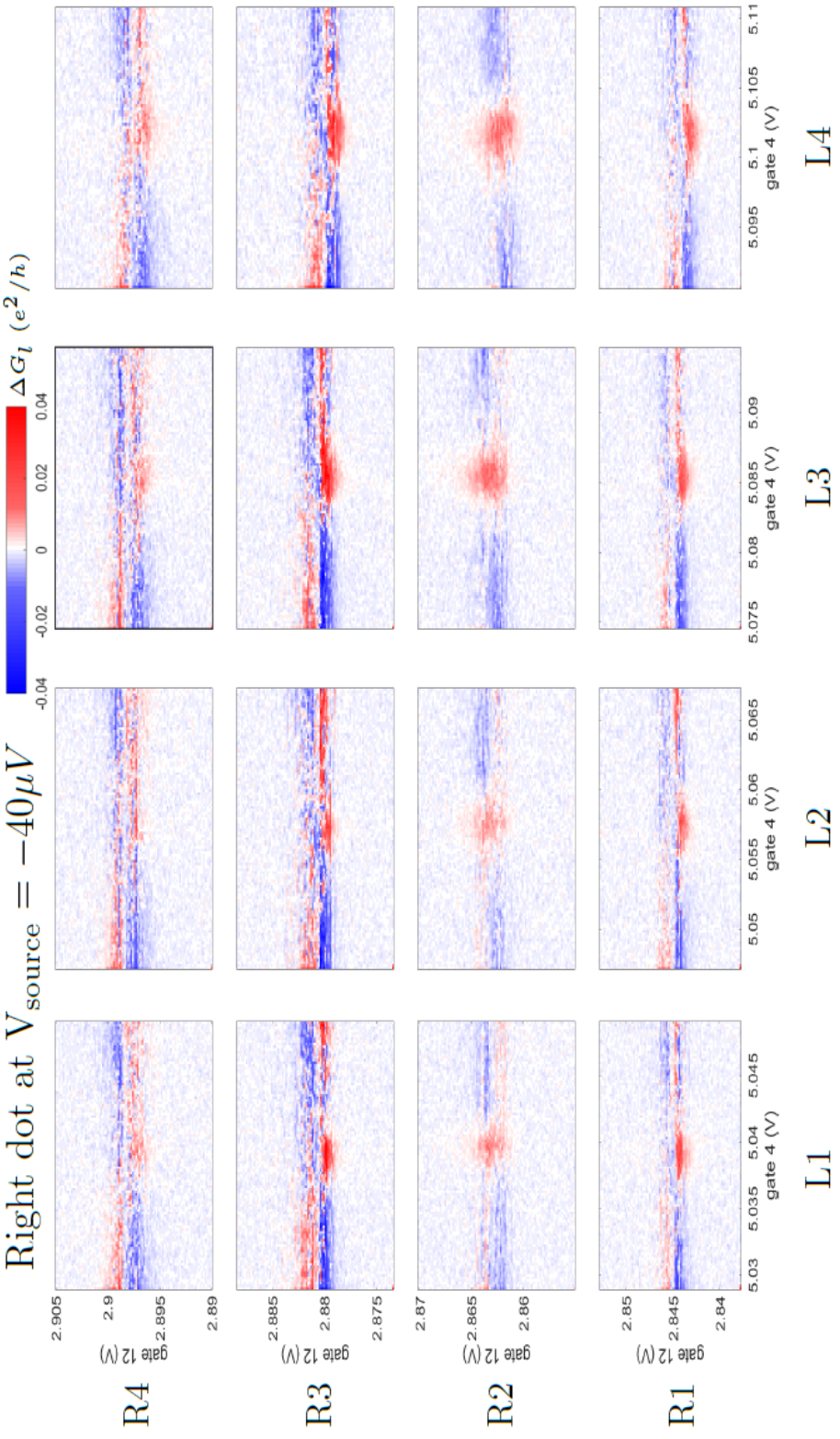

Figure 6.7: *An overview of the non-local signals found for each peak intersection at $-40V$ μV source bias in the right dot. The peak is displayed at the outer axis where the peaks from the left dot refer to the entire column and the peaks from the right dot refer to the entire row. Each two dimensional image shows ΔG at the specific peak intersection. The plot with the highlighted border is the $L3 - R4$ peak measured in Fig. 6.3d.*

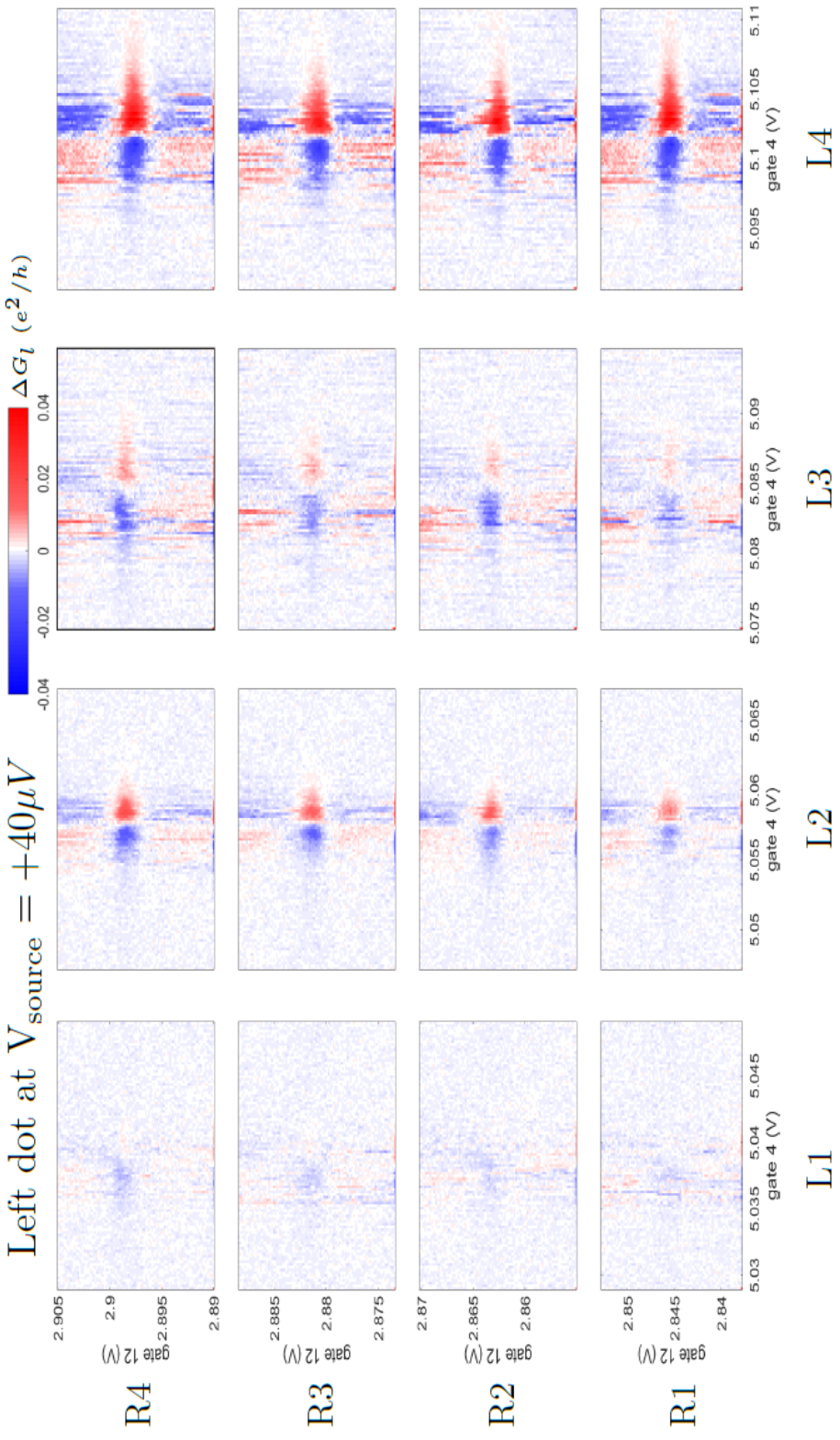

Figure 6.8: *An overview of the non-local signals found for each peak intersection at 40 μV source bias in the left dot. The peak is displayed at the outer axis where the peaks from the left dot refer to the entire column and the peaks from the right dot refer to the entire row. Each two dimensional image shows ΔG at the specific peak intersection. The plot with the highlighted border is the L3 – R4 peak measured in Fig. 6.3e.*

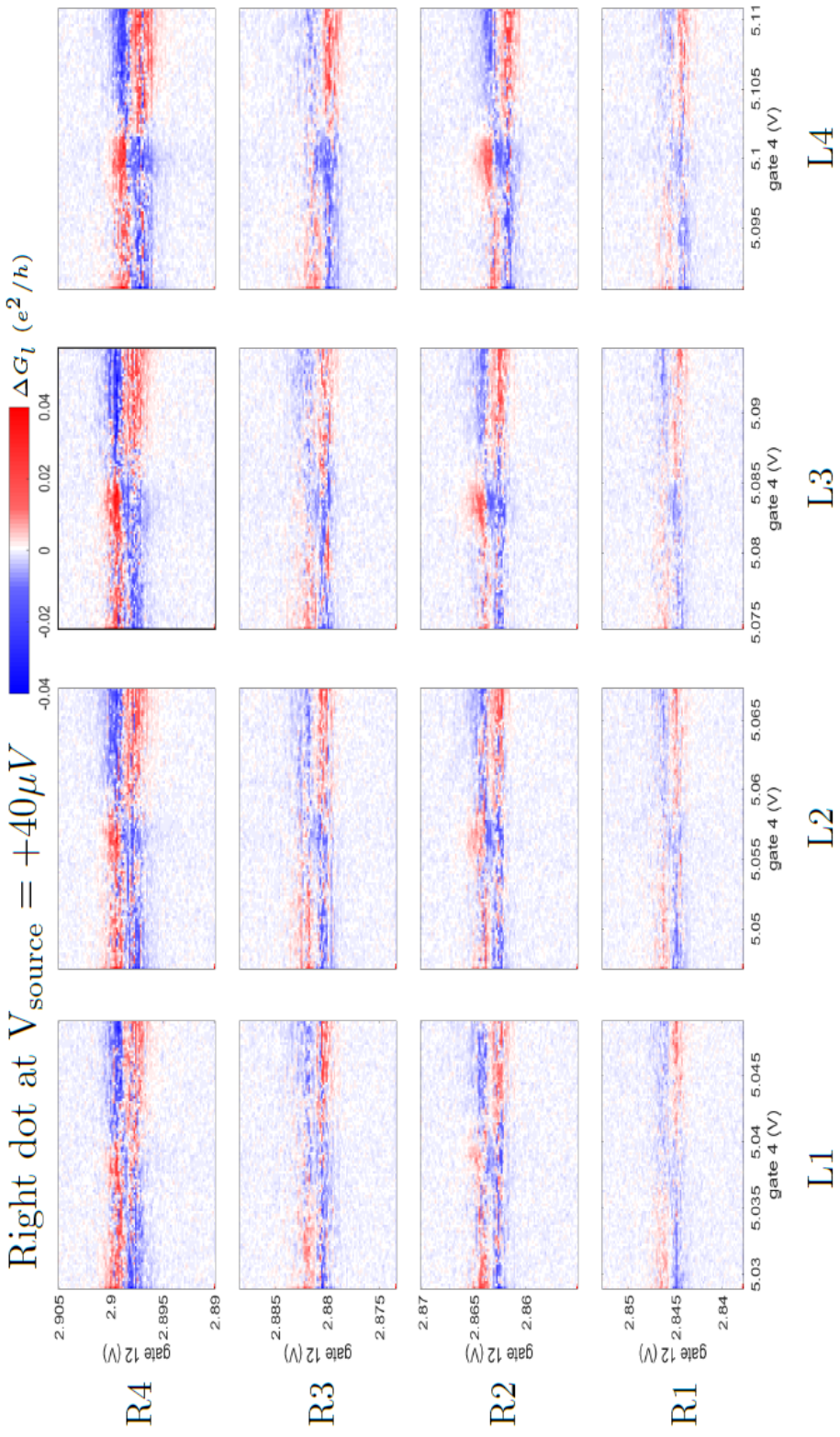

Figure 6.9: *An overview of the non-local signals found for each peak intersection at 40 μV source bias in the right dot. The peak is displayed at the outer axis where the peaks from the left dot refer to the entire column and the peaks from the right dot refer to the entire row. Each two dimensional image shows ΔG at the specific peak intersection. The plot with the highlighted border is the L3 – R4 peak measured in Fig. 6.3f.*

observed there is seen is the remainder of the plots in the same column, with identical peak patterns. The signal is weaker in the $L1$ column and $L2$ shows no to very weak non-local conductance. Column 4 shows a long positive peak instead, different from the others.

Figure 6.7 shows the right dot at $V_{SD} = -40$ µV. The highlighted plot is identical to Fig. 6.3d. The peaks that were hard to detect in that plot are clearer in the other rows. This confirms that the signal observed in Fig. 6.3d was due to non-local conductance. All plots have peaks with similar intensity except for the top row, whose signals are not that obvious. The $R2$ row has similar behaviour to the $L4$ column in Fig. 6.6, showing only a positive peak.

The left dot at positive voltage in Fig. 6.8 shows strong signals, especially in the $L4$ column. As the highlighted plot from Fig. 6.3e suggested, the peaks have changed sign. The $L4$ column now does not show a single peak any more but instead displays the positive-negative peak combination observed in all the other signals.

In contrast the signals in the right dot at $V_{SD} = 40$ µV in Fig. 6.9 shows weak signals. Only the $R4$ and $R2$ rows display observable peaks. Similar to the $L4$ signals in the left dot, at positive voltage the $R2$ row now displays positive and negative peaks as opposed to the single positive peak at $V_{SD} = -40$ µV. Overall the right dot is plagued by noise a lot more, making the signals hard to observe.

The non-local signal is in Figs 6.6 to 6.9 are very dependant on the local conduction peak, meaning in the left dot, ΔG depends strongly on the resonances in the left dot. It appears the non-local conductance is only weakly dependent on the non-local resonances.

To get a better idea of the non-local signals, the visibility, $\eta = \frac{\Delta G}{G}$, is measured for every plot from Figs. 6.6 to 6.9. The acquisition software creates a $2D$ plot of the visibility by calculating η at every point in the ΔG plots. The value chosen for the visibility is the maximum value in the area of the peak. A value of 0% means there was no visible η peak or that the peak was not clear and inside the noise range $\sim 2\%$. This is therefore also assigned as the uncertainty on η. The errorbars are not added to Fig. 6.10 as this made the plots to cluttered and unreadable. Most plots contain two peaks, a negative and a positive peak. The visibility was determined for both peaks. The results are reported in Fig. 6.10. The x-axis in these plots are the resonances of the right dot, while the data points are organised by the resonances of the left dot. This means that for example the data point of the $L1$ peak at $R = 1$ reflects the visibility of the $L1 - R1$ intersection. Each intersection has two points, one for the positive peak and one for the negative peak which is reflected by the positive and negative visibility values in the graph.

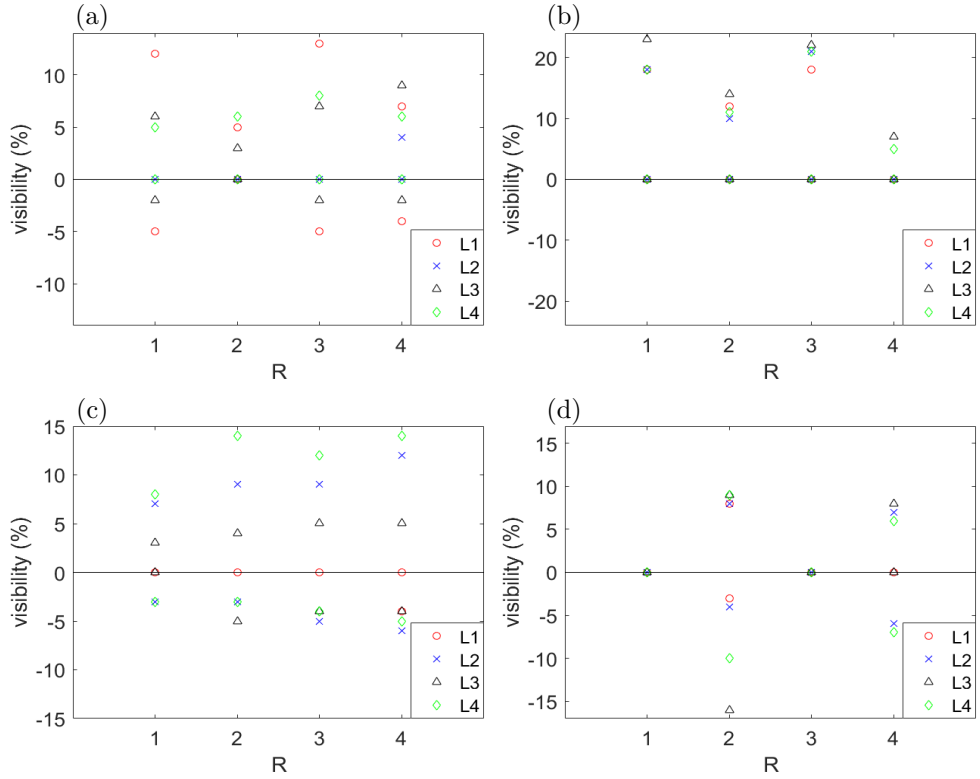

Figure 6.10: *The visibility of the non-local signals detected in Figs. 6.6 to 6.9. (a) and (b) show results of the ΔG signals measured at $V_{SD} = -40\mu V$ on the left and right dot respectively. The plots contain the visibilities of both the positive and negative signals detected. (c) and (d) present the findings of the left (c) and right (d) dots at $V_{SD} = 40\mu V$. The x-axis shows the peak number of the right dot. As such, A value of $L1$ on the $R1$ axis represents the visibility of the $L1 - R1$ peak intersection. The visibility has an error of 2% but the errorbars are not added on the plots as this made them to cluttered and unreadable.*

The visibilities of the non-local conductance in Fig. 6.10 show very varied results between the different dots. The visibilities in the right dot (Fig. 6.10b and d) show a strong dependence on the resonances in the right dot, in accordance with the observations made in Figs. 6.6 to 6.9. At negative bias in Fig. 6.10b, the $R1$ and $R3$ peaks have a consistent stronger η then $R2$ and $R4$, whereas at positive bias in Fig. 6.10d this is reversed in the extreme sense, with $R1$ and $R3$ showing no visibilities. The right dot is also responsible for the highest observed visibility, in both the positive peaks and negative peaks. This is likely due to it being in a more optimal splitting regime than the left dot as observed in the bias and conductance measurements in Fig. 6.2. However it is rather surprising that there is no negative ΔG Fig. 6.10b at all even though the negative peaks in Fig. 6.6 were not all that strong. In agreement with previous observations there is also no strong dependence on the resonances of the left dot, with the data points in Fig. 6.10b and d being fairly close to each other.
The left dot (Fig. 6.10a and c) shows the visibilities being strongly dependent on the resonances of the left, with the data points spread out. It also shows a weak non-local dependence as in the right dot with the magnitudes of the resonances varying only slightly. In addition, the left dot has more total observed visibilities but they occur in a smaller range. Similar to the

right dot, the negative signal are less clear with a maximum of $-7 \pm 2\%$ to a maximum of $16 \pm 2\%$.

To get a clearer picture the magnitude of the visibility is mapped out in Fig. 6.11.

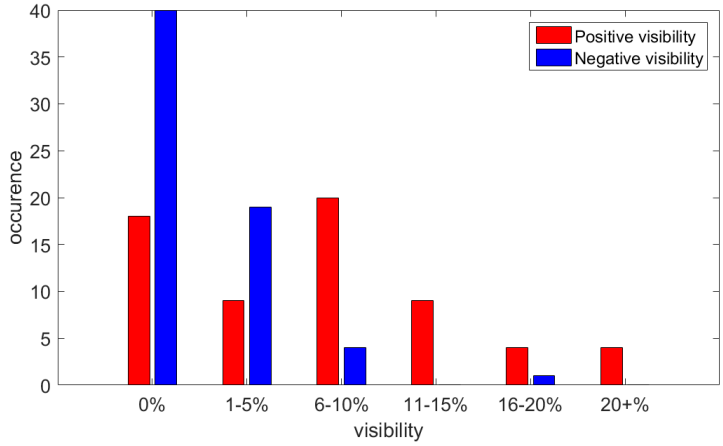

Figure 6.11: *The visibility of the peaks has been organised and categorised into groups. The figure shows the number of times the value of the visibility has fallen into one of the categories. It illustrates the disparity between the positive and negative signals, with the negative signal being far less successful. It also shows the large number of peaks which showed zero visibility. The highest observed visibility was 23 %.*

Fig. 6.11 shows clearly the weak negative signal, with 40 of the 64 total negative peaks resulting in a visibility of 0%. The positive signals have a wider spread, with the $6 - 10\%$ category having the highest occurrences.

6.2 Tuning of the non-local signal

With the detection of a non-local signal it is time to tune the coupling of the dots. The device has 15 bottom gates but initially only gate $2, 6, 11$ and 14 are used to tune. Gate 2 (g2) controls the coupling between the left dot and the normal electrode, Γ_{NL}. The tuning of this gate is showcased first, with a description of the method of tuning. The other gates are not shown, but were tuned in the same way. Gate 14 (g14) controls the normal electrode coupling on the right dot Γ_{NR} while gate 6 (g6) and gate 11 (g11) control the coupling to the superconducting electrode Γ_{SL} and Γ_{SR} respectively. Gate 10 is in a better position to tune Γ_{SR} however it was found to be unstable and very slow so instead gate 11 was used.

The coupling is tuned by applying a voltage on the tuning gate. In the case of gate 2, it's voltage was changed from 0 V to -0.55 V with steps at -0.3 V and -0.45 V. When adjusting the voltage on the coupling gate however it also slightly shifts the quantum dot resonances due to the proximity to the dot. Therefore it is necessary to adjust the plunger gate, in this case gate 4, to follow the resonances. This is illustrated in Fig. 6.12, where the peaks can be seen moving diagonally as gate 2 is lowered. When gate 2 is tuned the peaks in the dot are tracked.

This is the blue line in Fig. 6.12 which follows between $L1$ and $L2$. This is necessary to find the gate 4 value needed to image the same peaks as before. It is important to image the same peaks as the differences in the electrostatic potential in the dots can be observed in 1D conduction and bias spectroscopy plots such as in Fig. 6.2. The peak shape of the Andreev bound states observable in these type of plots indicate the coupling regime. When the dot switches regime, e.g from $\Gamma_N > \Gamma_S$ to $\Gamma_S > \Gamma_N$, it will be visible in these images. Figure 6.12 also shows when a peak gets less intense or narrows, already giving clues as to the changing shape of the ABS states.

After the tuning of all the gates the values needed to bring the device to any configuration are known. This was used to measure the non-local signal in several different regimes. The goal is to confirm whether the efficiency of the non-local conductance in tunable and, if so, is the highest in the ideal regime and if there is any significant transport in other regimes.

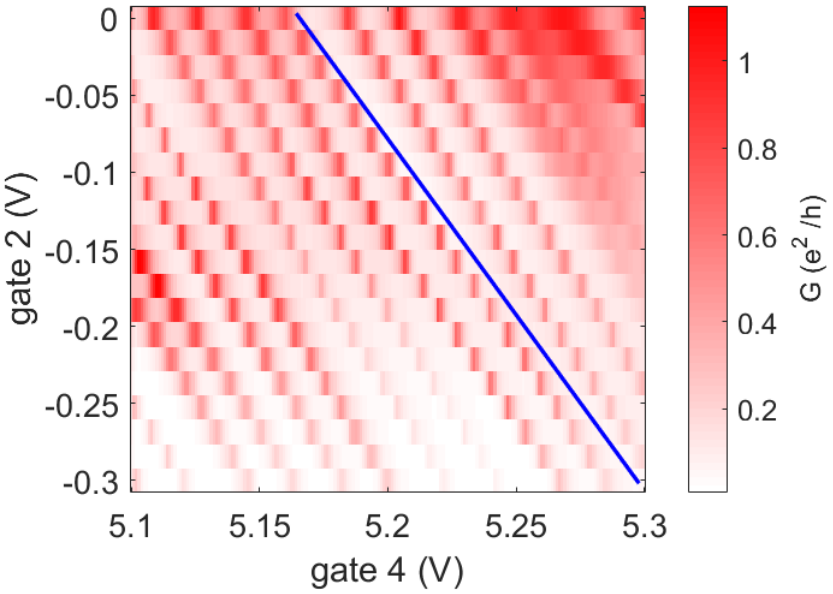

Figure 6.12: *A tuning overview of the tuning of gate 2 from* 0 *V to* -0.3 *V. When varying the voltage on gate 2, due to its proximity to the dot, it also slightly affects the resonances, shifting them similar to the plunger gate 4. Therefore it is important to track the peaks, shown here with a blue line, to ensure that the same peaks can be imaged after the tuning is finished.*

First the tuning of gate 2 is showcased. Gate 2 was varied from 0 V to -0.55 V with steps at -0.3 V and -0.45 V. At each point the conductance was measured and a bias spectroscopy of the left dot was taken. These are laid out in Fig. 6.13. Additionally these measurements were taken in the normal state with a magnetic field of $B = 0.14$ T to measure the coupling strengths, shown in Fig. 6.14.

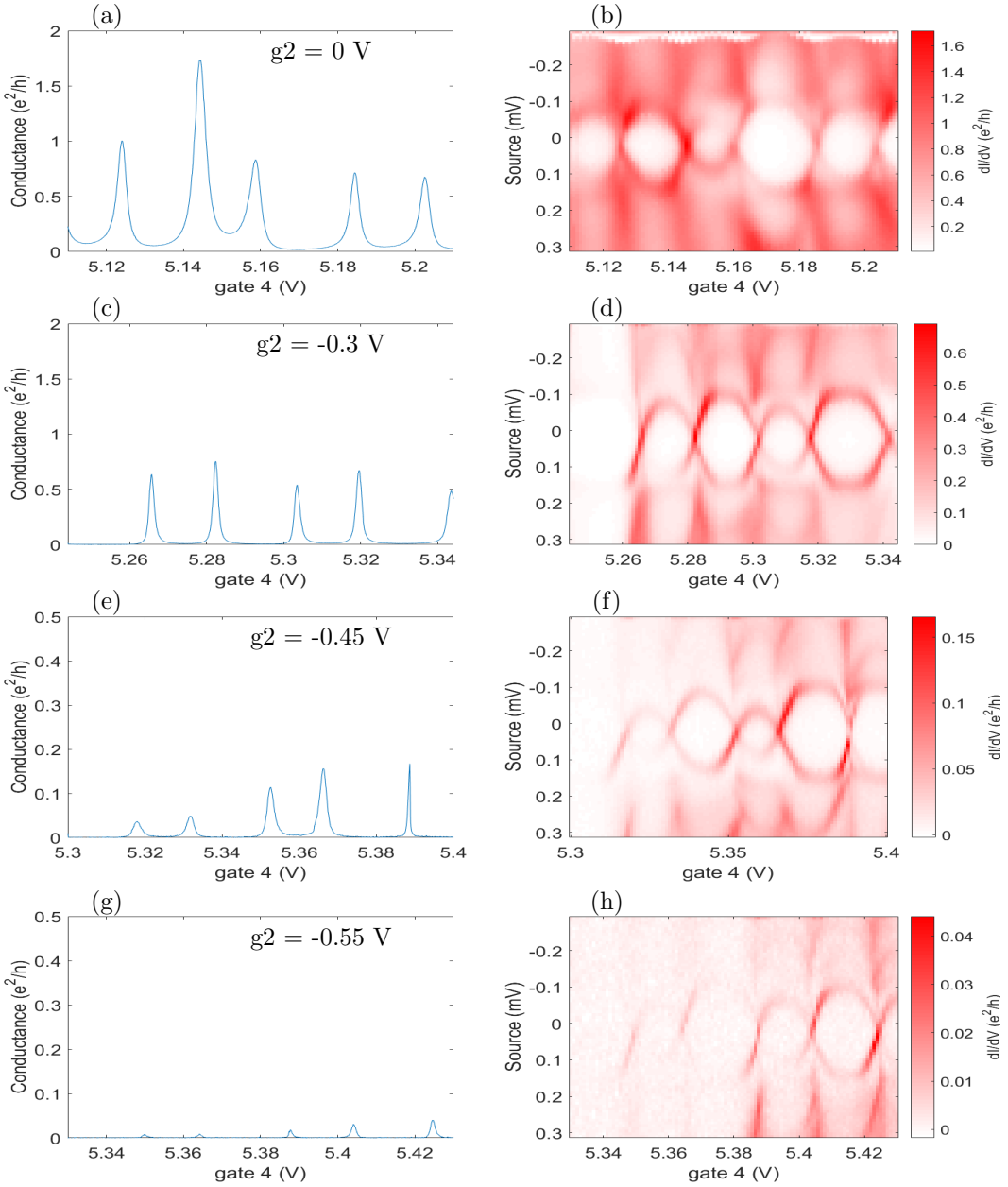

Figure 6.13: *The conductance (a),(c),(e),(g) and the corresponding bias spectroscopy (b),(d),(f),(h) of the left dot in the superconducting state as a result of the tuning of gate 2 (g2) from* 0 *V to* -0.55 *V. The value of gate 2 is stated on the conductance plots but also applies to the bias spectroscopy plots to the left. The conductance through the dot decreases rapidly until the dot is practically pinched off at* $g2 = -0.55$ *V (g). Clear Andreev bound states start showing up in the spectroscopy plot at* $g2 = -0.3$ *V, a sign that the* Γ_S *coupling is strong (g).*

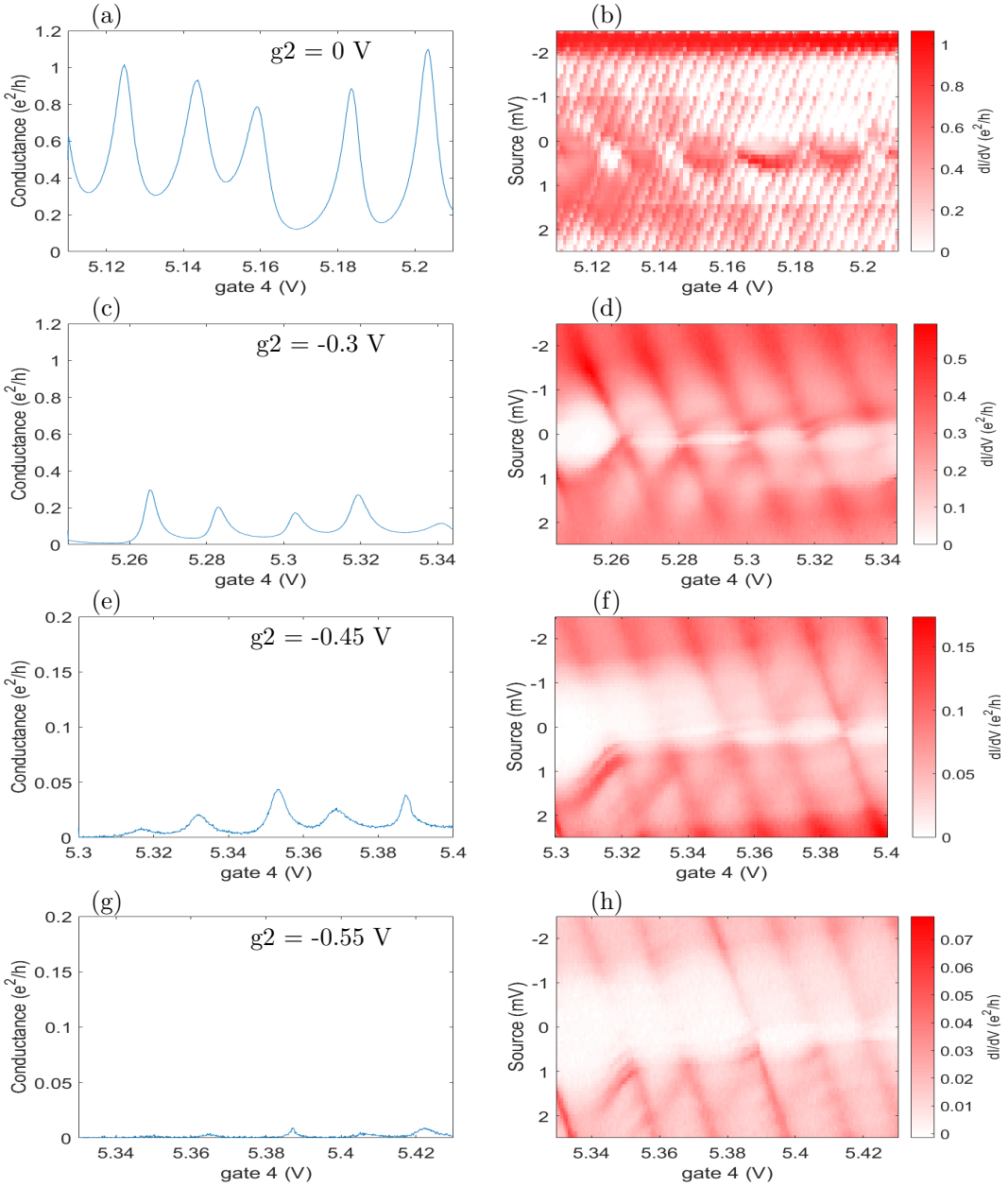

Figure 6.14: *The conductance (a),(c),(e),(g) and the corresponding bias spectroscopy (b),(d),(f),(h) of the left dot in the normal state as a result of the tuning of gate 2 (g2) from* $0V$ *to* -0.55 *V. The value of gate 2 is stated on the conductance plots but also applies to the bias spectroscopy plots to the left. The conductance through the dot decreases rapidly similar to observed in the superconducting state. A strange artefact occurred at the bias spectroscopy at* $g2 = 0$ *V (b), which was found to be due to a low time constant of the bias lock-in.*

Figure 6.13 shows clearly that Γ_N is being tuned. By increasing the negative voltage on the gate the contact barrier will get larger and Γ_N smaller. The result is that the dot will move to-

wards a $\Gamma_S > \Gamma_N$ regime. This is confirmed by the strong Andreev bound states which can clearly be seen at $g2 = -0.3V$ (Fig. 6.13d) onwards. The increased barrier results in a lower conductance through the dot. Note the adjusted scale on the conductance plots from $g2 = -0.45V$ (Fig. 6.13e and g). At $g2 = -0.55V$ the conductance through the dot is almost negligible showing that the current through the wire has been effectively pinched off. This tuning shows that having gate 2 at $-0.3V$ results in a $\Gamma_S > \Gamma_N$ regime with relatively high conductance through the dot. Naturally, gate 6 can still be adjusted to tweak the regime more or switch back to the opposite regime.

Fig. 6.14 shows the measurements taken in the normal state. The drop in conductance seen in the superconducting state is even more prevalent. Again note the adjusted y-axis on Fig. 6.14e and g. The bias spectroscopy emphasises the low conductivity in the superconducting gap. At $g2 = 0$ V in Fig. 6.14b an artefact blurs the measurement. The measurement was performed twice and both times the artefact popped up. It was found to be due to the time constant on the source lock-in and was resolved for future plots.

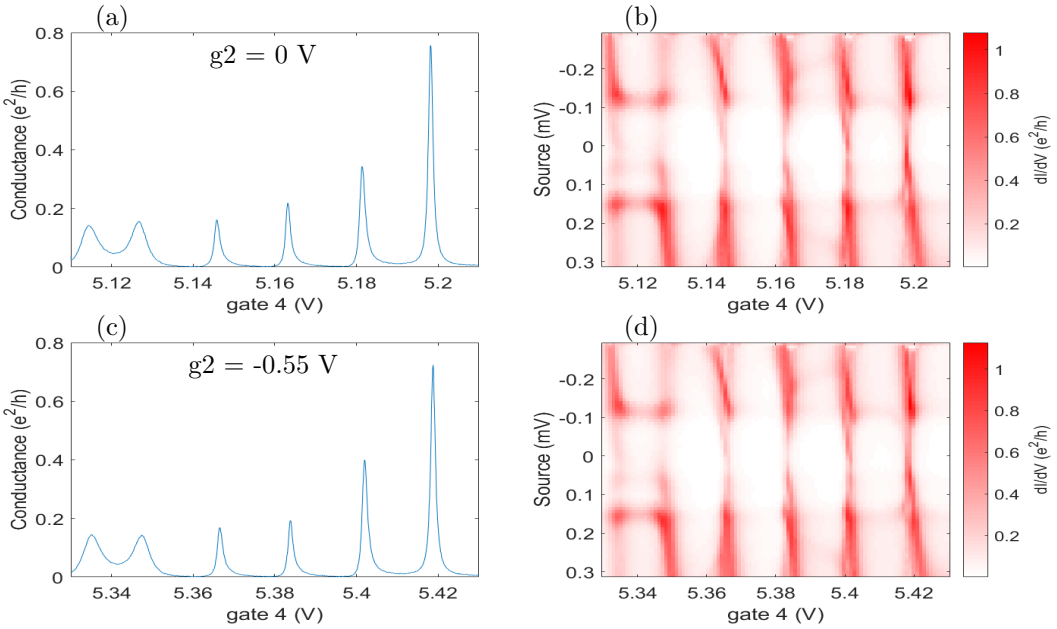

Figure 6.15: *The right dot in the superconducting state before ($g2 = 0V$)(a)-(b) and after ($g2 = -0.55V$)(c)-(d) tuning. The situation in the dot is completely unchanged after tuning gate 2. This is expected as gate 2 should not have an effect on the electrostatic environment of the right dot since it is positioned relatively far away.*

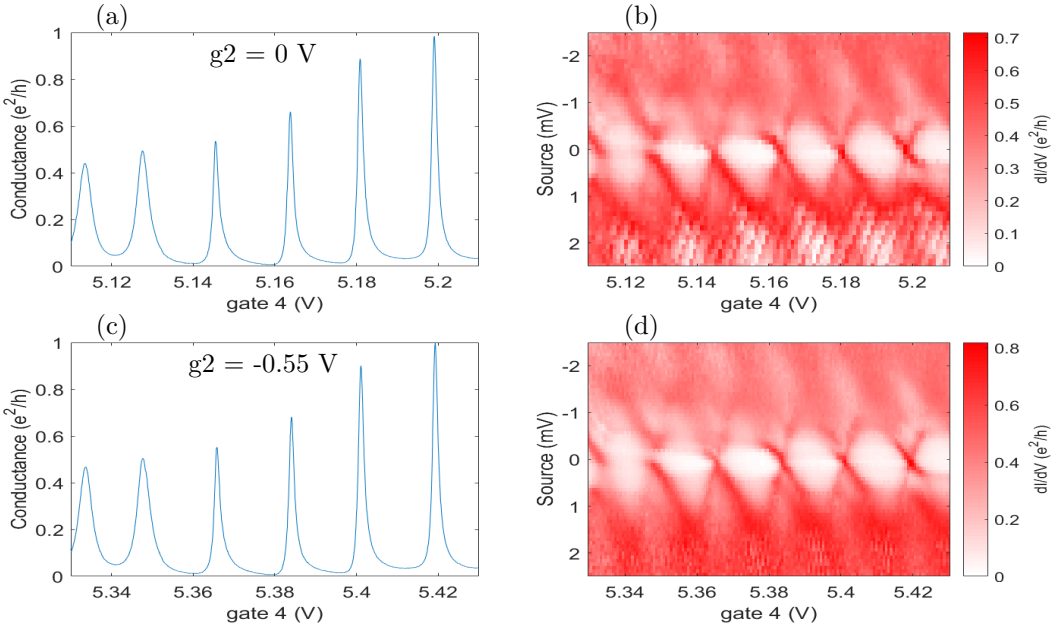

Figure 6.16: *The right dot in the normal state before ($g2 = 0V$)(a)-(b) and after ($g2 = -0.55V$)(c)-(d) tuning. As in the superconducting state in Fig. 6.15 the situation in the dot is completely unchanged after tuning gate 2. The artefact observed in Fig. 6.14b has returned in (b).*

Simultaneously the right dot was also measured. Figures. 6.15 and 6.16 present the measurements at $g2 = 0$ V and $g2 = -0.55$ V. They show that the situation in the right dot has not been affected at all by the tuning in the left dot, showing that independent control of the quantum dots is possible on this device. At $g2 = -0.55$ V in Fig. 6.13g the left dot has been almost completely pinched off. As a result the Cooper pair splitting would stop, causing a drop in the total conductance through the right dot. However the measured ΔG at $g2 = 0$ V in Fig. 6.13 was of the order of $(0.04\ \frac{e^2}{h})$ compared to $\frac{e^2}{h}$ of the G peaks. Detecting a drop in conductance would require a specialised measurement as these plots are not precise enough to confirm the nature of the non-local signal.

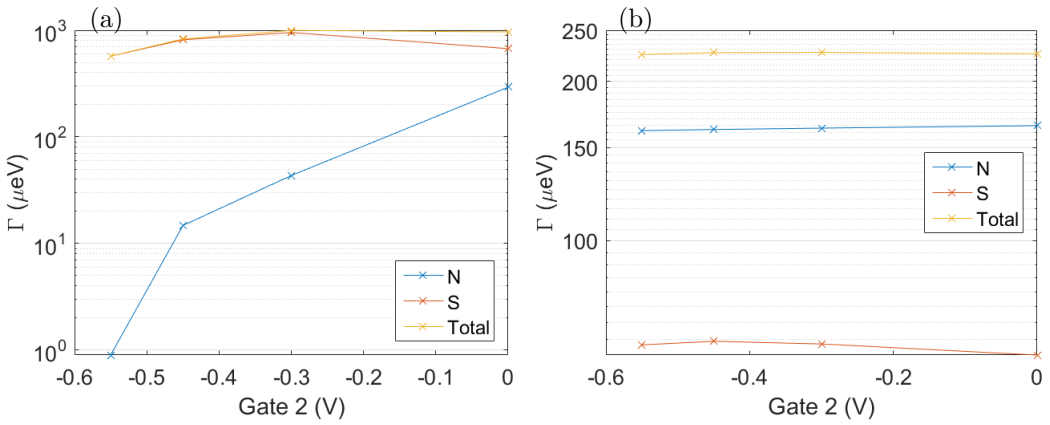

Figure 6.17: *The coupling strengths of the two dots during the tuning of gate 2 from* $0V$ *to* $-0.55V$*. The* Γ *values shown are the mean of the extracted values of the 4 numbered peaks in each dot* $(L1-4, R1-4)$*. (a) shows the evolution of the coupling in the left dot, (b) in the right dot. (a) The decreasing S coupling in the left dot shows signs that the tuning of gate 2 also weakly tuned* Γ_{SL}*, while the increase is likely caused by the negative bias pushing the dot towards the superconducting electrode. (b) The right dot, since it was untouched during this tuning, has remained stable. This is a good sign as it shows that gate 2 has no effect on the electrostatic environment in the right as was intended.*

The peaks traced in the normal state were used in the analysis of the coupling strengths shown in Fig. 6.17. The coupling strengths in the tuned left dot are shown in Fig. 6.17a. One coupling decreases exponentially as the voltage on the gate is made more negative, as is expected. This has to be Γ_{LN} as gate 2 is close to the normal electrode. Γ_{LN} being extremely low at $g2 = -0.55$ V explains why the total conductance through the dot was almost zero in Fig. 6.13g. Γ_{LS} however, would be expected to stay approximately level, as it is not being tuned. Instead it slightly increases and decreases again. An increase is not unusual, as a large negative bias on gate 2 can push the dot towards the superconducting electrode. A decrease is often caused by Γ_S being affected by some of the potential on gate 2, tuning the coupling slightly as well. The observed trace is likely caused by a combination of these two factors. The right dot in Fig. 6.17b is completely as expected, with the coupling strengths staying constant. With gate 2 very far from the right dot, it it is not affected by any of the tuning effects and remains in the same regime.

Using this tuning, the regime in the left dot, originally assigned in Table 6.2, can be confirmed as it clearly shows that at $g2 = 0$ V the dot is in the $\Gamma_S > \Gamma_N$ regime.

After the tuning of gate 2, the other coupling gates were tuned in a similar fashion. All the gates were tuned until a regime change was detected to allow for easy switching between different device configurations. The non-local signal is measured in 4 different configurations. The goal is to confirm whether the visibility and efficiency of the non-local signal in the ideal configuration is the highest. At each regime a bias spectroscopy of the dots is shown, after which a non-local conductance measurement at both $V_{SD} = -40$ µV and $V_{SD} = 40$ µV is made for the resonance crossing of $L5$ with $R1$. $L5$ was chosen as it turned out to be a more promising peak after mapping out $L5$ to $L8$. Non-local measurements for 3 other peak crossings were also done but are not shown.

The measured configurations encompass the main regimes the dots can be put in. An overview of the coupling in the configurations can be seen in Table 6.4. Firstly, the device was put in a configuration where the superconducting electrodes are more strongly coupled. This regime is optimal for the generation of ABS states and sub-optimal for Cooper pair splitting. Then the right dot was brought to the optimal regime of $\Gamma_N > \Gamma_S$ while the left dot was left untouched. After that the left dot was tuned to the same regime as the right dot to bring the device in the most optimal configuration. Next the configuration was optimised after analysing the non-local signals, to eventually try to achieve a highly efficient device. The fourth configuration kept the same regime in the dots but involved opening up the tuning gates to increase the total conductance through the dots. Unfortunately a forced warm-up due to a cooling system renovation cut the experiment short after configuration 4. An attempt was made to cool the device again however the electrical environment was completely changed, making it impossible to continue with the same peaks.

Configuration number	Regime left dot	Regime right dot
Configuration 1	$\Gamma_S > \Gamma_N$	$\Gamma_S > \Gamma_N$
Configuration 2	$\Gamma_S > \Gamma_N$	$\Gamma_N > \Gamma_S$
Configuration 3	$\Gamma_N > \Gamma_S$	$\Gamma_N > \Gamma_S$
Configuration 4	$\Gamma_N > \Gamma_S$	$\Gamma_N > \Gamma_S$

Table 6.4: *The configurations of the dots during the different measurements.*

Configuration 1

To achieve this configuration the gate values were set as shown in table 6.5.

gate 2	gate 6	gate 11	gate 14
−0.3	−0.3	0.6	−0.6

Table 6.5: *The value of the tuned gates to achieve configuration 1. Values are shown in volts.*

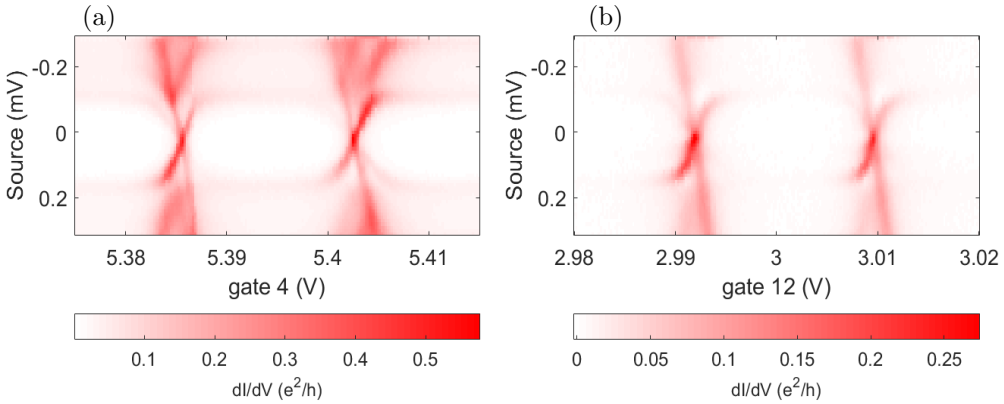

Figure 6.18: *The bias spectroscopy of the left and right dots in the first configuration. Both dots show features of ABS, a sign that the superconducting coupling is strong.*

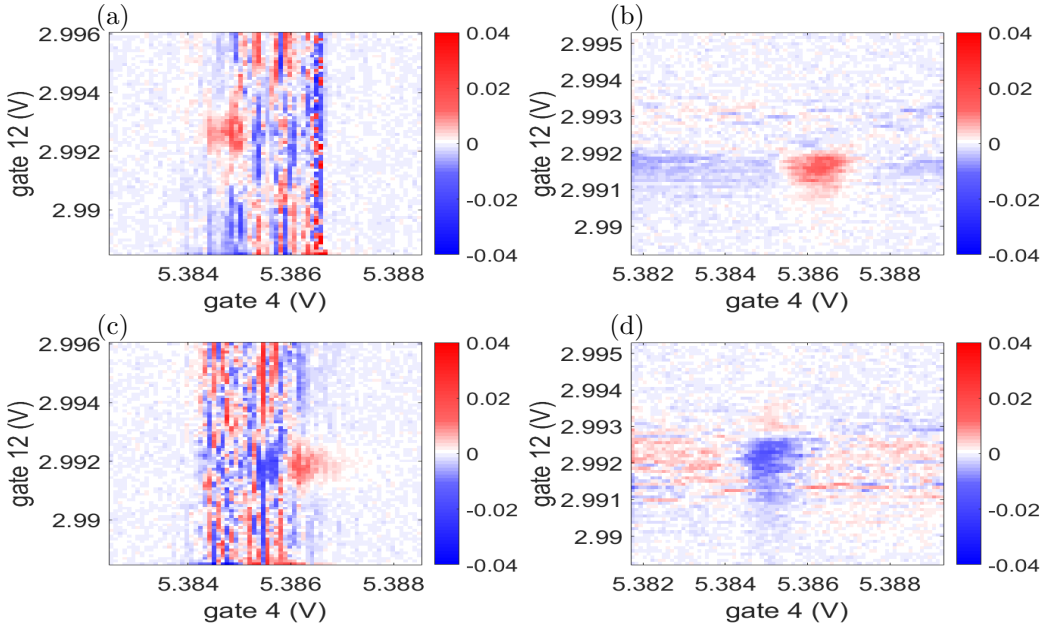

Figure 6.19: *The non-local conductance of the resonance crossing $L5 - R1$ in the first configuration at $V_{SD} = \pm 40\ \mu V$. The shape and magnitude of the signals are comparable to ones detected earlier. Interestingly, the right dot shows a single dominant peak instead of the positive-negative peak combination generally observed during the detection measurements. This is slightly unexpected as the bias spectroscopy shows clear YSR-states indicating ground state transition which cause the positive-negative peaks.*

Fig. 6.18 shows that both dots have ABS states as expected in a strongly S-coupled system. The spectroscopy plots also show that the total conductance in the left dot is higher.

The non-local conductance measurements in Fig. 6.19 show fairly strong ΔG peaks, comparable to the earlier measurements. Despite the system being in a sub-optimal regime, Cooper pair splitting can still occur, so it not unexpected. Especially since both dots are in the same regime and the total conductance through the dots is fairly high. The left dot again shows the positive-negative peaks seen in Figs 6.6 to 6.9. The right dot has more similarities with the $L2$ and $R4$ peak measurements in Figs. 6.6 and 6.7.

Configuration 2

Next the right dot was tuned towards the ideal regime for a CPS. The voltages on the gates are shown in Table 6.6.

gate 2	gate 6	gate 11	gate 14
−0.3	−0.3	0.55	0.15

Table 6.6: *The value of the tuned gates to achieve configuration 2. Values are shown in volts*

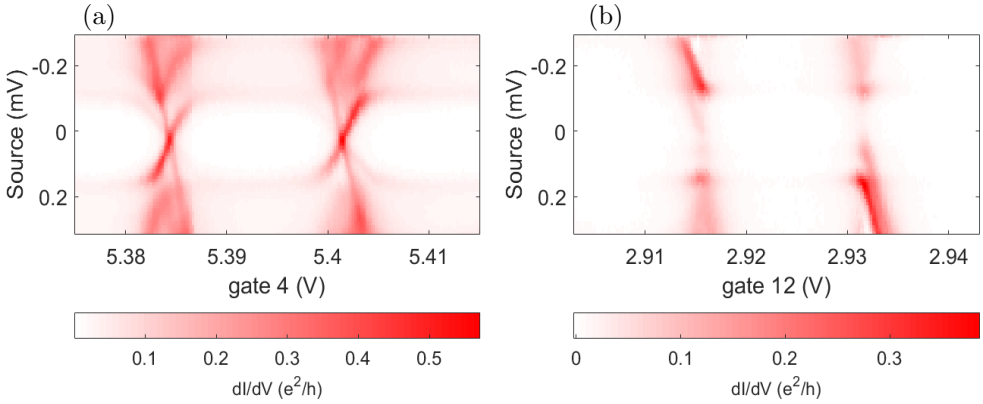

Figure 6.20: *The bias spectroscopy plots of the two dots in configuration 2. The left dot remains unchanged, with the sub-gap states still visible, indicative that the dot has remained in the* $\Gamma_S > \Gamma_N$ *regime. This is expected as tuning gates were unaltered. The right dot has moved to the* $\Gamma_N > \Gamma_S$ *regime as a result of altering the tuning gates. The dot not shows sharp Coulomb peaks, indicative of a low* Γ_S *coupling.*

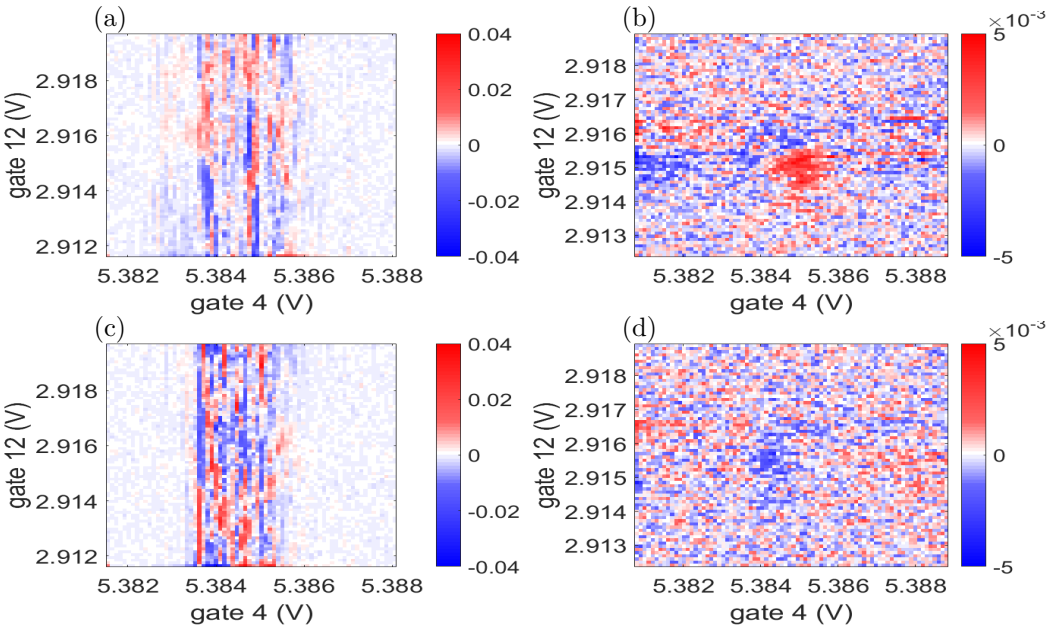

Figure 6.21: *The non-local conductance of the resonance crossing* $L5 - R1$ *in the second configuration at* $V_{SD} = \pm 40\ \mu V$*. The* ΔG *has largely disappeared, the left dot shows no signs of any signal and the right dot only has a very low non-local conductance. The imbalanced configuration does not appear beneficial for Cooper pair splitting.*

Figure 6.20 displays a change in the right dot analogous to its new configuration. The ABS states have become very sharp, a sign of a low Γ_S. The left dot shows an unchanged bias spec-

troscopy as expected. The right dot does appear to have low conduction inside the gap where the non-local signals take place. At $V_{SD} = -40$ µV and $V_{SD} = 40$ µV the conductance seems to be at least 5 times lower than in the left dot.

This configuration appears to be very ineffective as Fig. 6.21 shows very low non-local signals. The scale in the right dot had to be adjusted in order to detect ΔG. The low non-local signal can be due to the uneven configuration in the device, however the dots were also in an uneven regime when the non-local signals were initially detected in Fig. 6.6 to 6.9. The low total conductance in the right dot could be another reason for the significantly lower ΔG signal. Mostly because the left dot, which was left untouched and previously showed good non-local signals, now has very weak ΔG. Likely it is due to a combination of the two.

In these plots there is also a rather high signal to noise ratio. Ideally the measurement would have been repeated several times and averaged, allowing a hidden to possibly appear. Unfortunately with the impending warm-up this was not an option.

Configuration 3

By setting the gates to the values shown in Table 6.7 the left dot was tuned to the same regime as the right dot bringing the device towards the ideal configuration.

gate 2	gate 6	gate 11	gate 14
−0.2	−0.75	0.55	0.15

Table 6.7: *The value of the tuned gates to achieve configuration 3. Values are shown in volts*

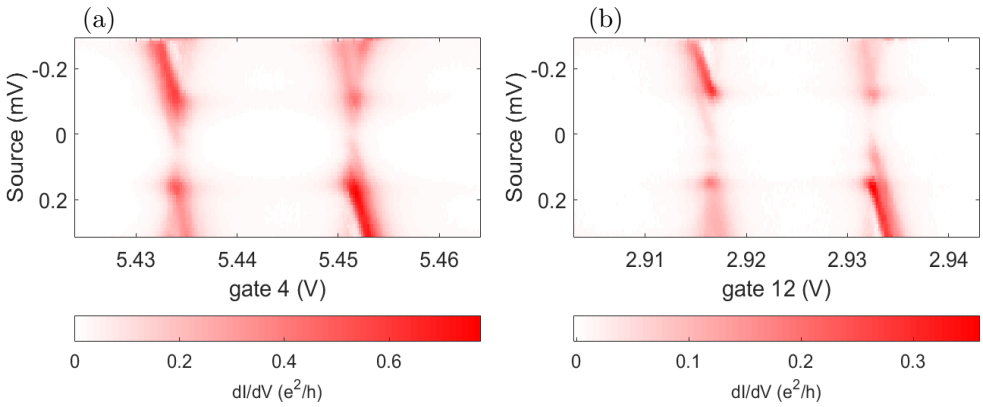

Figure 6.22: *The bias spectroscopy plots of the two dots in configuration 3. The left dot has now moved to the same regime as the right dot, which has been left untouched. The left dot now shows sharp Coulomb peaks as the right dot indicating that both dots are in the same regime.*

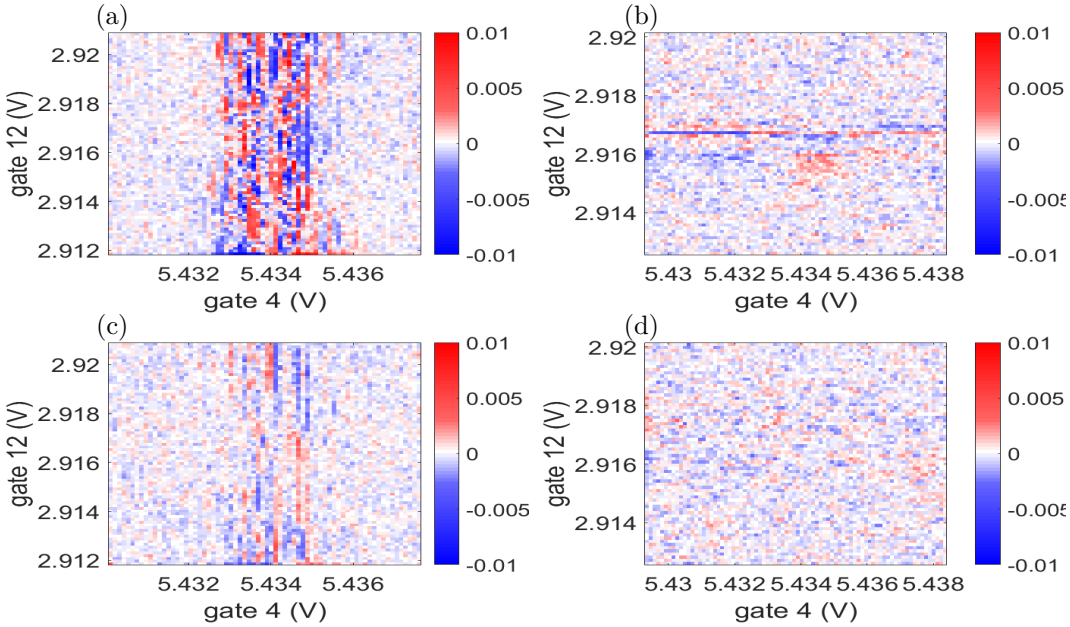

Figure 6.23: *The non-local conductance of the resonance crossing $L5 - R1$ in the third configuration at $V_{SD} = \pm 40\ \mu V$. The non-local signal has completely disappeared. This is unexpected as the device should be in or near the optimal regime. However, the total conductance through the dots is quite low which could cause an undetectably small ΔG signal.*

The bias spectroscopy plots in Fig. 6.22 display the left dot in its new strong N-coupling regime with similar sharp peaks as the right dot. However, as with the unchanged right dot, the total conductance appears to be quite low at $V_{SD} = -40$ µV and $V_{SD} = 40$ µV which may result in weak signals although it is higher than the right dot.

Fig. 6.23 shows the non-local measurements from regime 3. There appears to be no observable signal. This is quite unexpected as the device is in its theoretical ideal configuration. The low total conductance G could be the issue.

Configuration 4

Next the coupling strengths were altered to the gate values in Table 6.8 to tweak the regime so the non-local signal will hopefully be visible.

gate 2	gate 6	gate 11	gate 14
−0.4	−1.15	0.55	−0.15

Table 6.8: *The value of the tuned gates to achieve configuration 4. Values are shown in volts*

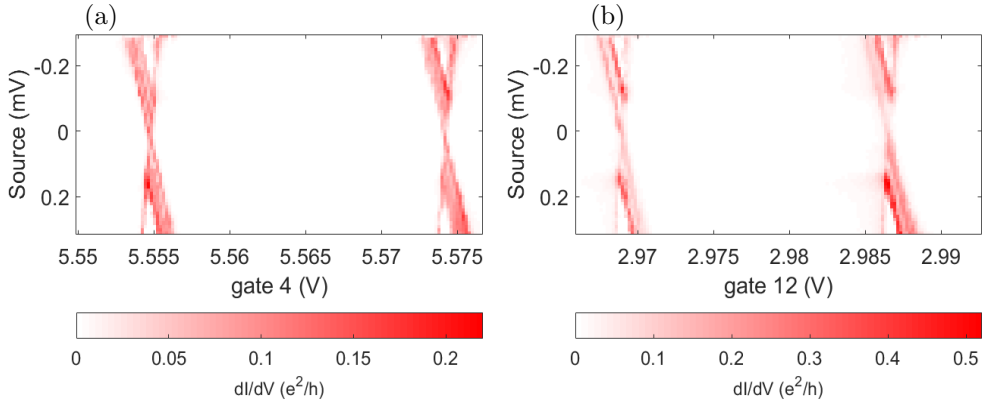

Figure 6.24: *The bias spectroscopy plots of the two dots in configuration 4. The dots are in the same regime as in configuration 3 but the couplings with the electrodes have been opened up allowing a higher conductance through the dots.*

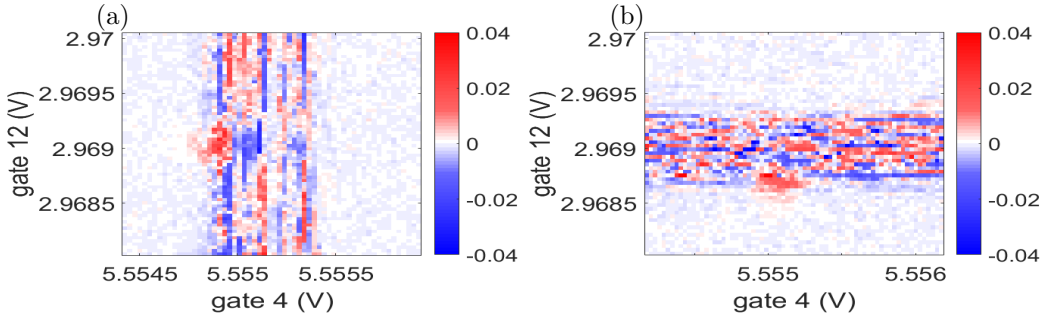

Figure 6.25: *The non-local conductance of the resonance crossing $L5 - R1$ in the fourth configuration at $V_{SD} = -40\mu V$. The non-local signals have returned. The peaks appear very narrow, likely a result of the very sharp Coulomb peaks seen in Fig. 6.24. The left dot also shows the positive-negative peak combo seen so often in the detection measurements.*

Unfortunately when taking this set of measurements time constraints due to a forced warm-up to replace the cooling system resulted in low resolution images and only the non-local signal at negative bias being measured to speed up the data collection.

Figure 6.24 shows both having very sharp peaks indicative of strong $\Gamma_N \gg \Gamma_S$. Conductance between the peaks has also completely disappeared and the total conduction through both dots is also similar as the first regime.

In configuration 4 in Fig. 6.25 the non-local conductance have returned. Both dots show ΔG peaks with a similar intensity as the ones in the first configuration, although the low resolution on the plots makes it hard to conclude if the the peaks are more well defined. The behaviour is also similar, with the left dot showing positive and negative peaks and the right dot only a positive peak. Ideally the non-local signals would have been visibly stronger as this the ideal

configuration for Cooper pair splitting. However measuring the visibility of the non-local signal will show if the final configuration has been more successful. The visibility is shown is Fig. 6.26

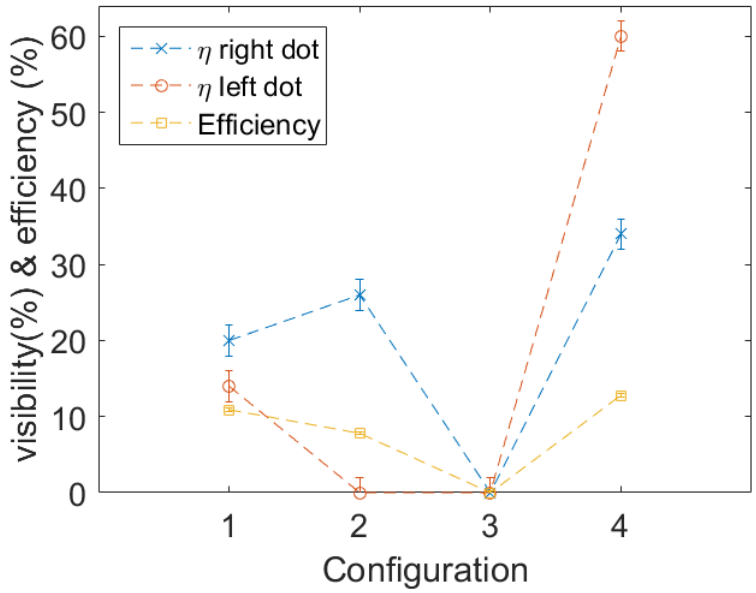

Figure 6.26: *The visibility η and efficiency s of the non-local signals measured for the $L5 - R1$ intersection at $V_{SD} = -40\mu V$. Only the negative source bias is shown as there is no data for the positive bias. The fourth configuration is the most successful with the highest visibilities and efficiency occurring here. A good result as the fourth configuration is the most optimal of the four.*

The visibility strongly increases in the last configuration showing that the non-local signals are indeed stronger as expected. The first configuration has visibilities comparable to the non-local detection measurements in Fig. 6.10. In configuration 2, the visibility of ΔG in the right dot actually increases, even though the signal was very weak. However the left does not give any significant visibility. Configuration 3 shows no visibility. Not surprising as there was no observation of any non-local signals. When the regimes were tweaked to configuration 4, the visibilities jump up to a maximum of $60 \pm 2\%$. Being in the ideal regime this is very promising as 60% is higher than detected in any of the other measurements in this thesis. This shows that the device can be successfully moved to from a low Cooper pair splitting configuration to a high splitting configuration. With more tweaking a complete map could be created, allowing the users to precisely control the flow of entangled pairs.

To calculate the efficiency of the device the same definition as the 2012 paper by Schindele et al. [11] which reported an efficiency of 90 % is used:

$$s = \frac{\Delta G_L + \Delta G_R}{G_L + G_R}$$

Where the subscript L or R refers to the left or the right dot. The maximum value of the G and ΔG peaks are used. The result is also shown on Fig. 6.26. The efficiency follows the

general result of the visibility although not as drastically. configuration 1 gives an efficiency of $10.9 \pm 0.2\%$ compared to the ideal configuration 4, with high visibilities, with $12.8 \pm 0.2\%$.

While the forced warm-up prevented any further investigation it did produce one important point. The device did not return to the state it was before the warm-up, meaning if a similar device is to be used as a reliable source for entangled pairs it has to constantly be held at cryogenic temperatures which might prove difficult.

A non-local conductance was successfully detected in most of the 32 investigated resonance crossings at both neagative and postive source-drain bias. Many showed a positive and negative conductance peak, a result of a transition between the superconductor ground states according to [42]. The visibilities reinforce the strong dependence on the local resonances observed in the initial detection measurements. Also observed is the positive signals having a higher visibility and a better spread than negative ΔG, where 40 of the 64 peaks show no visibility.

The tuning of the non-local signals has been successful. The coupling strengths have demonstratively been varied using the many gates available on the device. This allowed us to measure the non-local conductance in various regimes culminating in a high visibility and the highest efficiency in the ideal configuration. Unfortunately the forced warm-up cut the experiment short. I believe that a higher visibility and efficiency definitely could have been achieved by tweaking the configuration of the device, perhaps even by using the remaining gates, which have remained unused in this thesis but were utilised in following experiments. Despite this, I still believe the main goal of this thesis has been successful as we have detected non-local conductance in a large number of resonance crossings and demonstratively tuned them to more effective configurations.

More data exist that can still be analysed, but due to time constraints was not done for this thesis. There are 3 additional peak crossings measured in all the configuration. Calculating the visibilities and efficiencies of these peak crossings can help underline the observed behaviour and confirm that configuration 4 is indeed the most successful.

Chapter 7

Conclusion

With the Cooper pair splitter device placed in the cryostat at 40 mK, two quantum dots formed between the normal and superconducting electrodes. The dots were first characterised, using the observed Coulomb peaks in both dots to extract the charging energy, energy level spacing and the gate factor of the dots. The values found for U_c and ΔE satisfied the requirements stated in section 3.6. Next, the observed Coulomb peaks in both dots were investigated further by looking at the superconducting gap. The bias spectroscopy suggested that the coupling regimes of the dots were different, which was confirmed by Γ analysis. The analysis showed that the right dot was less strongly coupled and, from the shape of the ABS states in the bias spectroscopy plots, was likely in the $\Gamma_N > \Gamma_S$ regime. The left dot was assigned to the $\Gamma_S > \Gamma_N$, which was confirmed later. Next, the non-local conductance was measured in both dots for one resonance crossing at positive and negative bias voltage. The observed non-local conductance consisted of a positive and negative peak. This type of signal has been observed before by Schindele et al. in 2014 [42] suggesting the sign change occurs due to ground state transitions in the superconductor. Also observed, and in line with Schindele et al. (2014) is a sign change of the peaks when the source-drain bias is reversed. In order to confirm whether the observed signals were caused by S-state related transport such as Cooper pair splitting, the signal was measured with increasing magnetic field. The non-local conductance disappeared at a magnetic field of 80 mT showing this is indeed the case. With the non-local conductance observed and tested against the field, a total of 32 resonance crossings were investigated at both $V_{SD} = -40$ µV and $V_{SD} = 40$ µV. Most crossings displayed non-local signals with the positive-negative peak seen earlier except the $L4$ resonance in the left dot and the $R2$ resonance in the right dot which showed only positive signals. The reason for this is unknown. The ΔG peaks were strongly dependent on the the local resonance and only weakly dependent on the non-local resonance. The visibilities were measured of all the detected signals. This showed the positive peaks being far more successful than the negative peaks. The weak dependence on the non-local resonances is also apparent from the visibility plots.

Next the non-local conductance was tuned. Gate $2, 6, 11$ and 14 on the device were assigned as tuning gates. The tuning of Γ_{LN} using gate 2 was showcased. At each tuning step a trace of the conductance and a bias spectroscopy plot was taken in both the normal an superconducting state. As the voltage on gate 2 was made more negative, the total conductance through the dot decreased drastically, as well as the ABS states becoming more defined. Analysing the Coulomb peaks in the normal state showed that Γ_{LN} was successfully tuned, although Γ_{LS} was slightly affected by it as well. The right dot was unaffected by the tuning of gate 2, showing that independent control of the dots is possible on this device. Finally the device was put in

four different configurations using the tuning of the coupling strengths with the tuning gates. In the first configuration where both dots were in the $\Gamma_S \gg \Gamma_N$ regime, non-local conductance was detected. The device was then moved to an asymmetric regime where the right dot was moved to the $\Gamma_N \gg \Gamma_S$ regime. This regime is the optimal regime for Cooper pair splitting. The asymmetric regime only showed very weak ΔG signals in the right dot. Both dots were put in the optimal regime next, but surprisingly no non-local conductance was visible. The configuration was tweaked in the final regime resulting in a return of the non-local conductance. The experiment was cut short due to a forced warm-up. The calculated visibility and efficiency mirror the observations, with the first and last configurations being the most successful. The visibilities were significantly higher in the final configuration while the efficiency showed an increase of around 2% with respect to the first configuration.

The experiment could have been improved by more tweaking of the configuration of the device. Unfortunately a forced warm-up prevented this. I firmly believe that the efficiency could have been improved further, especially considering the difference between the third configuration which showed no ΔG signals at all and the successful fourth configuration. Being able to explore further would have led to a better understanding of the requirements to create a very efficient Cooper pair splitter. Secondly, the initially observed non-local conductance could have been fitted to the rate equation model used to fit the similar looking signals in [42]. This would have provided more insight into the nature of the observed signal and is something I would definitely recommend to be done in future. Thirdly, repeat measurements of the 2D ΔG plots would have decreased the noise and would have provided more precise values for the visibility and efficiency. Unfortunately time constraints prevented repeat measurements being utilised for the plots in this thesis. After the warm-up we did experiment with repeat measurements. However, while improving the signal to noise ratio, creating one 2D plot of ten repeat measurements took about 16 hours. Attempting to analyse the large number of resonance crossings and device configurations would require careful planning and time management.

The next step is to analyse the extra data collected in this experiment. Three additional resonance crossings were measured in the four configurations. Comparing their efficiency and visibility across the configurations to the $L5 - R1$ crossing shown in this thesis would solidify the claim of successful tuning to high efficiency regimes.
The experiment can be repeated with different Cooper pair splitter devices, investigating the success of different materials and configurations to attempt to reach a near unity efficiency. As explained in section 3.6, even with a 100% efficient device the entanglement of the Cooper pair electrons can decay in or before reaching the normal leads. Spin detection measurements are a necessary next step to ensure the success of the Cooper pair splitter as an entangled electron source. Finding the right parameters to ensure entanglement, along with a configurable, highly efficient Cooper pair splitter will end the search for a reliable and reproducible source of entangled particles and will greatly aid the research into the development of qubits.

This thesis showcased non-local conductance observed in both dots which was measured simultaneously. An unprecedented number of resonance crossings have been investigated, giving a very complete view of the non-local signals. This thesis showed the ability to successfully tune a Cooper pair splitter device in order to increase the efficiency of the non-local conductance as suggested by Fülöp et al. [12], which is an important step towards creating a reliable source of entangled particles for use in the generation of qubits.

Chapter 8

Appendix

Appendix A: All data collected on the device

The following tables introduce all the data taken on the device in the full experiment of the thesis. It is split in two tables, with table 8.1 showing all the data obtained before the forced warm-up. The rows highlighted in light blue are the data sets included in the thesis. The data taken before the warm-up mostly consists of tuning the 4 main tuning gates leading up to the configuration measurements.
Table 8.2 shows the data taken after the warm-up. While the dots remained fairly stable and it was easy to return to the previous regimes, noise had become a big problem. As a result, a lot of gate tuning was performed to find good, clear non-local signals to repeat the configuration measurement performed the thesis. Unfortunately, this was unsuccessful, leading to a attempt to average ΔG over a number of measurements (repetitions). While this was successful in some cases, when attempting to measure ΔG the conductance peaks kept shifting, rendering the averaged data useless. New current amplifiers were brought in to reduce the noise but they were only partially effective. After several more tuning attempts, it was concluded that the device was no longer suitable for configuration measurements. After that the temperature dependence of the non-local signal was measured, disappearing at 200 mK aligning with the earlier B-field dependence showing ΔG is due to superconducting effects. The chemical potentials of the two normal electrodes were also varied and finally the non-local conductance was measured at different ground state transitions, showing the positive-negative peak combination seen so often in this thesis only occurs when the ground state transitions from a singlet to a doublet state or vice versa.
After this experiment was concluded, the device was used to investigate double dot systems as the many gates on the device can be used to precisely manipulate the two dots, in an experiment led by Kasper Grove-Rasmussen.

Data type	Data description
ΔG plots	$L1-4@R1-4$ at ± 40 µV
Bias dependence	$L3@R4$ and $L3@R2$ from -200 to 200 µV
Tuning g2	From 0 to -0.55 V
Tuning g2 ΔG plots	Large scale ΔG and total conductance plots containing several peaks at $g2 = 0, -0.3$
Bias dependence $L4@R2$	From -100 to 100 µV Gate switch occurred on left dot resulting in losing the peaks. Peaks named with letters, e.g LA, until the previous peaks were found
Bias dependence	LA, D, E From -60 to 60 at $g2 = -0.3$ µV
Tuning g2 #2	From 0 to -0.5
Tuning g2 #2 ΔG plots	$LC-D@R1-2$ at 40 µV only
Tuning g2 #3	From 0 to -0.5 no ΔG plots
Bias dependence	$LC, LD@R1$ from -90 to 90 µV
Tuning g6	From 0 to -0.7 at $g2 = -0.3$
Tuning g6 ΔG plots	Large scale ΔG and total conductance plots containing several peaks $@-0.3, -0.5$, Traditional 2D ΔG plots containing one peak $@-0.5, -0.7$
Tuning g14	From 0.3 to -0.6
Tuning g14 ΔG plots	$L5-6@R1-2$ at $g14 = 0, -0.3, -0.6$
Tuning g11	From 0.6 to 0.55. stability test
Tuning g14	From -0.6 to 0.45. no ΔG plots
Regime tuning	Tuning dots to the 4 regimes used in the configurations
Configurations	Measured ΔG in 4 configurations

Table 8.1: *Data overview BEFORE warm-up. Highlighted rows are the data sets that were included in the thesis. Each row represents a data set. The description states the key parameters or results in the data set. The notation L@R refers to a resonance crossing. When referring to a gate, e.g. gate 2, the notation g2 is used.*

Data type	Data description
Tuning g6	From -0.4 to -0.7
Tuning g6 ΔG plots	Regimes in dots similar to before the warm-up when clear signals were detected. However observe weak to no signal and high noise
Tuning g2	From -0.3 to -0.6
Tuning g2 ΔG plots	$L3-4@R3-4$
Tuning g13	From -0.3 to -0.6
Tuning g13 ΔG plots	$L4@R3-4$
Bias dependence	$L4@R3$ from -240 to 240 µV (above Δ). Signal persists above Δ but disappears with $B > B_c$
Tuning g11	From 0.6 to 0.85
Tuning g11 ΔG plots	$L3-4@R3-4$
Tuning g11	From -0.85 to -1.0 no ΔG plots
Tuning g2	From -0.4 to -0.3
Tuning g6	From -0.4 to -0.7
Tuning g6 ΔG plots	$L3-4@R1-2$
Tuning g2	From -0.3 to -0.4
Tuning g2 ΔG plots	$L1-4@R1-2$
New current amplifiers installation	Switched to Basel IF3602 and LSK389A in order to try to reduce the noise
Tuning g2	From -0.4 to -0.3
Configurations	$L3@R2$ tuned across 4 different dot configurations. ΔG signal was averaged over 7 repetitions on only the left dot. Frequent peak shifting prevented further measurements
Tuning g2	From -0.4 to -0.3
Tuning g6	From -0.6 to -1.0
Tuning g2	From -0.3 to -0.5
Tuning g11	From 0.6 to 0.8
Tuning g11 ΔG plots	$L0-2@R1-2$
Tuning g6	From 0 to 0.8
Tuning g6 ΔG plots	$L1-2@R1-2$
T-dependence	$L1@R2$ and $L2@R1$. ΔG disappears at 200 mK
Tuning g11	From 0.6 to 0.85
Tuning g11 ΔG plots	$L3/4@R0$ at g11 = 0.8, 0.85
Tuning g2	from -0.5 to -0.4
Tuning g2 ΔG plots	$L3-4@R1-2$ at g2 $= -0.4, -0.5$
μ_L and μ_R dependence	Varied source and μ_L and μ_R from -80 to 80 µV while measuring ΔG.
Ground state dependence	Measured signal for two singlet states on left dot and two doublet state on right dot. Found single positive peak for singlet-singlet crossing and positive-negative peak combo for singlet-doublet crossing
Ground state dependence	Measured signal for two singlet states on both dots. Found single positive or single negative peak for singlet-singlet crossings

Table 8.2: *Data overview AFTER warm-up. Each row represents a data set. The description states the key parameters or results in the data set. The notation L@R refers to a resonance crossing. When referring to a gate, e.g. gate 2, the notation g2 is used.*

Appendix B: Additional data taken on the different configurations

As stated in the thesis, the non-local conductance of 4 peak crossings, $L5-6@R1-2$, was measured across the 4 different configurations. The thesis only showcased one, $L5@R1$. The visibilities of the three remaining peak crossings were measured and averaged with the visibilities obtained from the $L5@R1$ crossing. The results are shown in Fig. 8.1. However, only the first 3 configurations are averaged. During the fourth configuration the left dot experienced a peak shift, as seen in Fig. 8.2, resulting in nearly all the ΔG peaks being out of frame or not trustworthy. As a result, only the data extracted from $L5@R1$ is usable in the fourth configuration.

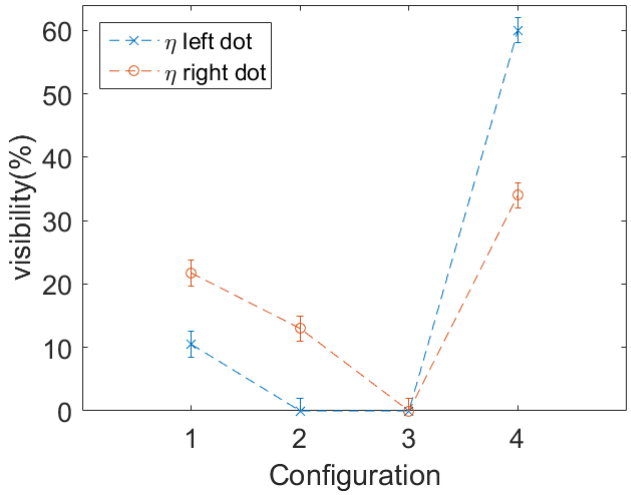

Figure 8.1: *The visibilities of the non-local signal across the four configurations. Configuration 1, 2 and 3 are averaged. 4 is not and only shows the visibility of the $L5@R1$ peak crossing. This is due to a peak switch which made the non-local signal in the other peak crossings disappear.*

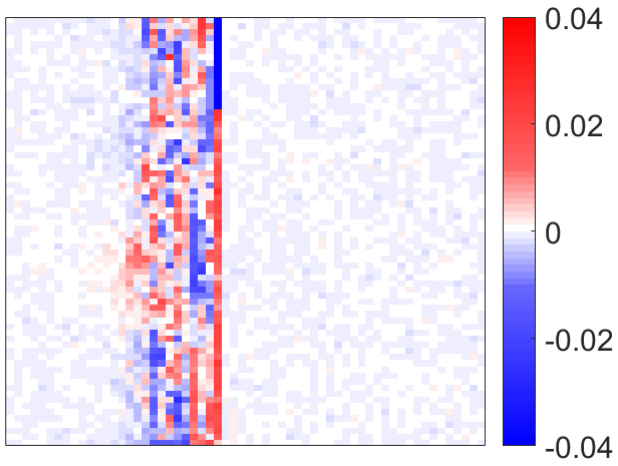

Figure 8.2: *The non-local conductance measured in the fourth configuration showing the peak switch. The signal is collected from left to right in vertical traces. The instantaneous drop in conductance shows that the peak has moved. In the consecutive measurements the peak was out of frame.*

The visibilities in configuration 1 and 3 are quite consistent. Configuration 1 has values around 10% for the left dot and 24% for the right dot. Configuration 3 is zero all round, just as the left dot in the second configuration. The value of 13% for the right dot is the average of two values of zero from the $L5-6@R2$ peak crossings and two values of 26% from the $L5-6@R1$ crossings. Configuration 4 has no clear signals due to the peak switch aside from the ones seen in the thesis and is therefore not averaged.

Appendix C: Tuning of gate 6

Included is the data taken while tuning gate 6 from 0 V to -0.7 V before the warm-up. Gate 6 is the tuning gate for Γ_{LS} coupling. This particular tuning set was interesting for two reasons. Firstly there is a very clear transition of the Andreev bound states, going from smooth to very sharp states. Secondly the non-local conductance ΔG is visible in some of the raw conduction data. This shows the non-local signal seen in the thesis is not an artefact of the computer algorithms but actually real. The tuning of the ABS states is shown first, then several large scale ΔG plots are shown, taken during the tuning, showcasing several peaks.

As Fig. 8.3 shows the Andreev bound states move from a smooth profile in Fig. 8.3b to a very sharp profile in Fig. 8.3f and h. A smooth profile occurs when Γ_S is large. From the tuning of gate 2, shown in the thesis, we know that the dot is in the $\Gamma_S > \Gamma_N$ regime. This is reflected in the shape of the ABS. When the negative voltage on gate 6 is increased, the potential barrier becomes larger and the coupling strength decreases. The shape of the ABS states suggests that the dot has moved to $\Gamma_N > \Gamma_S$ regime.

The large scale ΔG plots are generated with a different color scale than used in the thesis. This color scale enhanced the contribution of the non-local signal most clearly. The non-local contribution is most obvious in Fig. 8.6b and Fig. 8.8b. This contribution correlates with strong positive peaks seen in (d). Both these signals occur at negative bias. At positive bias ΔG becomes much weaker. The left dot shows some non-local contrbutions in the large overview plots in Fig. 8.4a and Fig. 8.5a.

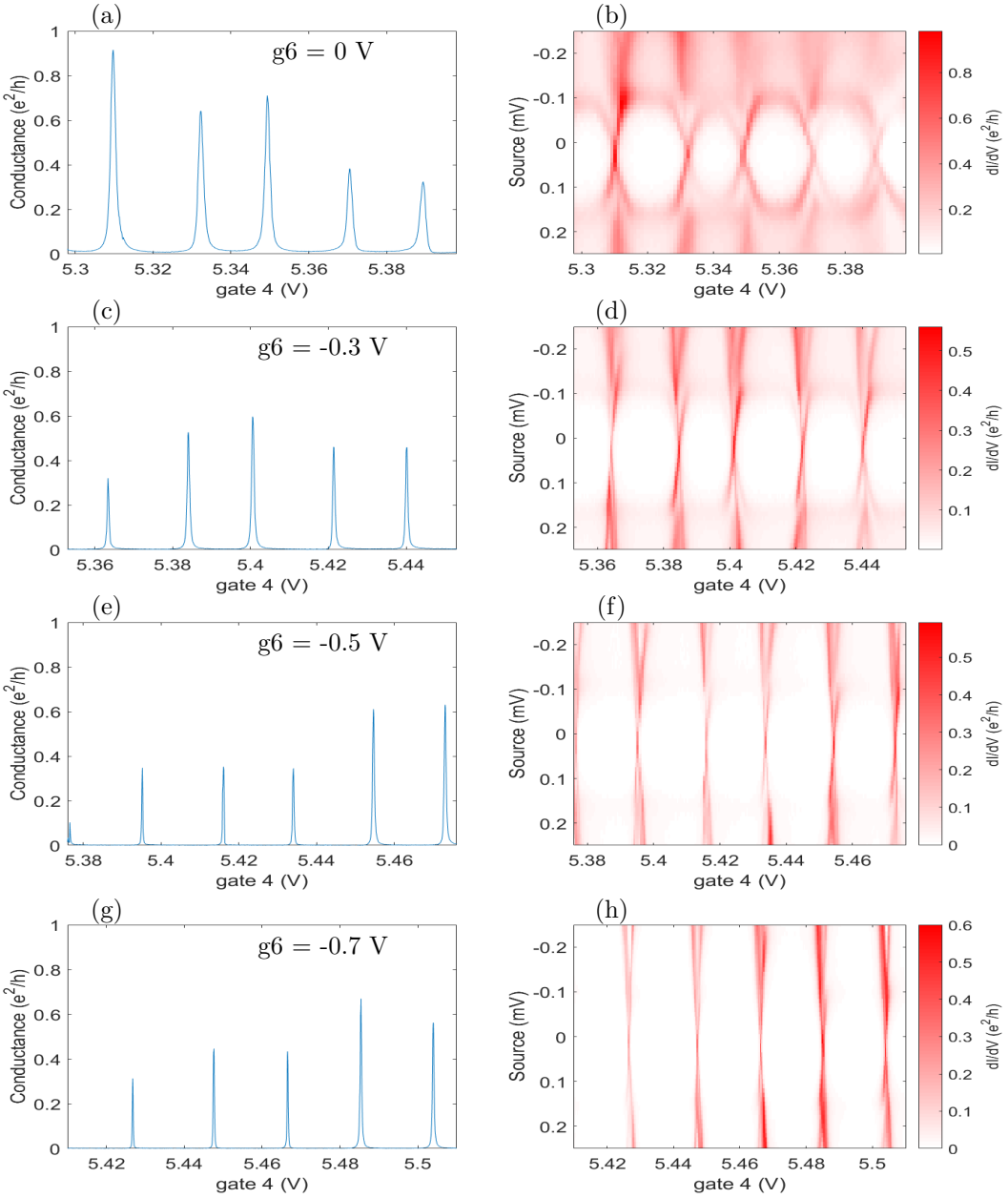

Figure 8.3: *The conductance (a),(c),(e),(g) and the corresponding bias spectroscopy (b),(d),(f),(h) of the left dot in the superconducting state as a result of the tuning of gate 6 (g6) from* 0 *V to* −0.7 *V. The value of gate 6 is stated on the conductance plots but also applies to the bias spectroscopy plots to the right. The Andreev bound states move from a smooth profile (b) to a very sharp profile (h) indicating a likely regime change in the dot.*

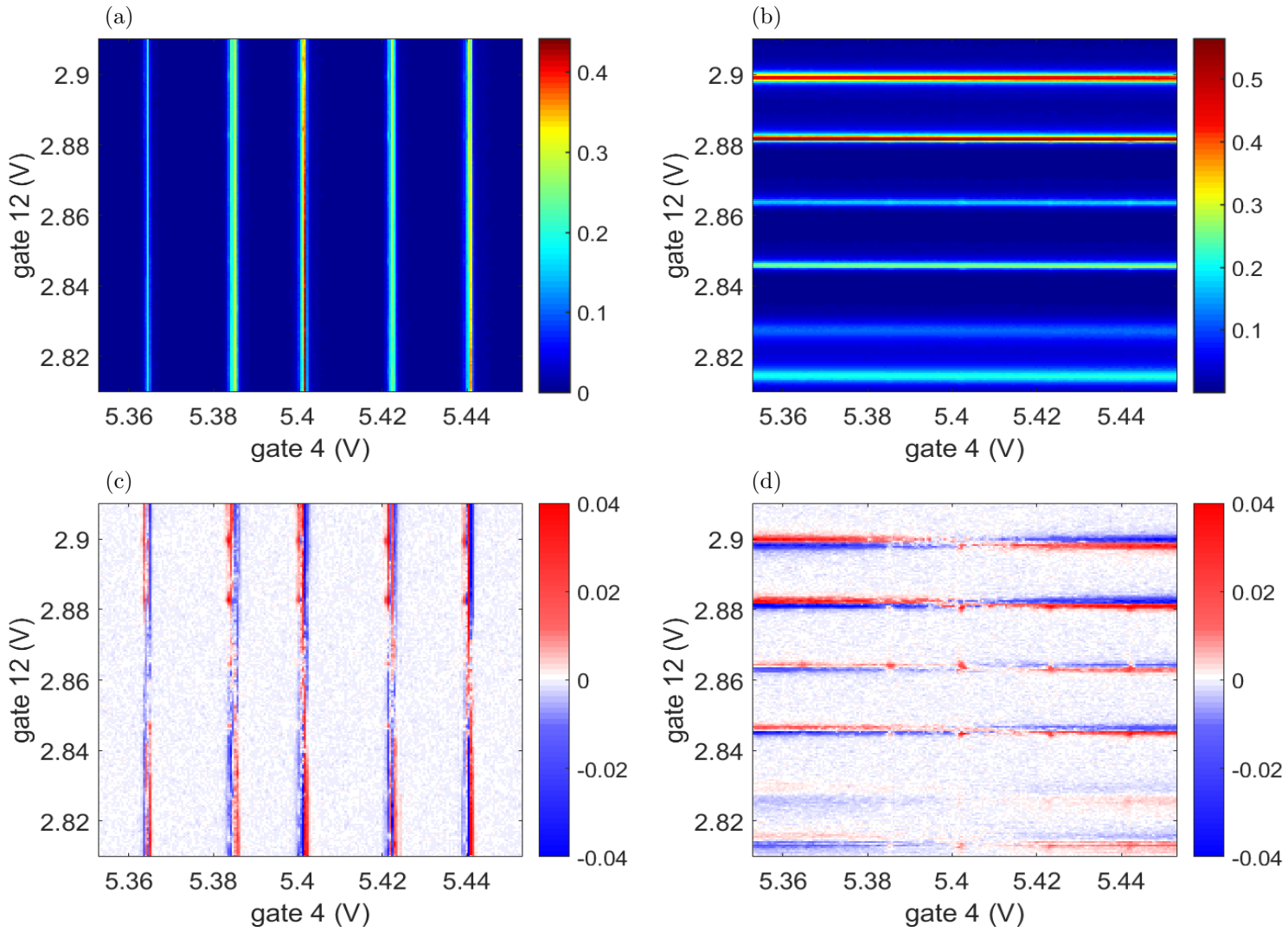

Figure 8.4: *The total conductance (a)-(b) and non-local conductance (c)-(d) through the left dot at* $g6 = -0.3$ *V at a bias of* -40 μV.

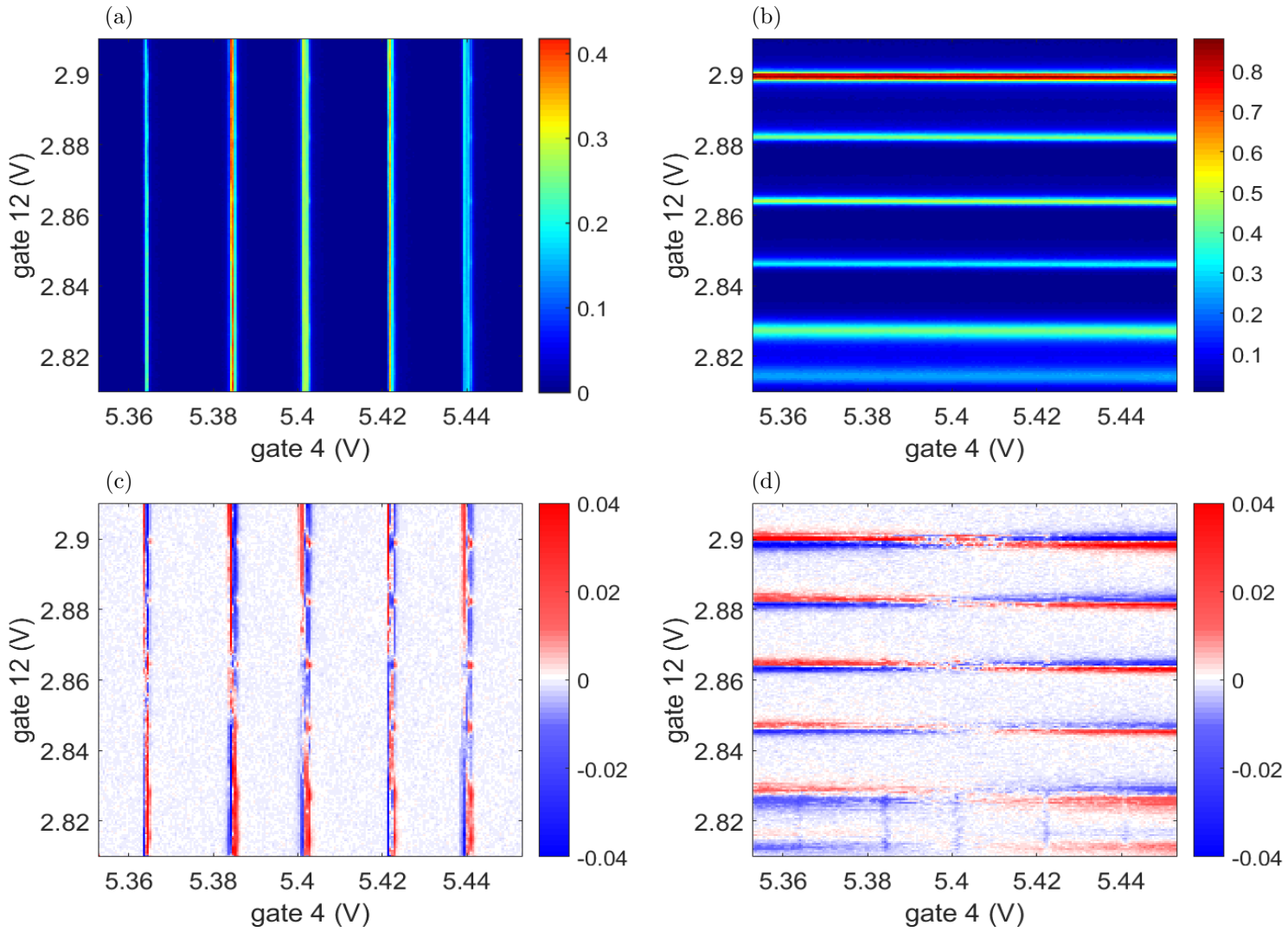

Figure 8.5: *The total conductance (a)-(b) and non-local conductance (c)-(d) through the left dot at* $g6 = -0.3$ *V at a bias of* 40 μV.

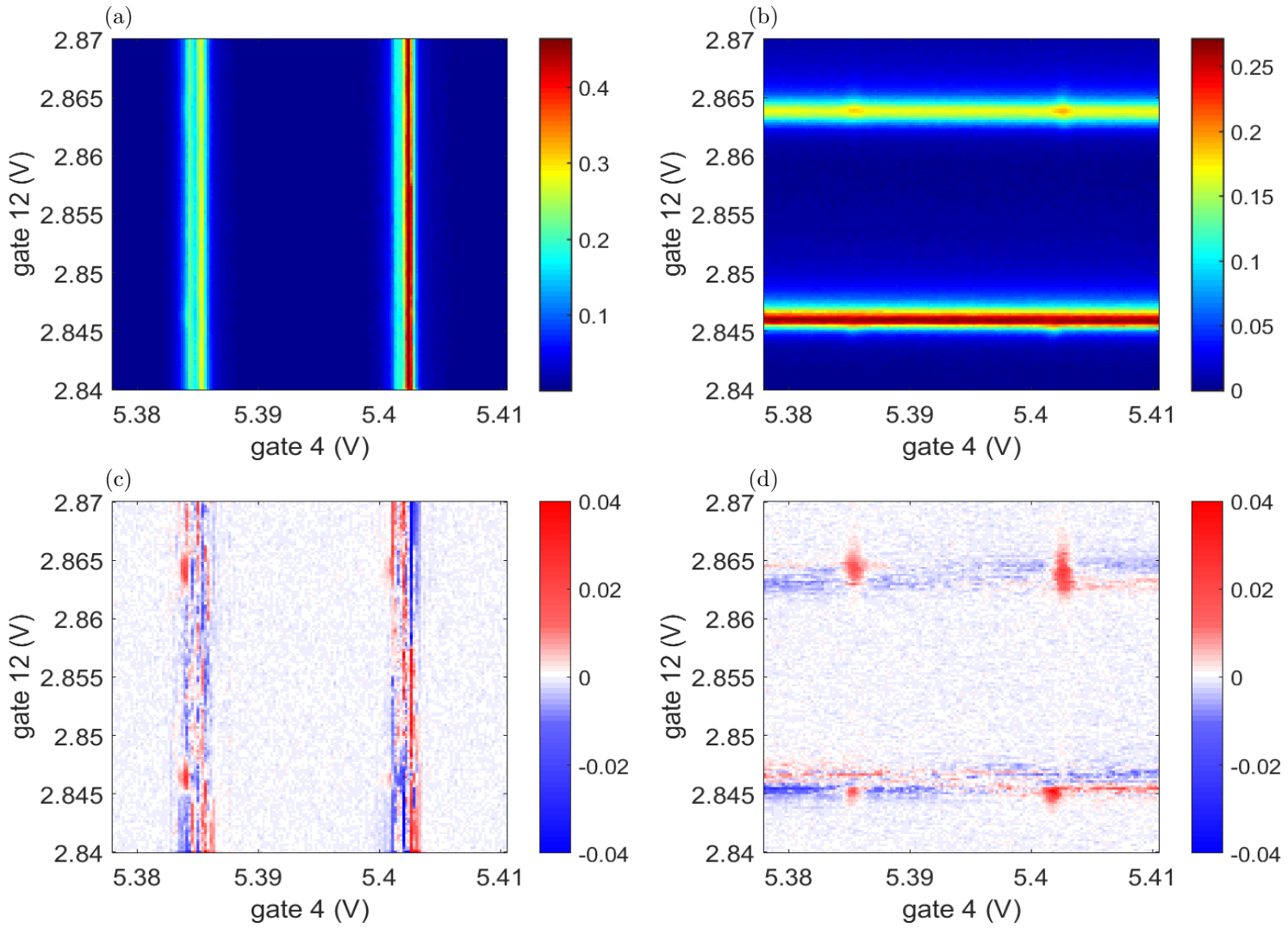

Figure 8.6: *The total conductance (a)-(b) and non-local conductance (c)-(d) through the left dot at* $g6 = -0.3$ *V at a bias of* -40 μV.

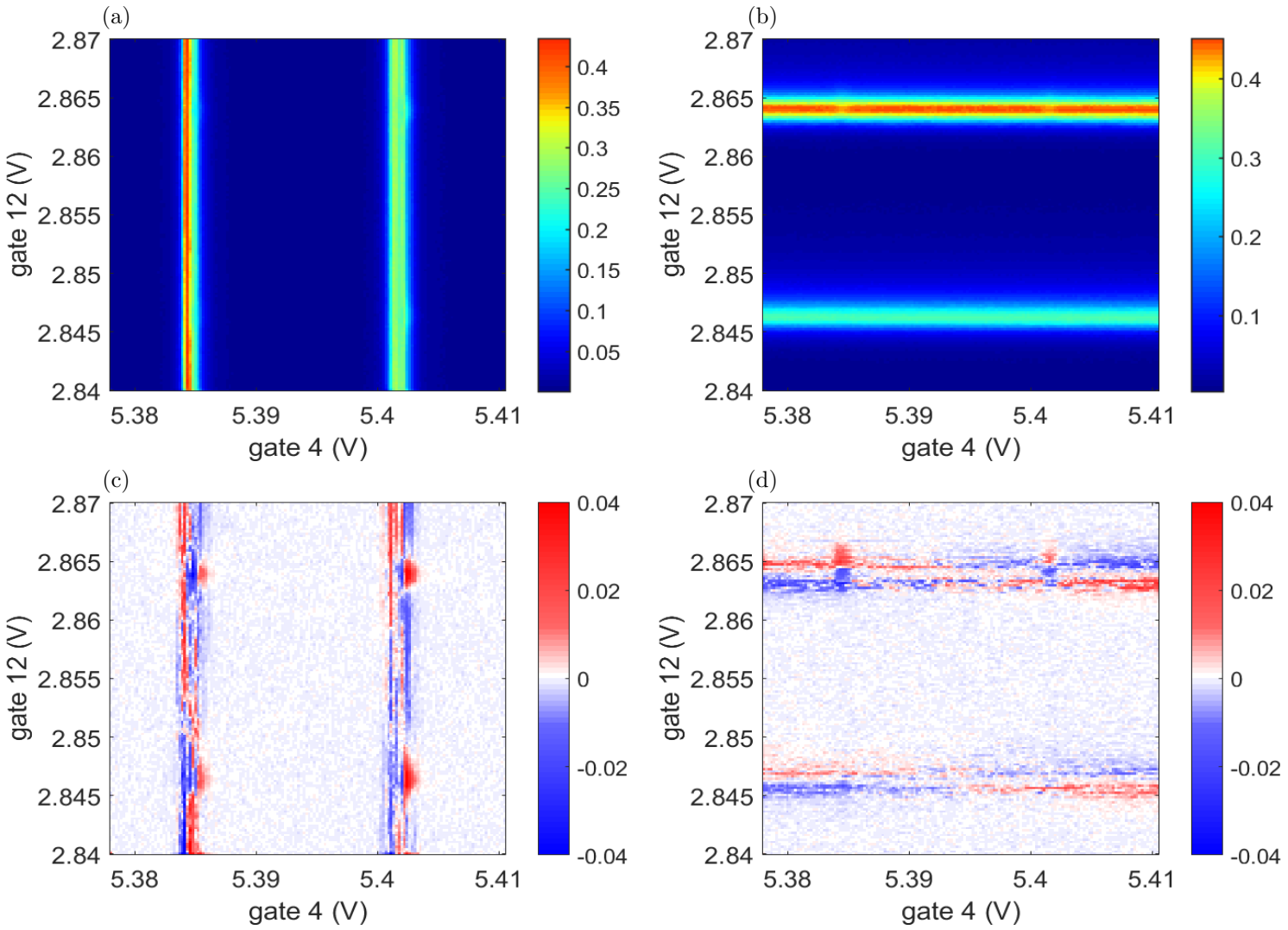

Figure 8.7: *The total conductance (a)-(b) and non-local conductance (c)-(d) through the left dot at* $g6 = -0.3$ *V at a bias of* 40 μV.

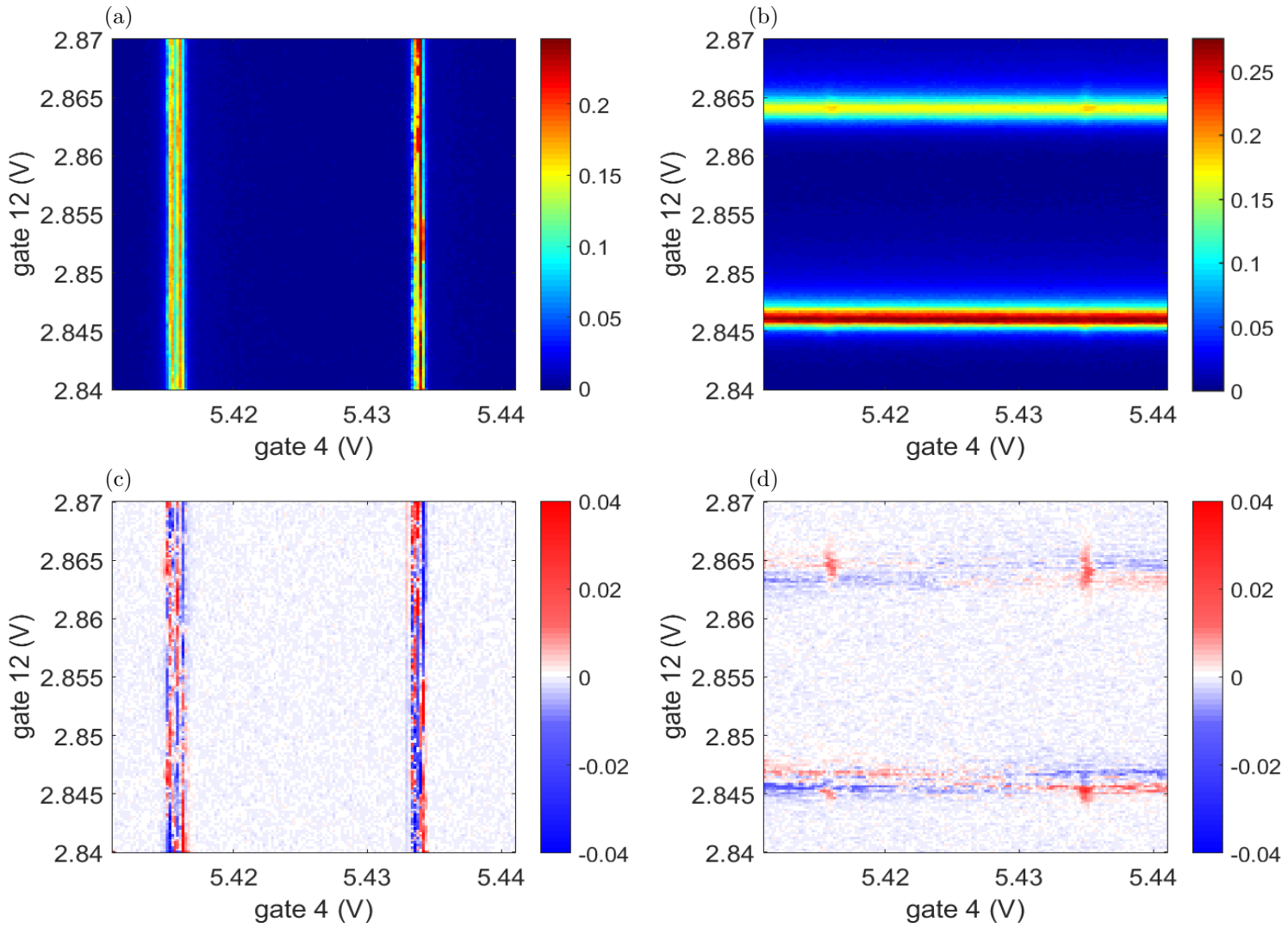

Figure 8.8: *The total conductance (a)-(b) and non-local conductance (c)-(d) through the left dot at* $g6 = -0.5$ *V at a bias of* -40 μV.

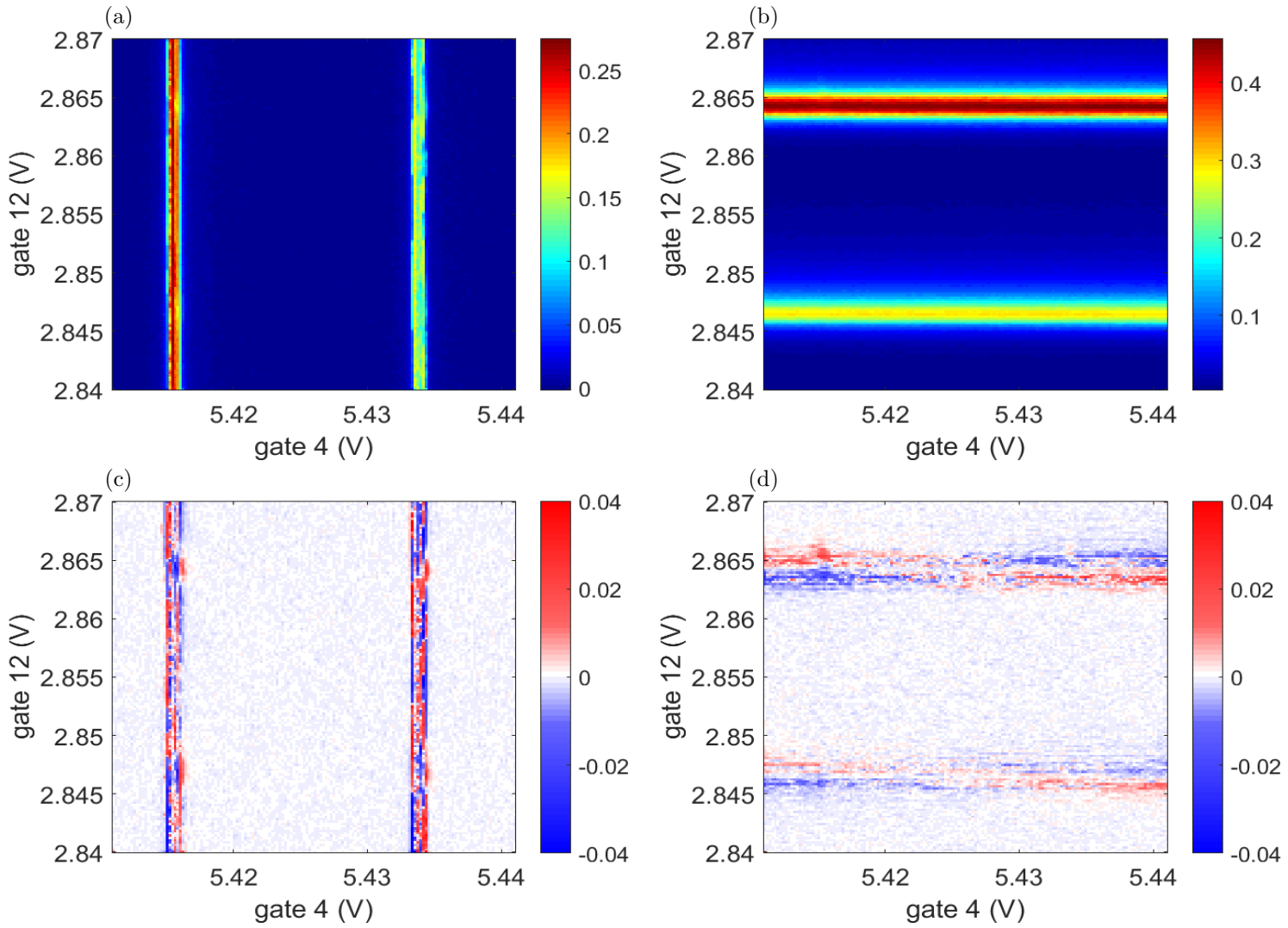

Figure 8.9: *The total conductance (a)-(b) and non-local conductance (c)-(d) through the left dot at* $g6 = -0.5$ *V at a bias of* 40 μV.

Bibliography

[1] A. Einstein, B. Podolsky, and N. Rosen, "Can Quantum-Mechanical Description of Physical Reality Be Considered Complete?," *Physical Review*, vol. 47, pp. 777–780, May 1935.

[2] M. A. Nielsen, Chuang, and L. Isaac, *Quantum Computation and Quantum Information*. Cambridge University Press, 2010.

[3] P. W. Shor, "Polynomial-Time Algorithms for Prime Factorization and Discrete Logarithms on a Quantum Computer," *eprint arXiv:quant-ph/9508027*, Aug. 1995.

[4] D. P. Divincenzo, "Quantum Computation," *Science*, vol. 270, pp. 255–261, Oct. 1995.

[5] K. Saeedi, S. Simmons, J. Z. Salvail, P. Dluhy, H. Riemann, N. V. Abrosimov, P. Becker, H.-J. Pohl, J. J. L. Morton, and M. L. W. Thewalt, "Room-Temperature Quantum Bit Storage Exceeding 39 Minutes Using Ionized Donors in Silicon-28," *Science*, vol. 342, pp. 830–833, Nov. 2013.

[6] P. G. Kwiat, K. Mattle, H. Weinfurter, A. Zeilinger, A. V. Sergienko, and Y. Shih, "New high-intensity source of polarization-entangled photon pairs," *Physical Review Letters*, vol. 75, pp. 4337–4341, Dec. 1995.

[7] R. P. Feynman, "Simulating Physics with Computers," *International Journal of Theoretical Physics*, vol. 21, pp. 467–488, June 1982.

[8] L. N. Cooper, "Bound Electron Pairs in a Degenerate Fermi Gas," *Physical Review*, vol. 104, pp. 1189–1190, Nov. 1956.

[9] L. Hofstetter, S. Csonka, J. Nygård, and C. Schönenberger, "Cooper pair splitter realized in a two-quantum-dot Y-junction," *nature*, vol. 461, pp. 960–963, Oct. 2009.

[10] L. G. Herrmann, F. Portier, P. Roche, A. L. Yeyati, T. Kontos, and C. Strunk, "Carbon nanotubes as cooper-pair beam splitters," *Phys. Rev. Lett.*, vol. 104, p. 026801, Jan 2010.

[11] J. Schindele, A. Baumgartner, and C. Schönenberger, "Near-Unity Cooper Pair Splitting Efficiency," *Physical Review Letters*, vol. 109, p. 157002, Oct. 2012.

[12] G. Fülöp, S. d'Hollosy, A. Baumgartner, P. Makk, V. A. Guzenko, M. H. Madsen, J. Nygård, C. Schönenberger, and S. Csonka, "Local electrical tuning of the nonlocal signals in a Cooper pair splitter," *Physical Review B: Solid State*, vol. 90, p. 235412, Dec. 2014.

[13] N. N. Bogoliubov, *Theory of superconductivity*, vol. 4. CRC Press, 1968.

[14] A. M. Kadin, "Spatial Structure of the Cooper Pair," *eprint arXiv:cond-mat/0510279*, Oct. 2005.

[15] M. Tinkham, *Introduction to superconductivity*. McGraw-Hill, 1996.

[16] J. Bardeen, L. N. Cooper, and J. R. Schrieffer, "Theory of Superconductivity," *Physical Review*, vol. 108, pp. 1175–1204, Dec. 1957.

[17] K. Yamazaki, T. Yamaguchi, and H. Namatsu, "Three-Dimensional Nanofabrication with 10-nm Resolution," *Japanese Journal of Applied Physics*, vol. 43, p. 1111, Aug. 2004.

[18] U. Cvelbar, "Towards large-scale plasma-assisted synthesis of nanowires," *Journal of Physics D Applied Physics*, vol. 44, p. 174014, May 2011.

[19] J. Elias, J. Michler, L. Philippe, M.-Y. Lin, C. Couteau, G. Lerondel, and C. Lévy-Clément, "ZnO Nanowires, Nanotubes, and Complex Hierarchical Structures Obtained by Electrochemical Deposition," *Journal of Electronic Materials*, vol. 40, pp. 728–732, May 2011.

[20] Y. Wang, L. Zhang, C. Liang, G. Wang, and X. Peng, "Catalytic growth and photoluminescence properties of semiconductor single-crystal ZnS nanowires," *Chemical Physics Letters*, vol. 357, pp. 314–318, May 2002.

[21] C. Thelander, P. Agarwal, S. Brongersma, J. Eymery, L. Feiner, A. Forchel, M. Scheffler, W. Riess, B. Ohlsson, U. Gsele, and L. Samuelson, "Nanowire-based one-dimensional electronics," *Materials Today*, vol. 9, no. 10, pp. 28 – 35, 2006.

[22] J. Schindele, *Observation of Cooper Pair Splitting and Andreev Bound States in Carbon Nanotubes*. PhD thesis, Philosophy and Natural Sciences Faculty, University of Basel, 2014.

[23] R. C. Ashoori, "Electrons in artificial atoms," *nature*, vol. 379, pp. 413–419, Feb. 1996.

[24] S. de Franceschi, L. Kouwenhoven, C. Schönenberger, and W. Wernsdorfer, "Hybrid superconductor-quantum dot devices," *Nature Nanotechnology*, vol. 5, pp. 703–711, Oct. 2010.

[25] L. P. Kouwenhoven, D. G. Austing, and S. Tarucha, "Few-electron quantum dots," *Reports on Progress in Physics*, vol. 64, no. 6, p. 701, 2001.

[26] C. W. J. Beenakker, "Theory of coulomb-blockade oscillations in the conductance of a quantum dot," *Phys. Rev. B*, vol. 44, pp. 1646–1656, Jul 1991.

[27] H. I. Jørgensen, T. Novotný, K. Grove-Rasmussen, K. Flensberg, and P. E. Lindelof, "Critical Current 0-π Transition in Designed Josephson Quantum Dot Junctions," *Nano Letters*, vol. 7, pp. 2441–2445, Aug. 2007. Supplementary information.

[28] S. Sapmaz, P. Jarillo-Herrero, J. Kong, C. Dekker, L. P. Kouwenhoven, and H. S. J. van der Zant, "Electronic excitation spectrum of metallic carbon nanotubes," *Phys. Rev. B*, vol. 71, p. 153402, Apr 2005.

[29] S. De Franceschi, S. Sasaki, J. M. Elzerman, W. G. van der Wiel, S. Tarucha, and L. P. Kouwenhoven, "Electron cotunneling in a semiconductor quantum dot," *Phys. Rev. Lett.*, vol. 86, pp. 878–881, Jan 2001.

[30] A. Martn-Rodero and A. L. Yeyati, "Josephson and andreev transport through quantum dots," *Advances in Physics*, vol. 60, no. 6, pp. 899–958, 2011.

[31] L. Yu *Acta Physica Sinica*, vol. 21, 1965.

[32] H. Shiba, "Classical Spins in Superconductors," *Progress of Theoretical Physics*, vol. 40, pp. 435–451, Sept. 1968.

[33] A. I. Rusinov, "On the Theory of Gapless Superconductivity in Alloys Containing Paramagnetic Impurities," *Soviet Journal of Experimental and Theoretical Physics*, vol. 29, p. 1101, 1969.

[34] A. Jellinggaard, K. Grove-Rasmussen, M. H. Madsen, and J. Nygård, "Tuning yu-shiba-rosinov states in a quantum dot." To be published, 2016.

[35] O. Sauret, D. Feinberg, and T. Martin, "Quantum master equations for the superconductor˘quantum dot entangler," *Phys. Rev. B*, vol. 70, p. 245313, Dec 2004.

[36] P. Recher, E. V. Sukhorukov, and D. Loss, "Andreev tunneling, Coulomb blockade, and resonant transport of nonlocal spin-entangled electrons," *Phys. Rev. B*, vol. 63, p. 165314, Apr. 2001.

[37] C. Kittel, *Introduction to Solid State Physics*. Wiley, 8 ed., 2004.

[38] P. Y. Yu and M. Cardona, *Fundementals of semiconductors*. Springer, 1995.

[39] R. Levy, *Microelectronic materials and processes*. Kluwer Academic publishers, 1 ed., December 2012. Softcover reprint.

[40] M. J. Madou, *Fundementals of Microfabrication: The Science of Miniaturization*. CRC Press, 2 ed., March 2002.

[41] A. Jellinggaard, *Dots coupled to a superconductor*. PhD thesis, The Faculty Of Science, University of Copenhagen, 2015.

[42] J. Schindele, A. Baumgartner, R. Maurand, M. Weiss, and C. Schönenberger, "Nonlocal spectroscopy of Andreev bound states," *Physical Review B*, vol. 89, p. 045422, Jan. 2014.